NTNU

Norwegian University of
Science and Technology

Feasibility Studies on Integrating Offshore Wind Power with Oil Platforms

Atle Rygg Årdal

Master of Science in Energy and Environment
Submission date: June 2011
Supervisor: Tore Marvin Undeland, ELKRAFT
Co-supervisor: Raymundo Torres-Olguin, ELKRAFT

Norwegian University of Science and Technology
Department of Electric Power Engineering

Problem Description

Offshore oil and gas platforms are traditionally equipped with gas turbines and synchronous generators in order to generate their required electric power. The efficiency of these gas turbines is very low compared with onshore power plants. To interconnect platforms with renewable energy sources can therefore contribute significantly to reduce the overall CO_2-emissions from Norway. At the same time, a large number of offshore wind farms are planned along the Norwegian coast. These projects have a marginal economy, where the grid connection is considered as one of the largest expenses. To connect offshore wind farms together with oil and gas installations is beneficial in this respect. Research should be performed in order to identify the potential.

The thesis should identify the major challenges that must be addressed in a power system consisting of an offshore wind farm and an oil platform. The technology status and current projects should be explored, followed by development of one or more relevant case studies. Modeling and control of the Voltage Source Converter should be one of the main topics in the thesis. Converters should be incorporated into the respective power systems with suitable control strategies. Relevant transient scenarios should be explored in simulation models built in PSCAD/EMTDC^{TM}. The results will lay foundation for discussions and conclusions regarding the behavior and feasibility of the systems.

Assignment given: Trondheim 17.01.2011
Supervisor: Tore Marvin Undeland, Department of Electrical Engineering

Preface

This report is the result of my final semester as a master student with the Department of Electrical Engineering, NTNU. The final year has brought a great amount of knowledge, along with valuable experiences and hard work.

It is not easy to decide the topic and contents of the master thesis as an uncertain 4^{th} year student. I feel very privileged to be surrounded with so many enthusiastic and helpful persons that have pushed me in the right directions during the past year. I would like to thank those that have contributed to the work.

My mentor and co-supervisor from day one has been Dr. Eng. Kamran Sharifabadi in Statoil. He initiated the cooperation that eventually led to the specialization project and master thesis, and has been a great resource throughout the whole period. His fast replies and ability to find all kinds of simulation data and references have truly been of great service.

Secondly, I express my sincere gratitude to PhD-student Raymundo Torres Olguin. He has been my co-supervisor with the department, and his efforts have been extremely valuable. He has gladly provided guidance in every way, and I owe him a huge debt for the numerous hours he has spent on my thesis.

I also express thankfulness to Dr. Ing. Salvatore D'Arco for his thorough assistance and feedback regarding the paper I have submitted to EPE Wind Energy Chapter. Gratitude is also rewarded PhD-student Bing Liu, for letting me use his PSCAD-model of the aerodynamics in wind turbines, and for answering questions related to his model.

In addition, I thank my family for their love and support during my studies here at NTNU. I am very thankful to my brother who offered to help out with his brilliant English skills during the final correction process. I would also like to express love to my girlfriend, who have helped me through the master year. We have had some long days on campus, and they are much easier to overcome together.

Last but certainly not least, I sincerely thank Prof. Tore Undeland, my supervisor. He has given me this great opportunity to explore the field of power electronics, and it has been an honor to be his master student. His combination of outstanding experience together with the commitment toward his students is impressive.

Trondheim 07.06.2011
Atle Rygg Årdal

Summary

This thesis is centered around the possibilities of integrating offshore wind power together with oil and gas platforms. The motivation behind this topic is to reduce the emissions of CO_2 and other pollutive gases from conventional offshore power plants. The electrical systems on oil platforms are weaker than an onshore grid, so measures should be taken to let the wind power integration contribute to a more stable operation on the platform. To explore existing and future technologies that can achieve this is an important part of this work.

Two different power systems are presented, denoted System 1 and System 2. Their schematics are shown in Fig. 1. Corresponding simulation models are built from fundamental blocks in the software PSCAD/EMTDC^{TM}. Aggregated models are utilized in order to save computational time.

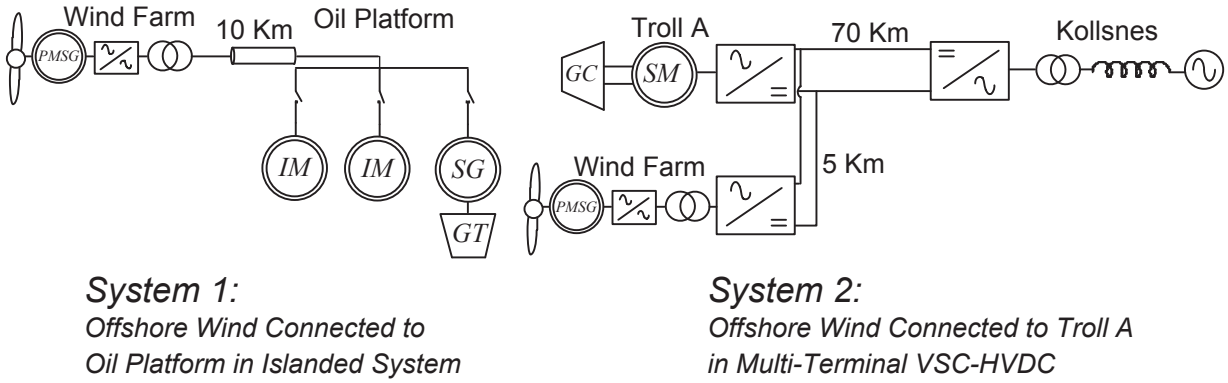

Fig. 1: Schematics of System 1 and System 2

System 1 consists of an offshore wind farm and an oil platform connected together in islanded operation. The oil platform contains an synchronous generator with an associated gas turbine and can adjust both active and reactive power quickly. The load consists of fixed-speed induction motors. The wind farm contains a back-to-back Voltage Source Converter (VSC) which is used for variable speed operation of the turbine. The converter is also used for voltage support to the system, and this functionality reduces voltage oscillations during disturbances. The most critical scenario investigated is to start a large induction motor. It is shown that the transmission cable may contribute to an increasing risk of voltage collapse during the start-up. Another critical event is when the wind power is suddenly disconnected, and the gas turbine has to adjust the power output quickly in order to avoid too large frequency deviations. The simulations show that a disconnection of the whole wind farm does not lead to critical operation or possible instability. This would not be the case in a system with slower control systems in the gas turbine and synchronous generator.

System 2 consists of a VSC-HVDC connection between Kollsnes and the platform Troll A. This existing configuration is powering a gas compressor on the platform through a variable speed synchronous motor. This thesis proposes to integrate wind power on the DC-side of the Troll A VSC-terminal. The challenge is to inject wind power in a way such that the operation of the gas compressor is not disturbed. The proposed control system is working as intended, and the selected simulation cases show that the compressor system is not affected by the wind power. The DC voltage control system is able to maintain a constant voltage at the Troll terminal during normal operation. The wind farm reduces the losses in the HVDC-cable, and surplus wind power is sent to the land grid during low-load operation. The DC-voltage drops to 73 % of the rated value for 10 ms when the wind power is suddenly disconnected, but the duration is so short that it does not affect the gas compressor operation.

The simulation results indicate that both configurations are feasible. However, the results are heavily dependent on the parameter data, and further research should put more efforts into gaining as correct values as possible. A sensitivity analysis is performed to System 1 as a guideline to which parameters that are most decisive, and therefore should be modeled most accurately. In addition, new simulation cases might reveal challenges that this thesis does not concern.

Contents

List of Figures

Abbreviations

AVR Automatic Voltage Regulator (Oil Platform System 1)

DC Direct Current

GC Gas Compressor(Troll A)

GSC Generator Side Converter

GT Gas Turbine (Oil Platform System 1)

HVDC High Voltage Direct Current

IM Induction Motor (Oil Platform System 1)

MSC Motor Side Converter (Troll A)

OSC Onshore Side Converter (Kollsnes)

PMSG Permanent Magnet Synchronous Generator (Used in wind turbines)

pu. Per Unit (Divided by a given reference value)

SM Synchronous Motor (Troll A)

SSC System Side Converter (Wind Turbine System 1)

VSC Voltage Source Converter

WSC Wind Side Converter (System 2)

Chapter 1

Introduction

1.1 Problem Background and Motivation

The climate crisis is a topic that concerns the population worldwide. Research has predicted that the consequences will be severe if the necessary measures are not taken within a short period of time. Large efforts are put toward reduction of greenhouse gas emissions from the energy sector. It is, however, a hard task to achieve without decreasing the standard of living, while at the same time letting less developed countries progress against western standards. Politicians and research communities are looking for solutions toward a less pollutive energy production. This includes renewable energy sources, as well as modifications of existing fossil fuel technologies. In 2007, the European Union committed their member countries to reduce their emissions with 20 % within 2020 [1].

Norway is blessed with a vast amount of oil and gas on its continental shelf. These resources have provided the country with wealth since the first drilling started around 1970. But the resources are limited, and the oil production was at its peak around year 2000 [2]. 56 % of the oil resources and 24 % of the gas resources are extracted in the beginning of 2010 [3]. [4] gives an overview of different attempts on estimating when the world peak oil production occurs, and it is assumed to happen before 2015.

Oil installations in the North Sea utilize gas fired turbines in order to generate their required electric energy. The turbines are placed on the platform and operate with a low efficiency due to area constraints and operation requirements. The efficiency lies in the range of 30 % for a typical offshore gas turbine[5]. The turbines are often operated at part-load, causing further reductions in efficiency [6]. The CO_2-emissions originating from the oil and gas installations are significant with respect to Norway's total emissions, and was 29 % in 2005 [7]. In addition to the environmental aspects, the utilization of gas comes at a great monetary expense for the involved companies. Norway has employed tax on NO_x- and CO_2-pollution, and this is the main economical incentive behind offshore electrification. Moreover, large revenues are lost as the gas could be sold to the market. Norwegian authorities have made incentives to replace offshore gas turbines with electricity from shore as one contribution to fulfill the EU 2020-requirements [8].

In addition to extensive fossil resources, the Norwegian coast is blessed with wind resources. A great amount of offshore wind power is being planned along the whole coast, and a total capacity of 4.5 GW is reported to the Norwegian authorities as planned projects [9]. No farms have been built yet due to the currently large costs associated with offshore wind power. If an offshore wind expansion will take place in Norway, it is important to evaluate all different ways of grid connection. See [10] for different ways to integrate offshore wind farms into the land grid.

It would be beneficial to consider a synergy between offshore wind and oil platforms, since it is a costly process to electrify offshore installations. A key motivation behind this is the overall reductions in CO_2-emissions. Research might reveal that a synergy can decrease

the investment cost compared to a case where the grid integration was done separately. The platform owners are very interested in reducing the size of their conventional power plants. This will be increasingly important in the future, as the installed power per produced petroleum unit is expected to grow in the coming years.

This thesis will focus on electrification of oil platforms by means of offshore wind power. No such configurations exist today, but some research has been performed. A preliminary feasibility study by Sintef and Statoil [11] investigates the amount of CO_2-reductions, and also evaluates the voltage and frequency variations during large disturbances. A few operational scenarios of a wind farm interconnected with an oil platform are simulated in [12], where the main focus is transient stability. Moreover, detailed models and simulation results are described for an islanded power system including a gas/diesel generator connected with wind turbines in [13] -[17].

1.2 Relation to Specialization Project

The author wrote a specialization project report in the fall of 2010 [18]. It was titled "Modeling and Simulation of an Offshore Wind Farm Connected to an Oil Platform as an Islanded System". Some material from this report has been used in this thesis in order to form a more complete and independent text. This includes the following sections:

- Chapter 2 Voltage Source Converters (Except section 2.3 and section 2.7)
- Section 3.1: Aerodynamics of Wind Turbines
- Section 3.2: Pitch Control
- Section 3.3: Generator Technologies for Offshore Wind
- Section 3.9: Oil Platform Synchronous Generator
- Section 3.8: Oil Platform Gas Turbine
- Section 3.10: Oil Platform Induction Motors (Except section 3.10.2)

In addition, some paragraphs in other sections originate from the specialization project, but the content generally rewritten and restructured.

1.3 Outline of the Thesis

The following section explains the sequence of the contents and how the chapters are connected to each other.

Chapter 2 explains the basic features of the Voltage Source Converter (VSC). The VSC plays an important role in the thesis, and a large part of the work has been dedicated to design control systems that utilize the possibilities that the fast control of VSC introduces. The reader can omit reading chapter 2 with prior knowledge on the VSC, but should in any case pay attention to section 2.7. This section develops the basic control strategy that is shared among all the converters that are part of the different models.

The thesis is centered around two offshore power systems, denoted System 1 and System 2. The modeling and simulation chapters belonging to the two systems are separated in order to avoid confusion between them. A short description of the two systems will be presented below.

System 1

In System 1, a 20 MW wind farm is connected to an oil platform with maximum load of 40 MW. The platform has a 50 MW generating unit. The system will have no connection to the onshore grid.

Chapter 3 describes the modeling process of System 1. The wind farm model contains aerodynamic properties and a pitch control system, see section 3.1 and section 3.2. The available generator technologies are discussed in section 3.3, and the choice of generator in the simulations fell on the Permanent Magnet Synchronous Generator (PMSG). Modeling and control of the PMSG are covered in section 3.4 and section 3.5, respectively. The wind turbine is equipped with a back-to-back VSC, and the interaction between the PMSG and converter is an important part of the model. The last part of the wind turbine model is the control system in the System Side Converter (SSC), and it is covered in section 3.6. The model and equations belonging to the submarine cable between the wind farm and oil platform are given in section 3.7. The oil platform model consists of three major parts. First is the gas turbine in section 3.8, which is responsible for generating power on the platform. Second is the synchronous generator in section 3.9, which transfers the mechanical energy from the gas turbine into electrical energy. Third is the platform load, which as a simplification, is assumed to exclusively consists of fixed speed induction motors. Details regarding induction motor modeling and behavior are found in section 3.10.

A simulation model of System 1 is built in PSCAD/EMTDC^{TM}. All blocks are created by the author, except for the aerodynamic wind turbine model. See appendix H for documentation of the simulation model. Tuning and testing of the individual control systems are put in appendix C. Chapter 5 contains all simulations performed on System 1, supplemented with discussions and references to the model sections.

System 2

System 2 is a case study on an existing gas platform. Troll A lies in the North Sea and is operated by Statoil. Two parallel 45 MW VSC-HVDC systems are connected between the onshore processing plant in Kollsnes and two separate synchronous motors on the platform [6]. The motors are powering two gas compressors, and the offshore VSCs employ variable speed operation in order to control the gas flow through the pipelines. This thesis investigates the potential of integrating offshore wind power with the VSC-HVDC systems.

Chapter 4 treats the model and control systems of System 2. The chapter starts with a description of Troll A in section 4.1, and a discussion on how wind power can be integrated in section 4.2. The chapter continues with a description of the models and control of the synchronous motor in section 4.3 and section 4.4, respectively. The DC-network model is found in section 4.5, while the control system of the onshore converter at Kollsnes is covered in section 4.6. This thesis proposes that a 20 MW wind farm is connected to the DC-side of the offshore VSC. An additional VSC is installed in the wind farm, and the control system required here is described in 4.7. The wind farm model from System 1 is used for the simulations.

A simulation model of System 2 also built in PSCAD/EMTDC^{TM}. Appendix D describes the tuning process of the control systems. Transfer functions and Bode Diagrams are important tools in this respect. The control systems are tested individually in the beginning of chapter 6. This chapter includes all simulations performed to System 2, and each result is supplemented with a corresponding discussion.

1.4 Publication of Results

A paper based on the work in this report has been submitted to the EPE Wind Energy Chapter conference that took place in Trondheim May 9-11 2011. It is related to System 1, and performs a sensitivity analysis on the parameters in the system. The paper has the following co-authors: Raymundo Torres Olguin (NTNU), Salvatore D'Arco (NTNU), Kamran Sharifabadi (Statoil) and Tore Undeland (NTNU). See appendix J.

Another paper was submitted to the Norwegian Electrotechnical Association technical meeting in March 2010. It was written in cooperation with Kristin Høvik, and has Tore Undeland (NTNU) and Kamran Sharifabadi (Statoil) as co-authors. Its contents are related to electrification of offshore installations in general, where the role of VSC is highlighted. See appendix K.

Chapter 2

Voltage Source Converters

Power electronic converters are a fundamental component in electrical energy conversion. They have several applications within the field of renewable energy because they can improve the efficiencies and power quality.

2.1 VSC, Principles of Operation

The Fig. 2.1 shows the diagram of a two-level VSC. v_a,v_b and v_c represent the phase voltages, while the points P and N are the positive and negative potential of the DC-link respectively. The line current in phase A must pass through either T_{pa}, T_{na} or their respective diodes. The voltage $v_{aN} = v_a - v_N$ will be either v_{dc} or 0, depending on which switch or diode is conducting. It will therefore be a square-wave, but as the switching frequency can be much higher than the fundamental frequency, good approximations to sinusoids can be achieved. Note that the neutral point of the AC-side is floating with respect to N.

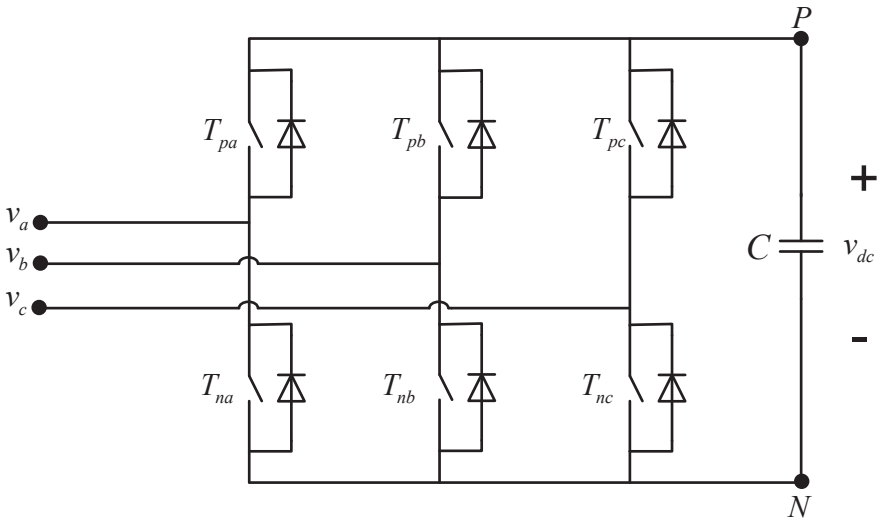

Fig. 2.1: Voltage Source Converter

There are several ways to modulate the transistors. Space-Vector-Modulation is one strategy where the vectorial sum of the AC-voltages is controlled [19]. Another technique is the carrier-based modulation [20]. Here, each of the phase voltages are controlled independently. This thesis will use a carrier-based modulation technique.

2.2 Pulse-Width-Modulation

This thesis uses Pulse-Width-Modulation (PWM) for the triggering of transistors. The technology is used in the VSC-HVDC solution presented by ABB under the brand HVDC Light ^{TM} [21]. In carrier based PWM, the transistors are turned on and off based on a comparison between two signals. One is a fixed triangular pulse v_{tri} with a high frequency, in range of several kHz. The other signal, $v_{control}$, is dynamically generated by the control circuit according to the specified objectives [20]. The transistor T_{pa} in Fig. 2.1 will conduct only when $v_{control,a} > v_{tri}$, and T_{na} conducts when $v_{control,a} < v_{tri}$. $v_{control,a}$ is the control signal corresponding to phase a. Fig. 2.2 shows the two signals that are compared in basic sinusoidal PWM, along with the resulting v_{aN}.

Fig. 2.2 shows only one phase, but the principle is equal in a three-phase system. In three-phase, three different control voltages are compared against the triangular pulse, and during a crossing, the two transistors that corresponds to the respective phase, change states.

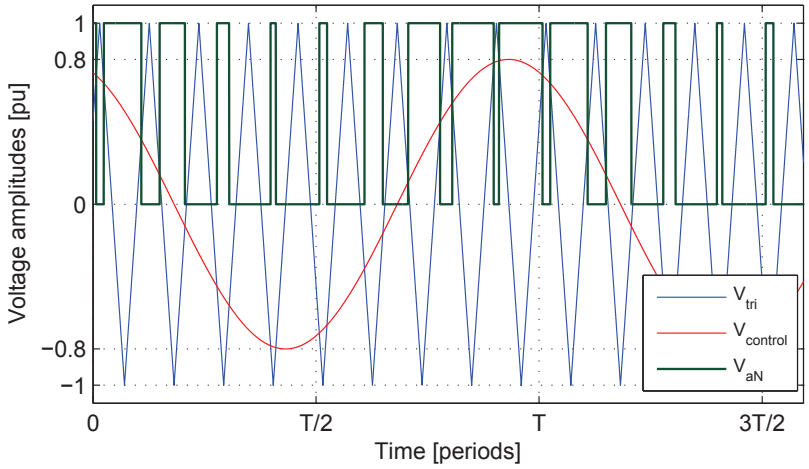

Fig. 2.2: Pulse Width Modulation waveforms

2.3 Multilevel VSC

Another VSC configuration is presented by Siemens under the brand HVDC Plus^{TM} [22]. A section on this technology is included in order to show different ways of implementing VSCs. Figure 2.3 shows the waveform that is generated by the multilevel VSC. The idea behind this technology is to build up the voltage in small steps, in contrast to the two-level VSC in Fig. 2.2 where the voltage v_{aN} is either 0 or v_{DC}. In order to achieve this, a number of IGBT modules are coupled in series and connected to individual capacitors which hold a share of the DC-link voltage. This is shown in Fig. 2.3. Depending of which IBGTs that are conducting, 9 different steps of AC line-to-line voltage is obtainable. For a given switching frequency, the harmonic distortion will be significantly smaller compared with two-level VSC [23]. The switching frequency can therefore be reduced, which will lead to smaller losses in the converter. The HVDC Plus^{TM} concept entered the market some years after HVDC Light^{TM}, so ABB is for the time being holding the major market share.

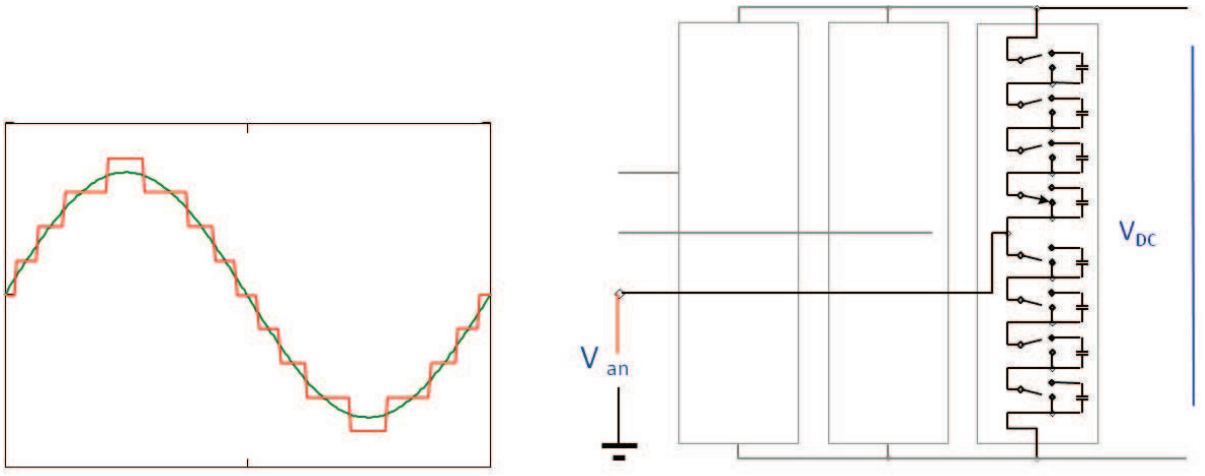

Fig. 2.3: Multilevel VSC

2.4 Harmonics in converter output

From this point, only two-level VSC is considered. The line-to-line voltage $v_{ab} = v_a - v_b$ should contain a minimum of harmonics. In the line-to-line voltage, all harmonics that are a multiple of 3 are cancelled out when the system is balanced [20].

A simulation with constant references is carried out for illustration purposes. The frequency of the triangular carrier is set to $9 \cdot f_n$ where f_n is the fundamental frequency. The number 9 is referred to as the modulation ratio m_f in [20]. v_{ab} is shown in Fig. 2.4. It can be either v_{dc}, 0 or $-v_{dc}$, and the approximation to a sinusiod is clearly visible. The harmonics in v_{ab} are calculated and shown in Fig. 2.4. The harmonics that are present are located around multiples of m_f. This result is important, as all low-frequent harmonics can be eliminated by using a sufficient high modulation ratio. An increase in m_f will shift the harmonics to higher frequencies, and the amplitudes from Fig. 2.4 remain constant [20]. The high-frequency harmonics are much easier to filter, so the harmonic distortion in the connection point can be lowered.

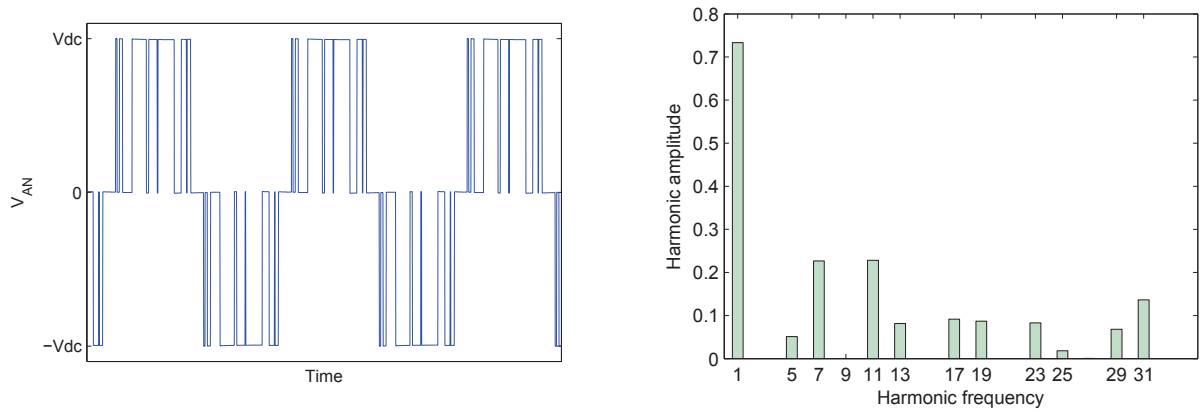

Fig. 2.4: V_{ab} and its harmonic components

2.5 Detailed Model of VSC

The most accurate model of a VSC includes switches with properties such as blanking time, snubber circuits and on-state voltage drop. Converter losses are not a part of this study, so the switches are considered ideal without any time-delay or losses. This is still a very detailed model for system studies. The per-phase equivalent circuit of a converter is shown in Fig. 2.5. An inductance L with resistance R is included between between the converter and the connection point.

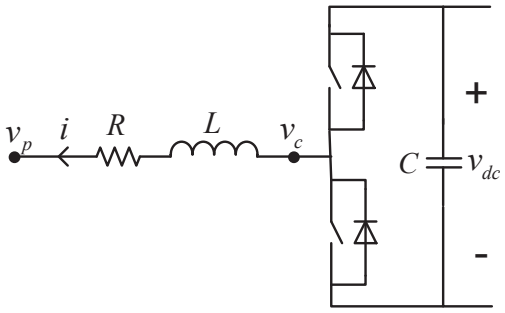

Fig. 2.5: Per phase converter equivalent, detailed model

2.6 Average Model of VSC

As explained in section 2.4, the harmonics are only located around multiples of m_f. If the switching frequency approaches infinity, the converter output will be a pure sinusoid according to section 2.4. The converter can then be modeled as a controlled voltage source. This model will be linear in contrast to the detailed model which has extensive non-linear effects. The computational time is heavily reduced with the average model, and this is the main motivation for its use. A schematic is shown in Fig. 2.6.

The instantaneous power flowing from the AC- to the DC-side must be equal at all times. This can be expressed with the equation:

$$v_{conv,a}(t) \cdot i_a(t) + v_{conv,b}(t) \cdot i_b(t) + v_{conv,c}(t) \cdot i_c(t) = I_{conv}(t) \cdot V_{dc}(t) \tag{2.1}$$

This equation completes the model, as it gives the relation between the AC and DC-side. The average VSC model is used in the simulations.

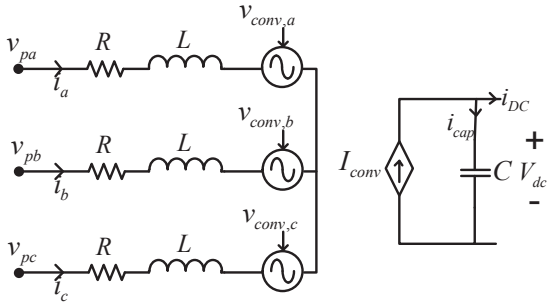

Fig. 2.6: Converter equivalent, average model

2.7 Control of VSC

The control objectives and strategies for the VSC depend on the application. This section explains in general the control strategies and structures of VSC. A generic model will be established that serves as a framework for the control systems in the different applications of VSC. The control of the wind turbine PMSG is found in section 3.5, while its grid side converter control is covered in section 3.6. Control of the synchronous motor in System 2 is described in section 4.4. Details of the onshore converter control in System 2 are found in section 4.6. The offshore wind energy converter in system 2 does not utilize the control principles that are given here. Nevertheless, its control system is stated in section 4.7.

An important feature of the VSC is that it has two degrees of freedom at each terminal. Two variables can be controlled independently. This project uses the well-known vector control technique in order to achieve independent control [24]. The vector control principle is based on a synchronous rotating *dq*-reference frame. The idea behind the *dq*-equivalent is to transform the sinusoidal waveforms into DC-quantities. A key motivation behind this is that the time-varying inductances in a rotating machine are constant in the *dq*-frame [25] [24]. Another benefit is that DC-quantities have smaller variations and are easier to control and simulate than sinusoids. The transformation between *abc* and *dq* is often called Park Transform [24]. Refer to appendix A for the mathematical description. For details regarding how Park Transform can be applied to VSC, refer to [26], [27] and [28].

A cascaded system is used to facilitate the control design. The full block diagram consisting of both the control system and the electrical system is shown in Fig. 2.7. The derivation and ideas are explained below in a general way that is valid for all systems under investigation in this project. The harmonics are assumed negligible, as justified in section 2.4. The author proposes to describe the electrical system by means of the following generic equations in the Laplace-domain:

$$\begin{aligned} V_{cd} &= F_d(s) \cdot i_d + G_d \cdot i_q + H_d \\ V_{cq} &= F_q(s) \cdot i_q + G_q \cdot i_d + H_q \end{aligned} \tag{2.2}$$

$V_{c,dq}$ [1] is the voltage at the converter terminal, i_{dq} is the line current, and $F_{dq}(s)$,G_{dq},H_{dq} are arbitrary functions that is not dependent on i_d and i_q. F_{dq} represents a general impedance, G_{dq} represents the link between the d- and q-axes, while H_{dq} represents a general voltage that is located behind the impedance represented by F_{dq}. An electrical circuit equivalent of the same equations is shown in Fig. 2.8.

The equations are used to create a linearized model of the system. The base control objectives are to let i_d and i_q follow their references i_d^* and i_q^*. The converter can control the voltages V_{cd} and V_{cq} with a time-delay $T_w = \frac{1}{2f_s}$ where f is the switching frequency [26]. This can be expressed in the Laplace domain as:

$$\begin{aligned} V_{cd} &= \frac{1}{1 + T_w s} V_{control,d} \\ V_{cq} &= \frac{1}{1 + T_w s} V_{control,q} \end{aligned} \tag{2.3}$$

[1] Later in the text, the subscript d and q refers to the direct and quadrature axis in the respective transformation frame without further explanation. The notation $V_{c,dq}$ represents the space vector $\vec{V_c} = V_{cd} + jV_{cq}$.

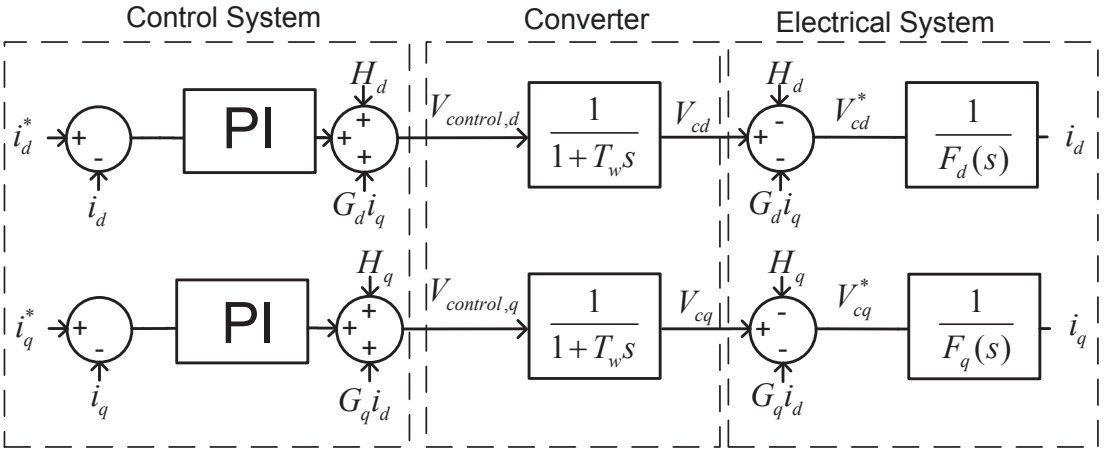

Fig. 2.7: Generic dq-Current Controller

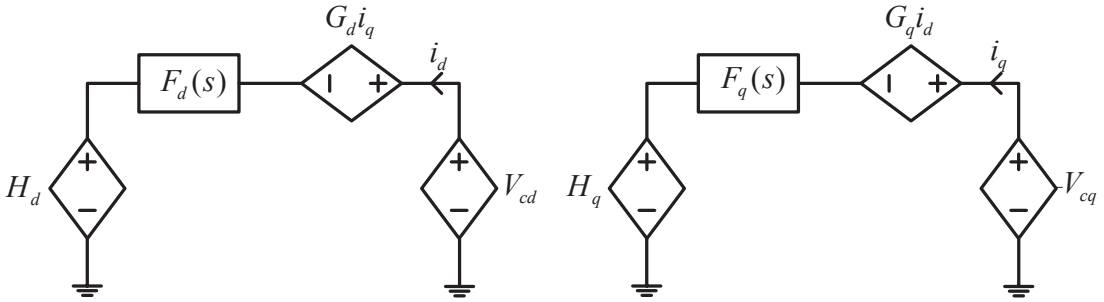

Fig. 2.8: Generalized system in the d-q reference frame

where $V_{control,d}$ and $V_{control,q}$ are the desired voltages, that is, the output of the control system.

The control structure will now be outlined, refer to Fig. 2.7. From (2.2) two variables are defined:

$$\begin{aligned} V_{cd}^* &= V_{cd} - G_d \cdot i_q - H_d = F_d(s) \cdot i_d \\ V_{cq}^* &= V_{cq} - G_q \cdot i_d - H_q = F_q(s) \cdot i_q \end{aligned} \tag{2.4}$$

V_{cd}^* and V_{cq}^* are linear with respect to the currents i_d and i_q, which makes the PI-regulator design easier. $G_{dq} \cdot i_{dq}$ and H_{dq} are added to the regulator output in order to obtain the desired converter voltage $V_{control,dq}$. This voltage will appear at the terminals as $V_{c,dq}$ after a time-delay T_w. The summation to the right in Fig. 2.7 represents the physics in (2.2). Note that if T_w is so small that it can be neglected, the two summation blocks cancel each other out, and F_{dq} remains as the only transfer function between the regulator and feedback.

Chapter 3

System 1: Islanded operation of Wind Farm and Oil Platform

The Fig. 3.1 shows a schematic diagram of System 1, which is a fictitious configuration in the North Sea. It consists of a wind farm connected to an oil platform through an AC sea cable. The advantages with a system like this were discussed in the introduction. The main motivation of modeling the dynamics of System 1 is to obtain a controller that fulfills a set of given requirements. Furthermore, it may show feasibility of paralleling offshore wind farms with oil platforms, and hereby encourage to more research on the topic.

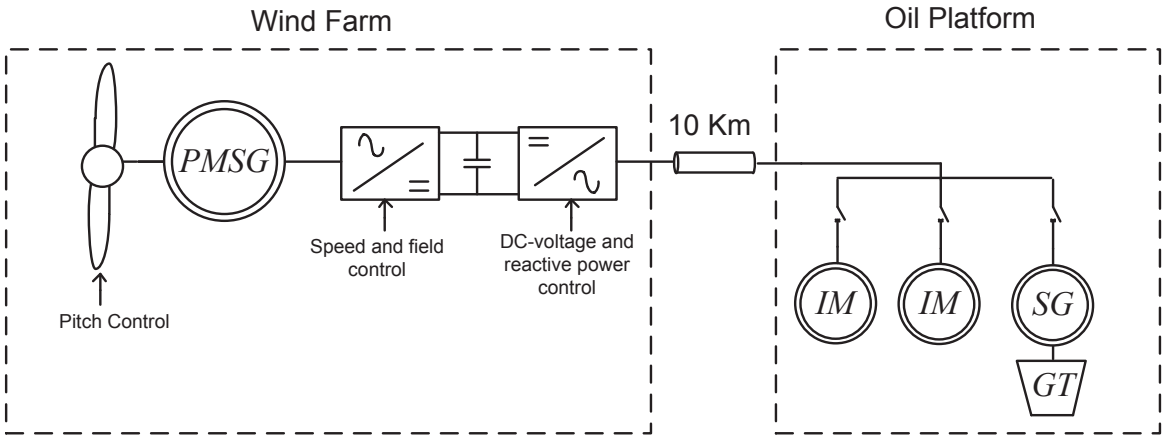

Fig. 3.1: Schematic of System 1: Islanded operation of Wind Farm and Oil Platform

The objective of the wind farm is to extract kinetic energy from the wind and convert it to electrical energy. This consists of several steps. First is the interaction between the wind and the rotor blades. This requires an aerodynamic model of the blades, see section 3.1. Next is the process of converting the mechanical energy to electrical. This is done through the generator, see section 3.4 and 3.5. The generator is connected to a back-to-back VSC, and the control strategies are developed based on the goal of maximum power extraction.

The transmission system between the wind farm and the platform is modeled with ideal transformers and a cable PI-equivalent. The cable has a length of 10 km, and the data are taken from [29]. The cable model is covered in section 3.7, where an important equation describing the reactive power flow is developed.

The oil platform consists of a gas turbine with a synchronous generator and induction motors. The synchronous generator has to provide the load power when the wind speed is low, and it also compensates for the variable power output in the wind. The generator is described in section 3.9 while the gas turbine model is covered in section 3.8. The induction motors are the only load in the system, and a segment on induction machine modeling is found in section 3.10.

3.1 Aerodynamics of Wind Turbines

The rotor blades are designed such that the wind creates a torque in the direction of rotation. The aerodynamic processes are very complex, and their details are out of the scope of this thesis. In this section, a model that is commonly used in electrical system simulations is described.

The fundamental equation for the wind turbine is the relation between mechanical power P_{mech} and wind speed v [30]:

$$P_{mech} = T_{mech} \cdot \omega_m = \frac{1}{2} C_p(\lambda, \beta) \rho A v^3 \tag{3.1}$$

where $A = \pi R^2$ is the rotor area and ρ is the air density. R is the rotor radius, T_{mech} is the mechanical torque acting on the blades and ω_m is the rotational speed of the turbine (rad/s). The factor C_p is the ratio between the energy that is converted and the kinetic energy of the wind, and can be viewed as the instantaneous efficiency of the turbine. C_p can be approximated by means of the following empirical equations [31]:

$$\begin{aligned} C_p &= 0.5 \cdot (\frac{116}{\lambda_i} - 0.4\beta - 5) \cdot e^{-\frac{21}{\lambda_i}} \\ \frac{1}{\lambda_i} &= \frac{1}{\lambda + 0.08\beta} - \frac{0.035}{\beta^3 + 1} \end{aligned} \tag{3.2}$$

Here, $\lambda = \frac{\omega_m R}{v}$ is the tip speed ratio and β is the pitch angle [30]. The values of the numerical constants in (3.2) varies from one blade design to another.

In Fig. 3.2, C_p is plotted versus λ for $\beta = 0$, and the maximum value occurs at $\lambda_{opt} = 6.3$ where $C_p = 0.4382$. This is the motivation behind speed control of the generator, to adjust ω_m such that λ is as close to λ_{opt} as possible.

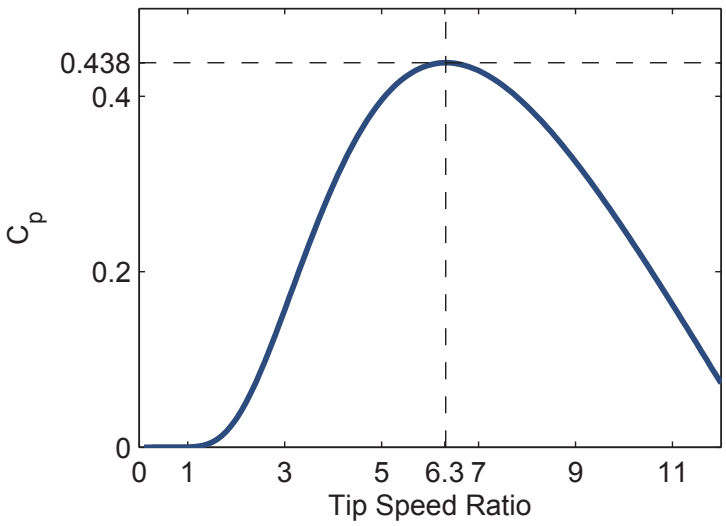

Fig. 3.2: λ versus C_p

The output power for a 2 MW turbine is shown for different wind speeds in Fig. 3.3. In Fig. 3.3a) ω_m is varied from zero to rated, and the power is shown for wind speeds $0 < v < 25$ m/s at each value of ω_m. It is seen that for each value of v, there is a unique ω_m that gives maximum power. Note that the power exceeds 2 MW when $v \approx 12$ m/s, so the pitching mechanism is enabled at this wind speed.

In Fig. 3.3b) the pitch angle β is varied when w_m is held at its rated value. An increase in β will decrease the power, so the pitch angle can be used to limit the power and torque at high wind speeds.

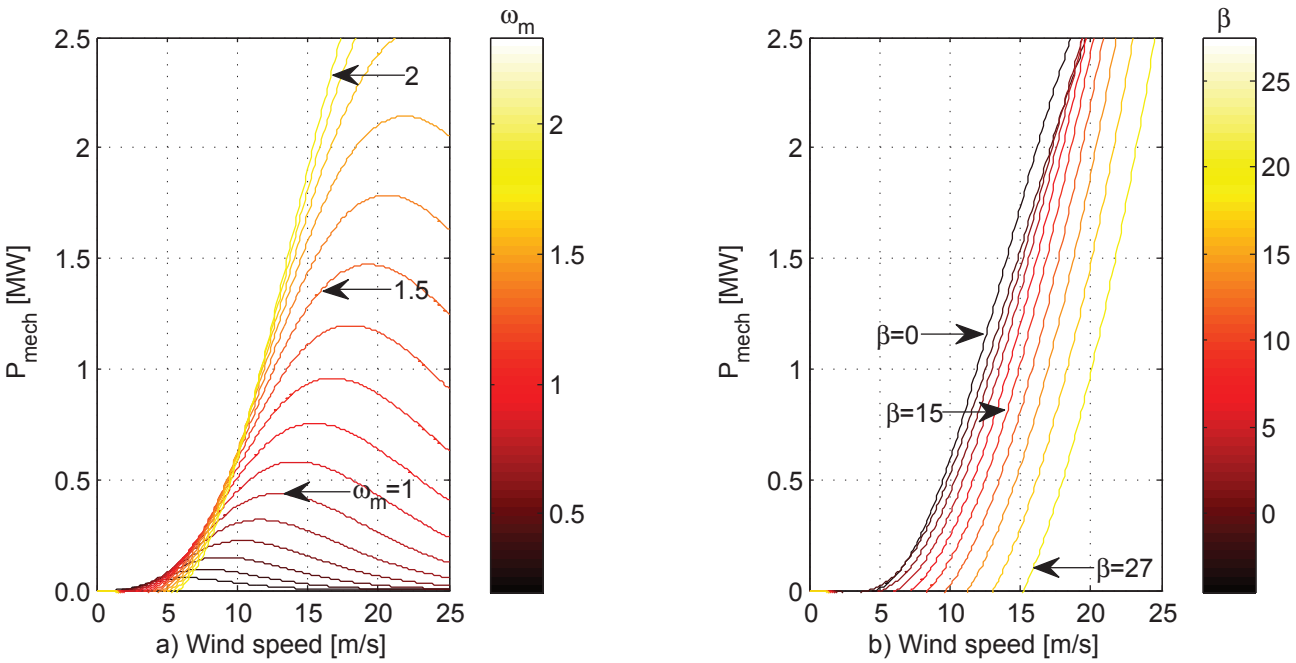

Fig. 3.3: Output power for variable ω_m [rad/s], v [m/s] and β [deg]

The Matlab-code that generates Fig. 3.2 and 3.3 is found in appendix I.

3.2 Pitch Control

When the wind speed is above a certain value, the torque acting on the rotor blades exceeds the rating unless action is taken to alter the aerodynamic properties. This is done through pitching of the blades, which means a rotation with an angle β. The mechanical torque and output power will decrease with increasing β until some point where it reaches zero. There is a limitation on how fast the blades can be turned, but this limit varies from one turbine manufacturer to another.

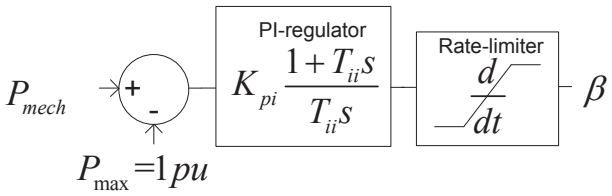

Fig. 3.4: Block diagram of pitch controller

The control structure can be implemented in several ways, see [32] for an overview. In this thesis, a PI-controller is enabled whenever the mechanical power is larger than the rating. This is a simple yet effective structure, and the block diagram is shown in Fig. 3.4. It is assumed that the mechanical power P_{mech} is estimated or measured, and a filter is applied so that the pitch mechanism does not react on small gusts in the wind speed. The mechanical dynamics of the pitching mechanism is not a part of this model, but could be included, see [30].

The aerodynamic processes are highly nonlinear as seen from (3.2). A linear control system such as the PI-controller is therefore not the optimal choice. A pure proportional controller could be used as in [33], but this will lead to steady-state error. Gain scheduling, which means variable control parameters is also an option, see [32].

3.3 Generator Technologies for Offshore Wind Energy

There are different types of generator technologies available for offshore wind turbines. One choice is the induction machine. It has a simple and rugged construction, is relatively cheap, and is easy to disconnect from the grid. It does, however, consume reactive power and requires a stiff grid connection [30].

A modified version of the induction generator called a Doubly Fed Induction Generator is attracting popularity among wind power applications since it addresses the above mentioned problems [34]. It is a wound-rotor machine with the rotor winding connected to the grid through a back-to-back converter. Depending on the rating of the converter, it can provide reactive power support, in addition to variable speed operation over a limited range.

The latest trend is to use a synchronous generator. Its main advantage is related to stability, since it can contribute to voltage control, and it is not dependent on a stiff grid. There are two ways to magnetize the machine, either by field windings or permanent magnets. The Permanent Magnet Synchronous Generator (PMSG) is gaining popularity in offshore wind applications for several reasons. The space required for a certain flux is smaller for a permanent magnet rotor than for a field winding type, so it is possible to have a larger number of poles per circumference. This eliminates the need for a gearbox, which will reduce the maintenance. PMSGs are normally used in combination with a full power electronic converter between the generator and the grid.

The PMSG will be used in the wind farm model in this study, since it is one of the technologies with best prospects in offshore wind development.

3.4 Modeling of PMSG

A mathematical model of the PMSG will now be described. The dynamic equations for the generator can be written [35] [36]:

$$\begin{aligned} v_{cd} &= R_s i_d - \omega_s \psi_{sq} + \frac{d\psi_{sd}}{dt} \\ v_{cq} &= R_s i_q + \omega_s \psi_{sd} + \frac{d\psi_{sq}}{dt} \end{aligned} \tag{3.3}$$

where $v_{c,dq}$ is the stator terminal voltage, R_s is the stator resistance, i_{dq} is the stator currents flowing into the generator and ω is the electrical speed of the machine. For synchronous generator control, the d-axis is aligned with the rotor flux ψ_r, in such a way that $\psi_{rq} = 0$ [24]. $\psi_{s,dq}$ is the flux linkages in the stator, and it can be expressed through the following equations [35]:

$$\begin{aligned} \psi_{sd} &= L_{sd} i_d + \Psi_f \\ \psi_{sq} &= L_{sq} i_q \end{aligned} \tag{3.4}$$

L_{sd} and L_{sq} are the stator inductances, that is, the sum of the leakage inductance and the mutual inductance between rotor and stator. Ψ_f is the constant flux produced by the permanent magnets. (3.3) can be rearranged and written in the Laplace domain in order to match (2.2):

$$\begin{aligned} v_{cd} &= \underbrace{(R_s + sL_{sd})}_{F_d(s)} i_d + \underbrace{-\omega L_{sq}}_{G_d} i_q + \underbrace{0}_{H_d} \\ v_{cq} &= \underbrace{(R_s + sL_{sq})}_{F_q(s)} i_q + \underbrace{\omega L_{sd}}_{G_q} i_d + \underbrace{\omega \Psi_f}_{H_q} \end{aligned} \tag{3.5}$$

The corresponding circuit equivalent is shown in Fig. 3.5, and is analogous to Fig. 2.8.

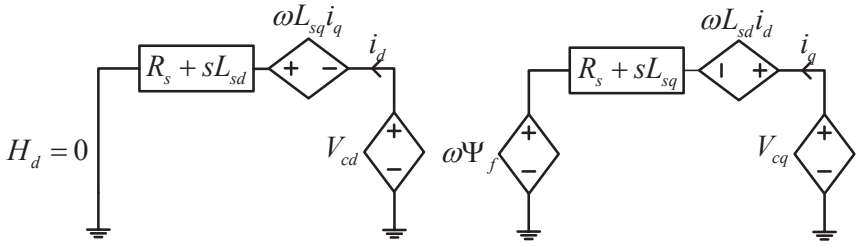

Fig. 3.5: PMSG circuit equivalent in the dq-frame

The torque can then be expressed as [35]:

$$T_e = p \cdot i_{qs}[i_{sd}(L_{sd} - L_{sq}) + \Psi_f] \approx p \cdot i_{sq} \Psi_f = J\frac{d\omega_m}{dt} - T_m \tag{3.6}$$

where p is the number of pole pairs, T_e is the electrical torque, and T_m is the mechanical torque. J is the combined inertia of the turbine and generator, while ω_m is the mechanical speed of the machine. Note that the torque is not dependent of i_d when saliency is neglected. These equations are used in developing the control structure.

3.5 Control of PMSG

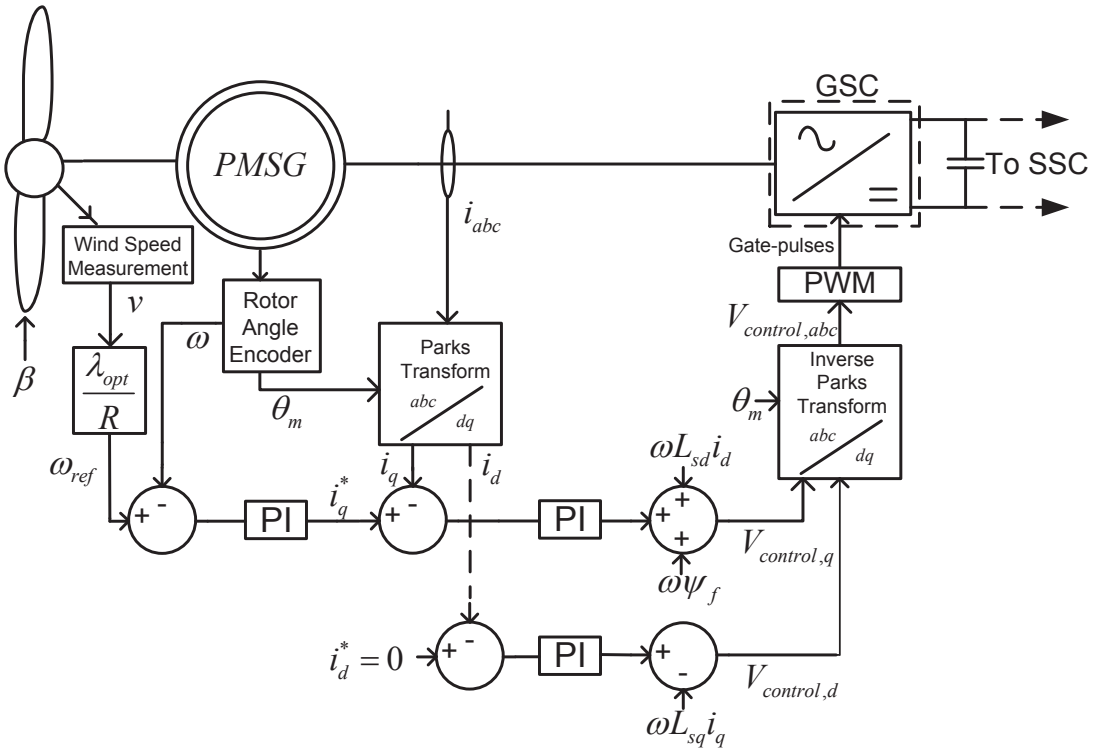

Fig. 3.6: Generator Side Converter (GSC) with control

The interaction between the PMSG and the converter will now be examined. The references [37], [38] and [39] give similar approaches to PMSG control in wind turbine applications. For convenience, the VSC connected to the PMSG is denoted Generator Side Converter (GSC), while the converter connected to the system is denoted System Side Converter (SSC). Fig. 3.6 shows the block diagram of the wind turbine and the GSC. The currents in the generator are measured, along with the rotor speed and position. The rotor angle is used as the transformation angle in the Park Transform. In this way, the requirement regarding that the transformation angle should be aligned with the rotor flux ψ_r is fulfilled. It is also assumed that the wind speed is measured. In practice this is a very hard task, so it can instead be estimated with sensorless control [39] [40].

The current control system is based on the method in section 2.7, and is similar to Fig. 2.7. The functions F_{dq}, G_{dq} and H_{dq} are substituted from (3.5). The reference of i_d is set to zero, that is $i_d^* = 0$. This will minimize the total current, and hence minimize the resistive losses in the stator. Another option is to use i_d to minimize the sum of all losses in the generator [37].

The control objective of the GSC is to extract maximum power from the wind. This requires a dynamic change in the generator speed, as discussed in section 3.1. Based on the constant optimal tip speed ratio λ_{opt}, the optimal speed reference can be calculated as $\omega_{ref} = \lambda_{opt}\frac{v}{R}$. Speed control is achieved by controlling the electrical torque, as seen from (3.6). An increase in the electrical torque will decelerate the machine. The relation between i_q and electrical torque is given in (3.6). The difference between the measured speed and reference speed will be applied to a PI-controller, where the output is used as the reference i_q^*. The complete block diagram is shown in Fig. 3.6.

3.6 System Side Converter Control

The SSC objectives are to control the DC-link voltage V_{DC} and the reactive power Q to the grid. Fig. 3.8 show the complete schematic including the control system. The structure is similar to the GSC-controller, with the similarities emphasized using the notation from section 2.7. The following model of the converter and grid is used [27] [26]:

$$\begin{aligned} v_{cd} &= \underbrace{(R+sL)}_{F_d(s)} i_d + \underbrace{-\omega L}_{G_d} i_q + \underbrace{v_{pd}}_{H_d} \\ v_{cq} &= \underbrace{(R+sL)}_{F_q(s)} i_q + \underbrace{\omega L}_{G_q} i_d + \underbrace{v_{pq}}_{H_q} \end{aligned} \tag{3.7}$$

where i_{dq} is the line current flowing out of the converter and ω is the system frequency in rad/s, while $v_{p,dq}$ and $v_{c,dq}$ are the voltages at the connection point and the converter terminals, respectively. L is an inductive filter with resistance R, and is connected between the converter and the voltage V_p. A step-up transformer in combination with a transmission line may provide enough filtering in some cases. The circuit equivalent of (3.7) is shown in Fig. 3.7. The complete schematic of the SSC is shown in Fig. 3.8.

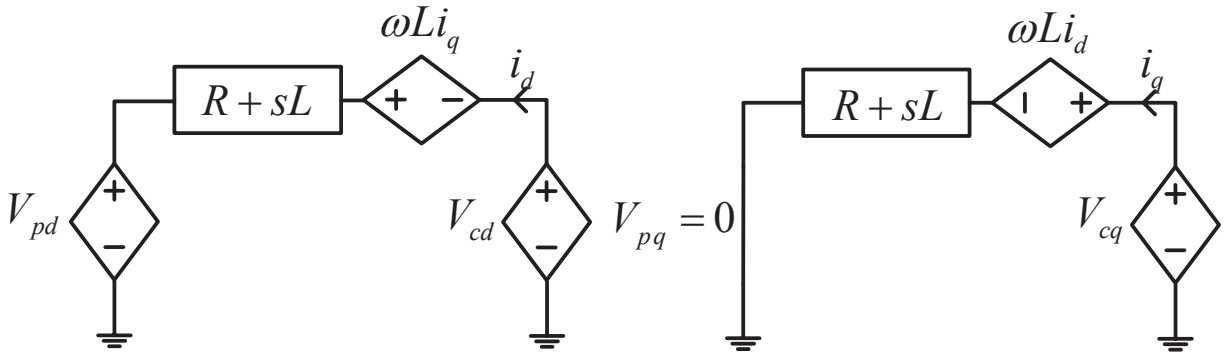

Fig. 3.7: SSC circuit equivalent in the dq-frame

The transformation angle is chosen as the phase angle in phase A of V_p. The angle is calculated through a Phase-Lock-Loop (PLL) based on the measured voltages. With this choice, $V_{pq} = 0$, which is a useful property in the control system. The following subsections describe how the DC-link voltage and reactive power is controlled.

3.6.1 DC-link voltage control

The DC-link voltage must be controlled in order to have a proper operation of the back-to-back converter. The wind turbine is allowed to inject any amount of active power in the converter at all times. An imbalance between the energy entering the GSC and leaving the SSC will accumulate in the DC-link capacitive storage, so a control function is required in order to keep the DC-voltage within specified limits. The equations leading to the control structure are given below. Refer to [41] and [42] for more thorough derivations, but keep in mind that these references use absolute quantities in contrast to the per-unit system that is used in this thesis.

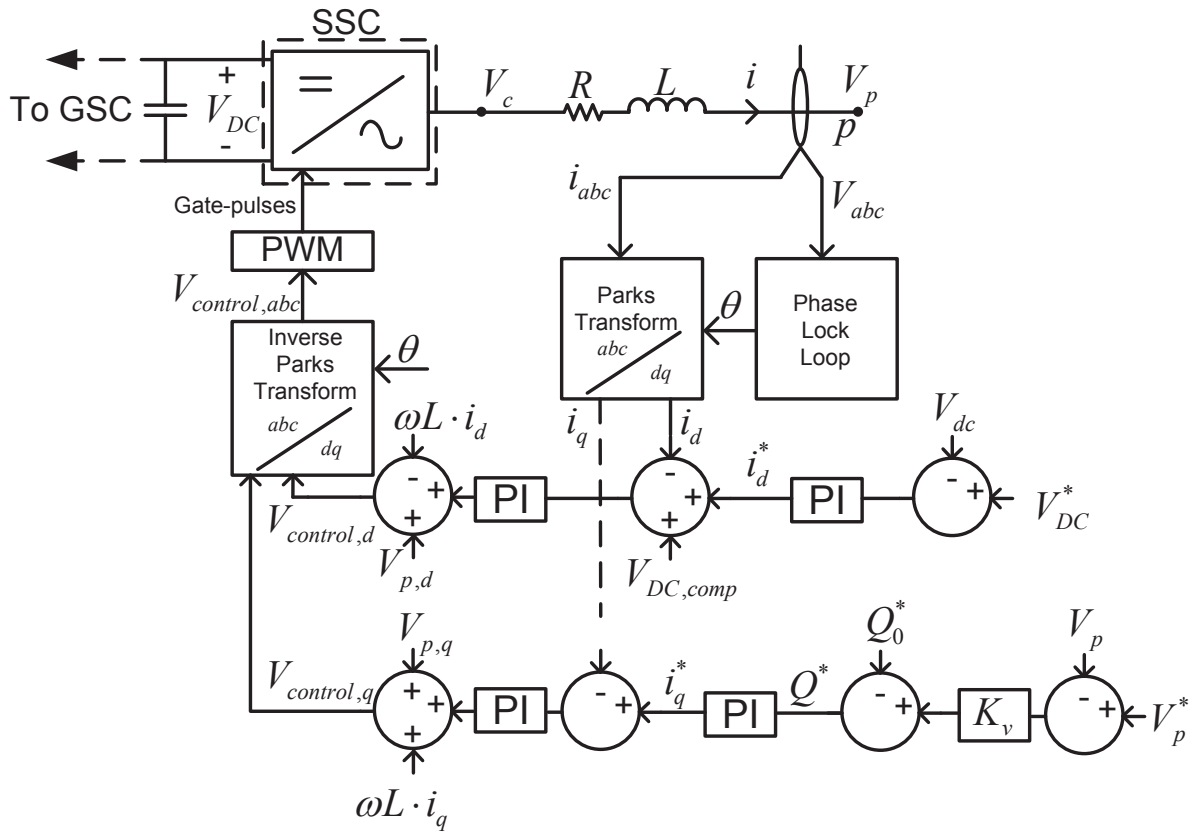

Fig. 3.8: System Side Converter (SSC) with control

Fig. 3.9 shows the per phase equivalent of the VSC. The per unit apparent power at the connection point p can be written in terms of the dq-equivalent in Fig. 3.7:

$$\begin{aligned} S_p &= (V_{pd} + jV_{pq})(i_{pd} + j \cdot i_{pq})^* = (V_{pd}i_{pd} - 0 \cdot i_{pq}) + j(V_{pd}i_{pq} + 0 \cdot i_{pd}) \\ P_p &= V_{pd}i_{pd} \\ Q_p &= V_{pd}i_{pq} \end{aligned} \tag{3.8}$$

Neglecting the losses in the filter resistance R and the IGBTs, this power is the same power that enters the DC-side of the SSC. The power that is flowing to the other side of the DC-link is equal to $P_{DC} = V_{DC}i_{DC}$, see Fig. 3.9. The power balance is given as:

$$\begin{aligned} P_p + P_C + P_{DC} &= 0 \\ \frac{dW_C}{dt} &= -P_p - P_{DC} \end{aligned} \tag{3.9}$$

The difference between P_p and P_{DC} is called P_C, and is the power absorbed in the capacitor C. P_c can be written as the time-derivative of the stored energy W_c in the capacitor. This gives the following relations:

$$\begin{aligned} P_C &= \frac{dW_C}{dt} = \frac{d}{dt}(\frac{1}{2}CV_{DC}^2) = C \cdot V_{DC}\frac{dV_{DC}}{dt} \\ C \cdot V_{DC}\frac{dV_{DC}}{dt} &= -V_{pd}i_d - V_{DC}i_{DC} \end{aligned} \tag{3.10}$$

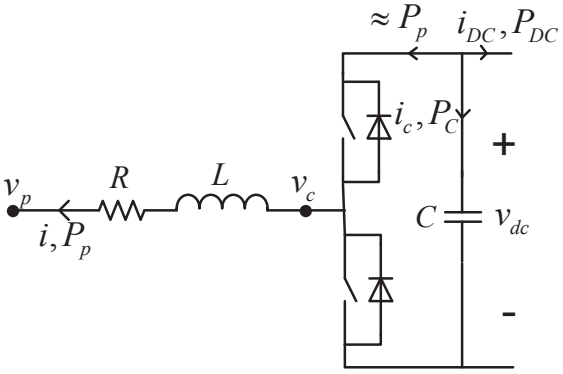

Fig. 3.9: VSC model

Since VSC controls the currents i_d and i_q independently, the i_d-controller should be used to control V_{DC} according to (3.9). The transfer function between V_{DC} and i_d is found taking the Taylor expansion of (3.9) [41]:

$$\frac{V_{DC}}{i_d}(s) = -\frac{v_{pd}}{V_{DC}^* sC} \tag{3.11}$$

The DC-link control system is shown in Fig. 3.8. The difference between V_{DC} and its reference is fed to a PI-regulator which produces the reference current i_d^*. [41]. The feed-forward term $V_{DC,comp} = -\frac{i_{DC}V_{DC}}{V_{pd}}$ compensates for load variations, and is calculated from the condition $P_p + P_{DC} = 0$ in steady state [41]. Note that an effective controller requires small variations in the voltages V_{pd} and V_{DC} as they are assumed constant during the linearization leading to (3.11).

3.6.2 Reactive Power Control

The ability to control i_q independently of i_d can be utilized for various purposes. To modify control strategies requires only software manipulation, so expensive changes in hardware and physical equipment are not required. In a strong power grid equipped with other reactive compensating units, there is no need for a dynamic reactive power control in the converter. It can then be set to operate at unity power factor, hence $Q^* = 0$. However, offshore power systems are not viewed as strong, so the different SSC control strategies should be examined.

The oil platform in System 1 contains a synchronous generator equipped with an Automatic Voltage Regulator (AVR). The AVR will adjust the reactive power production in order to have a desired terminal voltage. It is important to mark that the transient response of an AVR is not as good as the voltage source converter, due to the large time-delay associated with the field winding and excitation system. It therefore seems beneficial to let the units cooperate with the voltage control. However, the choice of control strategy is important when several inverters acts in parallel with an AVR. Only one unit should be responsible for eliminating the steady-state error, or in other words, utilize an integrator in its voltage feedback loop. Multiple controllers that tries to integrate the same error will never be able to reach steady-state, since even the smallest inconsistency between reference and measurement will create a high output when it is integrated over a certain time interval. It is natural that the AVR on the oil platform contains the integrator circuit, since it has much larger rating than a single wind turbine.

A proportional voltage controller will be used in the wind turbines, also referred to as voltage-droop in [43]. During a voltage disturbance, each wind turbine will adjust its reactive power production in order to bring the voltage back to its reference value. This feature will dampen the voltage oscillations that occur for instance during a motor start, and this will be shown in the simulation section 5.3.

The voltage-droop control implementation is shown in Fig. 3.8, where K_v is the droop constant. Q_0^* is the offset, representing the reactive power production when the voltage is equal to the reference. If the system is more likely to have a voltage dip than an overshoot, Q_0^* can be set to a negative value in order to increase its up-regulating capacity, and vice versa. Q_0^* can also compensate for the reactive power production or consumption in the sea cable, for instance to make the wind farm reactive power seen from the oil platform equal to zero.

An important limitation with the reactive power compensation from shunt-units like the VSC and STATCOM is that the current can not exceed its rated value. This raises the question whether it is economically feasible to over-rate the SSC current capability such that voltage support can be achieved even with maximum active power production. If the reactive current is allowed first priority, the surplus active power will accumulate in the wind turbine rotor and bring the rotational speed above the nominal value. As a simplification, the SSC is assumed to have the possibility of delivering rated reactive power at all times. This is equivalent to a total current rating of $\sqrt{2}$ times the active power current rating.

Another limitation is related to the support in low-voltage disturbances. Since the maximum current is fixed, the reactive power capability is proportional to the grid voltage, $Q_{max} = i_{rated} \cdot V_p$. Consequently, the SSC can only provide a limited amount of reactive power during a voltage dip, and almost no reactive power during a grid fault. This problem will be investigated during simulation studies in section 5.3

3.7 Submarine Cable Transmission

The transmission system between the wind farm and oil platform will influence the reactive power flow due to its inductive and capacitive properties. This is elaborated in the following section. The numerical data used in the simulations are found in [29]. See Fig. 3.10 for a schematic of the PI-equivalent that is used. The cable resistance is omitted since the transmission losses is out of the scope of the thesis.

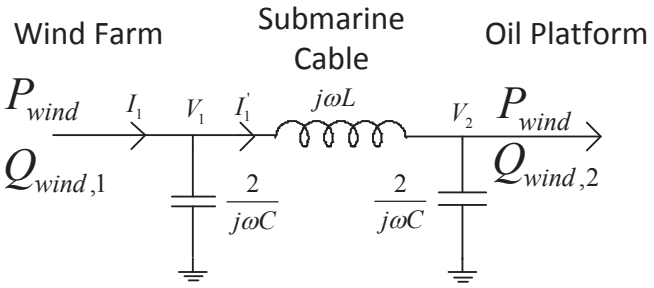

Fig. 3.10: Submarine Cable Equivalent

The reactive power entering the oil platform is denoted $Q_{wind,2}$ and calculated as follows:

$$
\begin{aligned}
I_1 &= \frac{P_{wind}}{V_1} - j\frac{Q_{wind,1}}{V_1} \\
I_1' &= \frac{P_{wind}}{V_1} - j\left(\frac{Q_{wind,1}}{V_1} + \frac{\omega C V_1}{2}\right) \\
Q_{wind,2} &= Q_{wind,1} - \omega L|I_1'|^2 + \frac{\omega C V_1^2}{2} + \frac{\omega C V_2^2}{2} \\
Q_{wind,2} &= Q_{wind,1} - \omega L\left(\left(\frac{P_{wind}}{|V_1|}\right)^2 + \left(\frac{Q_{wind,1}}{|V_1|} + \frac{\omega C|V_1|}{2}\right)^2\right) + \frac{\omega C|V_1|^2}{2} + \frac{\omega C|V_2|^2}{2}
\end{aligned}
\tag{3.12}
$$

where all the variables are recognized from Fig. 3.10. V_1 is chosen as the phase angle reference. A simplified expression is developed, where the voltage drop is neglected such that $|V_1| = |V_2| = V$. In addition, the term $\frac{\omega C V_1}{2}$ is neglected. It represents the inductive current that is caused by the capacitive current, and will be dominated by other terms. The following expression is obtained:

$$
Q_{wind,2} = Q_{wind,1} - \omega L\left(\left(\frac{P_{wind}}{V}\right)^2 + \left(\frac{Q_{wind,1}}{V}\right)^2\right) + \omega C V^2 \tag{3.13}
$$

Numerical values need to be inserted in order to determine whether the cable produces or consumes reactive power. In submarine cable transmissions, the capacitance normally dominates so that $Q_{wind,2} > Q_{wind,1}$. However, the reactive power from the cable is very sensitive to changes in the voltage, as all terms in (3.13) contain V^2. Even a small decrease in V will lead to a large increase in $Q_{wind,2}$, since the inductance will consume more, while the capacitance will produce less.

3.8 Oil Platform Gas Turbine

The gas turbine model is an important part of the system. Several gas turbine models exist, see [44] for an overview with comparisons. In this work, the Rowen model described in [45] and [46] is used. See Fig. 3.11 for a block diagram of the model.

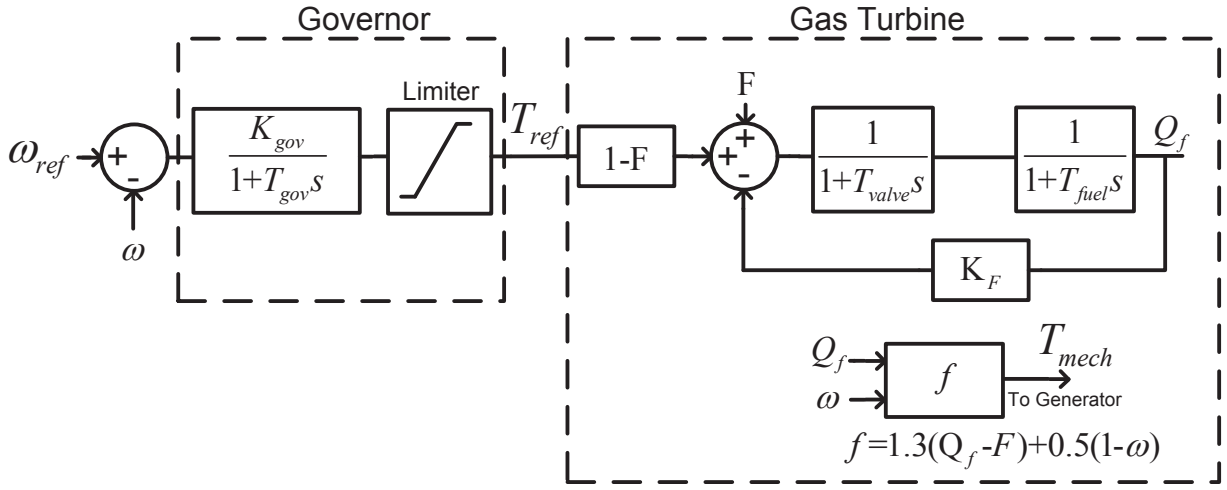

Fig. 3.11: Gas Turbine Model

The left of Fig. 3.11 shows the governor. The governor gives an output that is proportional to the deviation between the actual speed ω and the reference speed ω_{ref}, with a small governor sampling time delay T_{gov}. The number F is the fraction of the fuel flow that is needed to have rated speed when the turbine is running at no-load. The remaining fraction is multiplied with the governor output. The fuel system has two dominant time constants, here referred to as T_{valve} and T_{fuel}. T_{valve} models the valve positioner, and is the time required to open the valves from zero to maximum. T_{fuel} is the time delay associated with the fluid processes such as viscous friction. K_F is the fuel system feedback, which can be approximated to zero [46].

3.9 Oil Platform Synchronous Generator

The synchronous generator is a complicated machinery. Elements such as armature windings, field windings and damper windings should all be a part of the model. In addition there are saturation phenomena associated with the iron. The model used in this project is based on the standard synchronous generator from the PSCAD^{TM} library, which incorporates all key properties of the generator. Data for the resistances, reactances and unsaturated time-constants are found in [47] and given in appendix F.

Some equations describing the power flow in the generator are given here because they will facilitate the discussion and conclusion sections. The steady-state active and reactive power in a non-salient synchronous generator is equal to [48]:

$$P_{gen} = \frac{E_f V_t \sin\delta}{X} \tag{3.14}$$

$$Q_{gen} = V_t \frac{E_f \cos\delta - V_t}{X} \tag{3.15}$$

where E_f is the back-induced voltage, V_t is the terminal voltage, δ is the power angle, while X is the equivalent reactance between E_f and V_t.

The following paragraph contains an explanation to why the terminal voltage V_t will normally increase right after a disconnection of the wind farm. This fact will be verified with simulations. Consider a sudden increase in P_{gen}, for example after a disconnection of all wind power. The reactive power Q_{gen} is assumed to have small variations. The voltage E_f will remain constant until the excitation system starts to react. The time-delay of the exciter lies in the range of 1 s [25]. The term $(V_t \sin\delta)$ must therefore increase with a factor equal to the increase in P_{gen}. If the change in reactive power after the disturbance is small, for instance if the wind farm produces zero reactive power, the term $(V_t E_f \cos\delta - V_t^2)$ must remain constant. Observe that an increase in δ is required, and that δ is positive in generator operation. The increase in δ will shift the $Q - V_t$ characteristic to the right such that V_t must normally be increased in order to fulfill the condition of constant Q_{gen}. This can also be shown by taking the partial derivative of (3.15) with respect to δ. If Q_{gen} is assumed constant, the following expression is obtained: $\frac{\partial V_t}{\partial \delta} = \frac{V_t E_f \sin\delta}{2V_t - E\cos\delta}$. The derivative $\frac{\partial V_t}{\partial \delta}$ is positive if $2V_t > E\cos\delta$. If this condition is not satisfied, the generator reactive power will be larger than rated, since $Q_{gen} = V_t \frac{E_f \cos\delta - V_t}{X} > V_t \frac{2V_t - V_t}{X} = \frac{V_t^2}{X} >> 1 \quad pu.$ The derivative $\frac{\partial V_t}{\partial \delta}$ is therefore normally positive, implying that V_T increases if δ increases.

The above discussion explains that the terminal voltage on the platform will increase right after a disconnection of the wind farm. The generator would like to settle in a state with higher V_t, but after a certain time-delay, the AVR and excitation system will increase E_f such that V_t is reduced back to its reference value.

3.10 Oil Platform Induction Motors

As mentioned in the introduction, the System 1 oil platform only uses directly connected induction motors as load. This section explains the most relevant features of an induction motor.

The induced torque τ_{ind} in an induction motor in steady-state is given by [48]:

$$\tau_{ind} = \frac{3V_{TH}^2 \cdot R_2/s}{\omega_{sync}[(R_{TH} + R_2/s)^2 + (X_{TH} + X_2)^2]} \tag{3.16}$$

V_{TH}, R_{TH} and X_{TH} is the Thevenin equivalent voltage, resistance and reactance, seen from the rotor into the grid, respectively. ω_{sync} is the synchronous speed, ω_m is the mechanical speed of the rotor and $s = \frac{\omega_{sync} - \omega_m}{\omega_{sync}}$ is the slip. R_2 and X_2 is the rotor resistance and leakage reactance, respectively. The power that is converted from electrical to mechanical can be found from $P_{conv} = \omega_m \cdot \tau_{ind}$.

See appendix I for a plot where the torque-speed curve is shown for different R_2.

3.10.1 Induction Motor Start-up

The current drawn from the motor during start-up is much larger than during rated operation. This is because the rotor needs to be magnetized and accelerated.

It is beneficial with a high value for τ_{ind} during start-up, as this will shorten the acceleration time of the motor. This is achieved with a high rotor resistance R_2, see appendix I. However, the rotor copper losses in the machine are proportional with R_2. Wound rotor motors have the possibility of varying the rotor resistance, such that both high starting torque and low losses during normal operation is achieved. Another solution is to use deep-bar or double-cage machines for the same purpose [48].

The load torque T_m has influence on the start-up transient. It is the difference between the electrical and load torque that accelerates the machine, so a smaller T_m will yield a faster acceleration. The load profile varies largely from application to application. In this project, a centrifugal load is applied, where $T_m = b + k\omega^2$. The centrifugal profile is a good approximation for loads like pumps and compressors, which both are very common on oil platforms. See appendix I for a plot of the profile.

The oil and gas installations in the North Sea use direct start on the motors that does not have frequency converters. This will create a voltage dip in the system. In order to decrease this dip, the voltage is sometimes raised right before starting, or capacitor banks are connected in parallel [49].

The parameters in (3.16) will affect the simulations to a large extent. The data for induction motors vary much from application to application. The typical per-unit values for a squirrel cage motor in the PSCAD-library are used in the simulations.

3.10.2 Voltage Disturbances - Recovery or Collapse?

The electrical systems in oil platforms are far weaker than a land based grid. Different events, such as fault and motor starts, may cause a voltage dip. The dip has effect on the rest of the load, which also is assumed to consist of induction motors. If the synchronous generator is not properly rated, the system may not recover from a large voltage dip. This is elaborated in the following discussion.

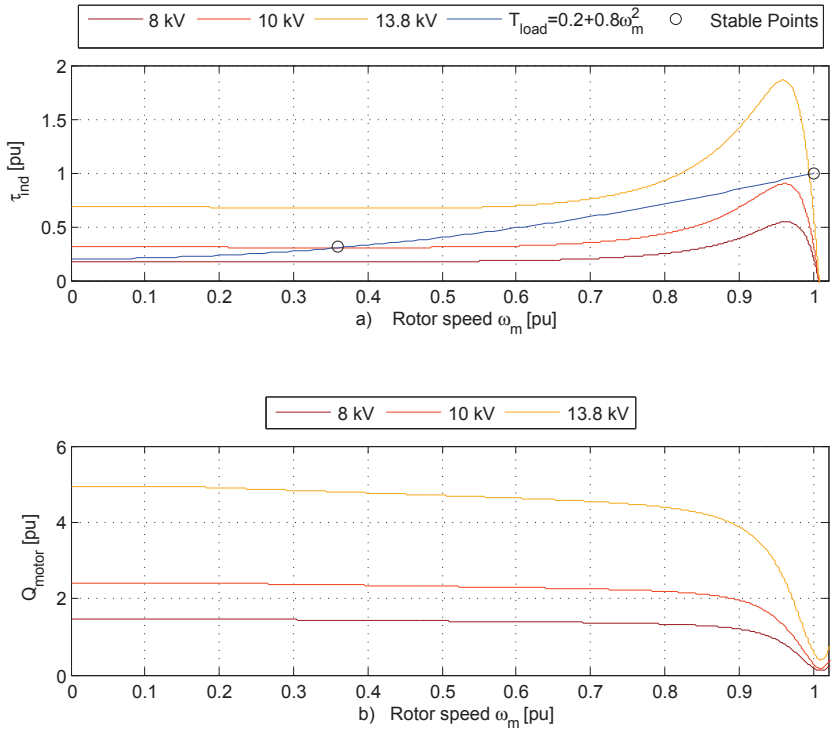

Fig. 3.12: Torque-speed curves for different terminal voltages

Fig. 3.12 a) shows torque-speed curves for a given motor where different terminal voltages are applied. The frequency is held constant. As the voltage drops, the torque-speed curve changes, since the induced torque τ_{ind} is proportional to V_{TH}^2. A decrease in the voltage will move the operating point to the left in Fig. 3.12 a). Since ω_{slip} increases, the reactive power consumed by the rotor of the induction motors increases. The total reactive power consumed by the motor is shown in Fig. 3.12 b). For example, if the voltage drops to 10 kV in Fig. 3.12 a), there is no stable operating point with ω_m higher than the speed corresponding to the pullout-torque. The motors will then settle in a state with $\omega_m = 0.36$ pu, where the reactive power consumed is about $Q_{motor} = 2.3$ pu. The synchronous generator needs to be sized according to this event, such that it can provide the necessary current in order to accelerate the motors back to nominal speed.

Note that platforms normally contain a mix of fixed-speed and variable-speed induction motors with frequency converters. It is reasonable to expect that the probability of a voltage collapse increases with a larger percentage of fixed speed motors, since the reactive power in variable-speed motors is locally generated by the motor side converter. If active inverters are employed, they may support reactive power during disturbances, hence increasing the voltage stability instead of being the cause to collapse. Refer to section 3.6.2 for a description on how this is achieved.

Chapter 4

System 2: Integrating wind power with Troll A

System 2 is based on an actual configuration in contrast to System 1. A collaboration with Statoil lead to this case study, where the goal is to examine the possibility of integrating offshore wind power with an existing oil platform. The choice fell on the platform Troll A, which has been operating since 1995, and has later become a pioneer by utilizing VSC-HVDC for controlling a large offshore motor. This chapter starts with a description of the Troll A platform, and continues with a discussion on how wind power can be integrated in the existing electrical system. An extensive section on the system models and control systems completes the chapter.

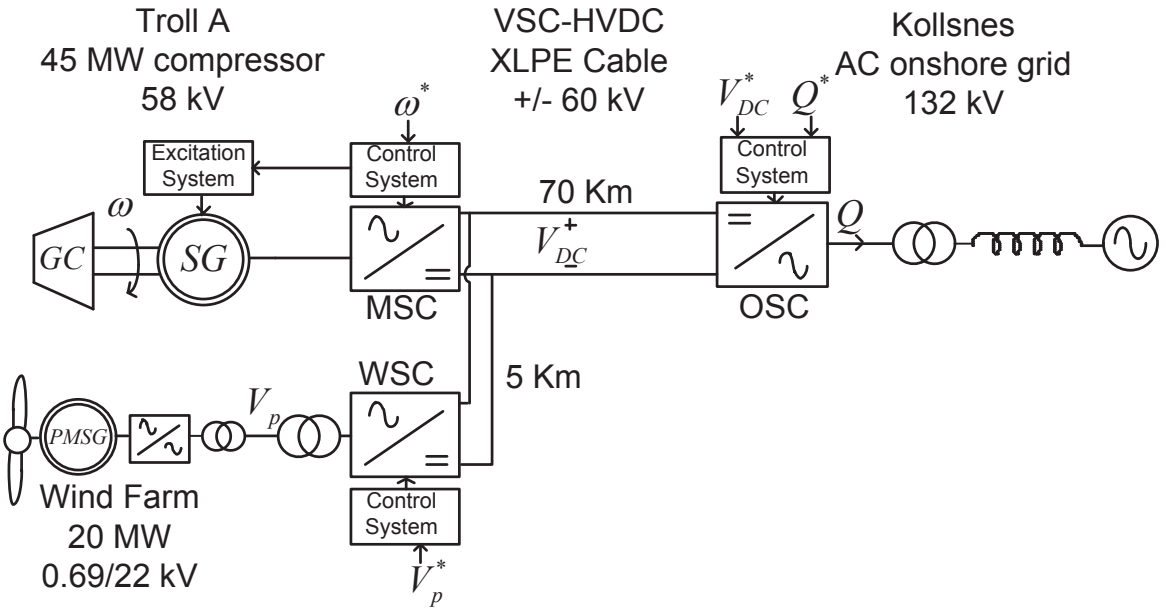

Fig. 4.1: System 2 Overview

4.1 Description of Troll A

The gas platform Troll A is operated by Statoil and lies in the North Sea. Two parallel VSC-HVDC transmissions between the platform and the onshore processing plant Kollnes were built in 2005 as the first HVDC transmission to an offshore facility in the world [50]-[51]. See Fig. 4.1 for a single line diagram of the system including the proposed wind power integration. Only one of the HVDC-systems are considered further in this thesis. The VSC on Kollsnes is denoted Onshore Side Converter (OSC), and controls the DC-cable voltage in order to maintain power balance between the converter stations. It can

also provide ancillary services to the onshore grid through its fast reactive power control. The VSC terminal on the platform, subsequently denoted Motor Side Converter (MSC), has the purpose of a regular variable speed motor drive, and is connected to a 45 MW synchronous motor. This motor is connected via a gear to a gas compressor that extracts gas from the reservoir and sends it to Kollnes through a pipeline. The reservoir pressure drops with time since the amount of gas is decreasing, and more compressors are needed in the coming years. Statoil has decided to build two new VSC-HVDC links that will be put into service in 2015/2016 in order to compensate for the falling reservoir pressure [49].

4.2 Wind Power Integration

From an offshore wind farm point of view it is favorable to interconnect with the Troll A platform, since it will utilize an already existing transmission system to shore. However, there are challenges concerning the technical solutions that must be implemented on the platform. Troll A produces gas that generates an income which completely outshine the profit that any wind farm can imagine to deliver. From the platform owner point of view it is therefore a requirement that the modifications that are done to the electrical system do not pose an increasing risk of shutdown or reduced availability for the compressor system.

The wind power can either be connected on the AC- or the DC-side of the MSC. The drawbacks with connecting to the AC-side lie in the expensive modifications required in the control strategy of the Synchronous Motor and compressor system. It is reasonable to believe that the robustness and stability of the system will be weakened if wind power is integrated on the AC-side. The protection system in the wind farm must be extremely reliable in order to avoid that any disturbances will affect the synchronous motor and thereby force a system shutdown.

To connect on the DC-side seems more promising regarding the system security. If the DC voltage stays within the imposed limits, the variable speed operation of the compressor will not be interrupted by the added wind power. The connection can be made in several ways, but the key problem is to transform the voltage from about 0.69 kV (AC) in the wind turbines to 120 kV which is the nominal DC-voltage. The transformation process should be done in AC because a DC/DC converter with this ratio is impractical. In addition, it is important to consider that Troll A has strict space requirements, so the transformers and converters must most likely be placed on a separate platform. A multi-terminal VSC solution is proposed in Fig. 4.1. The wind farm is represented by a single-turbine equivalent, including a PMSG with full converter. This is the same model that was used in System 1. The additional step-up transformer and VSC are placed on a common platform. The power is transferred to Troll A through a 5 km DC-cable. For more details on the models and control, see section 4.7.

4.3 Synchronous Motor Model

The dynamic equations describing a field excited Synchronous Motor (SM) are [24]:

$$\begin{aligned} v_{cd} &= R_s i_d - \omega_s \psi_{sq} + \frac{d\psi_{sd}}{dt} \\ v_{cq} &= R_s i_q + \omega_s \psi_{sd} + \frac{d\psi_{sq}}{dt} \\ v_f &= R_f i_f + \frac{d\psi_f}{dt} \end{aligned} \tag{4.1}$$

The flux linkages $\psi_{s,dq}$ and ψ_{fd} is expressed as [24]:

$$\begin{aligned} \psi_{sd} &= L_{sd} i_d + L_{md}(i_f + i_{rd}) \\ \psi_{sq} &= L_{sq} i_q + L_{mq} i_{rq} \\ \psi_{fd} &= L_f i_f + L_{md}(i_d + i_{rd}) \end{aligned} \tag{4.2}$$

And the electromagnetic torque T_{em} in the machine is expressed as [24]:

$$T_{em} = \frac{p}{2}[L_{md}(i_f + i_{rd})i_{sq} + (L_{sd} - L_{sq})i_{sd}i_{sq} - L_{mq}i_{rq}i_{sd}] \tag{4.3}$$

The variables occurring in the equations (4.1), (4.2) and (4.3) are summarized in Table 4.1. The model is similar to the PMSG that was treated in section 3.4. The differences are related to the field winding, where a controllable field voltage is applied in contrast to the constant flux produced by the magnets in the PMSG. In addition, damper windings can be included in both types of machines, but they are more common in the field excited SM. The reference [25] gives a detailed description on the physics behind the dynamical model, while [24] and [52] develop the equations that are required from a control point of view.

Table 4.1: Parameters in the Synchronous Motor Model

v_c	Terminal Voltage	L_s	Stator Self Inductance
R_s	Armature Resistance	L_m	Mutual Inductance
i	Stator Current *into* the Motor	L_r	Rotor Self Inductance
ω_s	Electrical Speed of Rotor	i_f	Field Winding Current
ψ_s	Stator Winding Flux Linkage	i_r	Damper Winding Current
ψ_f	Field Winding Flux Linkage	p	Number of Poles
L_f	Field Winding Self Inductance	T_{em}	Electromagnetic Torque
i_f	Field Winding Current	v_f	Field Winding Voltage

4.3.1 Simplifications

Some simplifications are made in order to develop the control system analytically. First, the damper winding currents are neglected, hence $i_{rd} = i_{rq} = 0$. The damper windings will be a part of the simulation model, but this approach omits their compensation terms in the control system. Secondly, the machine is assumed non-salient, i.e. $L_{sd} = L_{sq} = L_s$ and $L_{md} = L_{mq} = L_m$. This assumption is justified by the fact that machines connected to gas turbines or compressors are normally of round-rotor type, leading to similar inductances in both axes. As a last simplification, the armature resistance is neglected. The losses in the SM is not of no interest, so its role in the investigations is minor.

As the goal of these simulations is to investigate how wind power integration affects the operation of the synchronous motor, the simplifications will not produce large errors in the results. To design an optimal control system in the SM is out of the scope.

4.3.2 Simplified Model

Taking in to account the simplifications mentioned, the dynamical model is reduced to:

$$\begin{aligned} v_{cd} &= \omega_s \psi_{sq} + \frac{d\psi_{sd}}{dt} \\ v_{cq} &= \omega_s \psi_{sd} + \frac{d\psi_{sq}}{dt} \\ v_{fd} &= R_f i_f + \frac{d\psi_f}{dt} \end{aligned} \tag{4.4}$$

The flux linkages will be:

$$\begin{aligned} \psi_{sd} &= L_s i_d + L_m i_f \\ \psi_{sq} &= L_s i_q \\ \psi_{fd} &= L_f i_d + L_{md} i_d \end{aligned} \tag{4.5}$$

And the electromagnetic torque is simplified to:

$$T_{em} = \frac{p}{2} L_m i_f i_{sq} \tag{4.6}$$

Equation (4.4) is rearranged in order to match (2.2):

$$\begin{aligned} v_{cd} &= \underbrace{sL_s}_{F_d(s)} i_d + \underbrace{-\omega L_s}_{G_d} i_q + \underbrace{0}_{H_d} \\ v_{cq} &= \underbrace{sL_s}_{F_q(s)} i_q + \underbrace{\omega L_{sd}}_{G_q} i_d + \underbrace{L_m i_f}_{H_q} \end{aligned} \tag{4.7}$$

The control system of the synchronous motor will now be explained based on the given equations.

4.4 Synchronous Motor Control

One of the major benefits with the use of VSC-HVDC connection to Troll A is that the motor terminal voltage is fully controllable by the converter. Since no other application is connected to the offshore VSC terminal, the frequency and voltage can be exclusively used to fulfill the motor objectives. The main control objective is to adjust the rotational speed according to an external reference. This requirement arise because the gas pipe volumetric flow should be controlled according to how much the gas operator wants to deliver. Variable speed operation is beneficial in this respect as the pipe flow is a function of compressor speed. On the contrary, a fixed-speed operation requires maximal power at all times, where the surplus pressure has to be choked with a throttling valve. Adjustable speed operation introduces large energy savings, especially if the unit is operated at part load for a significant percentage of the time [24]. The complete schematic of the synchronous motor control system is shown in Fig. 4.2, and the different elements are explained in the following subsections.

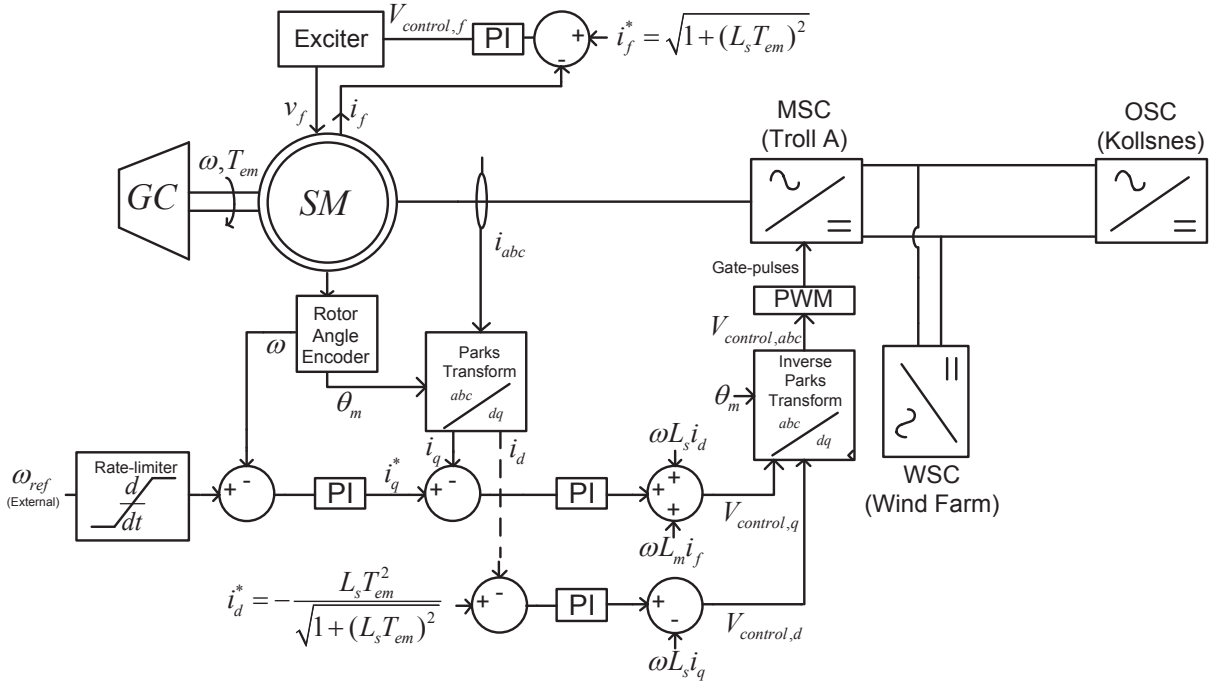

Fig. 4.2: System 2 block diagram with controls

4.4.1 Field Current Control

The control system of the SM has another degree of freedom compared with the PMSG, namely the field current i_f. It is controlled through the excitation voltage v_f. The exciter is assumed to be brushless, with rotating rectifiers according to the IEEE-model in [53]. A first order per unit approximation is applied:

$$\frac{v_f}{V_{control,f}}(s) = \frac{1}{1 + T_{fv}s} \tag{4.8}$$

where $V_{control,f}$ is the control signal. The time constant T_{fv} lies in the range of 0.5 - 1 s [25]. The response is slow because the excitation voltage v_f is only indirectly controlled through the field winding of the exciter. The field winding of the SM introduces a large time delay before the desired flux or field current is built up. This delay is given by the short-circuit transient d-axis time constant T'_{d0}. The complete block diagram for the field current control in per unit is shown in Fig. 4.3, while the control implementation is seen in Fig. 4.2. The bandwidth of the field current controller is limited by T'_{d0} such that it is hard to compensate for the influence from the fast dynamics of i_d [54].

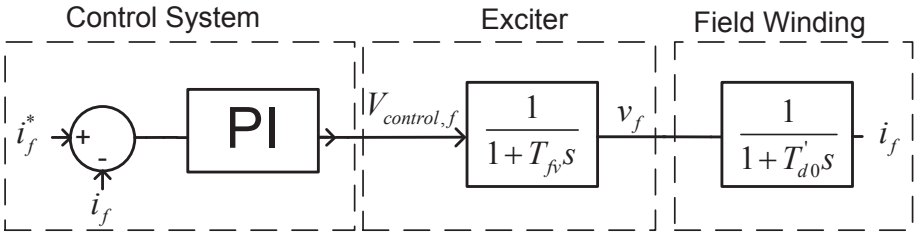

Fig. 4.3: Field Current Transfer Function

4.4.2 Stator Current Control

The stator currents are controlled in the same way as for both converters in sections 3.5 and 3.6. As (4.7) is only a special case of (2.2), the control structure is directly obtained from Fig. 2.7 and viewed in Fig. 4.2 and Fig. 4.4.

4.4.3 Speed Control

To control the rotational speed of the SM is assigned highest priority among the control objectives. When there is a desired change in the gas production, a new speed reference ω^* is sent to the drive system. Too rapid changes in speed should be avoided in order to protect the gear and compressor system, so a rate-limiter is applied as seen in Fig. 4.2. The speed is adjusted by increasing or decreasing the electrical torque T_{em}. This torque is proportional to both i_f and i_q as seen in (4.6), but only i_q is used in the speed control feedback since its controller reacts much faster. A centrifugal load profile is assumed, where the load torque $T_L = k\omega^2$. The current control loop is simplified to a first order transfer function with time constant T_q. See Fig. 4.5 for the closed loop block diagram of the speed control.

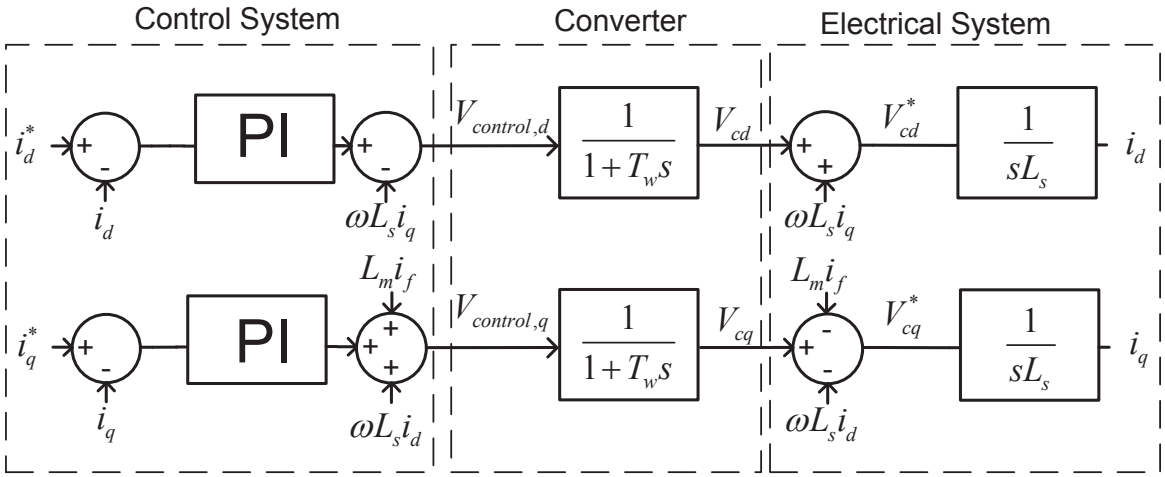

Fig. 4.4: Stator Currents Transfer Functions

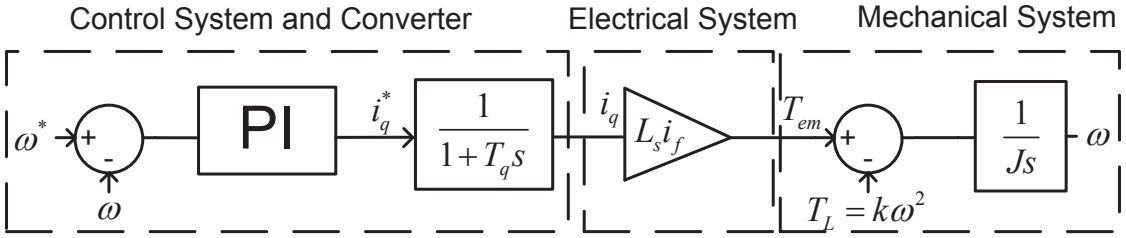

Fig. 4.5: Speed Control Transfer Functions

4.4.4 References of i_d and i_f

Two degrees of freedom can be utilized in addition to control the speed. One of them must be used to control the flux in the motor, and the other will be used to minimize the total stator current. The following strategies are proposed by the author.

The field magnitude $|\psi_s|$ is controlled to its rated value by keeping the ratio between the voltage and speed constant, that is $\frac{|v_c|}{\omega} = k$. This is shown from the following relations based on (4.4):

$$\begin{aligned} v_{cd} &= \omega_s \psi_{sq} + \overbrace{\frac{d\psi_{sd}}{dt}}^{=0} \\ v_{cq} &= \omega_s \psi_{sd} + \overbrace{\frac{d\psi_{sq}}{dt}}^{=0} \\ |v_c| &= \sqrt{v_{cd}^2 + v_{cq}^2} = \omega_s \sqrt{\psi_{sd}^2 + \psi_{sq}^2} = \omega_s |\psi_s| \end{aligned} \tag{4.9}$$

where the terms $\frac{d\psi_{sd}}{dt}$ and $\frac{d\psi_{sq}}{dt}$ are equal to zero in steady-state. To minimize the stator current is equivalent to:

$$min\{i_d^2 + i_q^2\} \tag{4.10}$$

The reference values i_d^* and i_f^* that fulfill both objectives are derived in appendix E based on (4.10) and (4.9) and the simplified model in (4.4). The reference field current is:

$$i_f^* = \sqrt{1 + (L_s T_{em})^2} \tag{4.11}$$

while the reference d-axis current is:

$$i_d^* = -\frac{L_s T_{em}^2}{\sqrt{(L_s T_{em})^2 + 1}} \tag{4.12}$$

These equations finalize the control structure for the motor, and the complete schematic for the motor and converter is shown in fig. 4.2. The main weakness of the chosen control strategy lies in the lack of feedback to ensure that both rated flux and minimized current are achieved. However, both objectives are confirmed in the simulations, but other approaches should be sought in a real implementation.

4.5 DC Network modeling

The capacitance in the DC-cables is vital with respect to the DC voltage control. A low capacitance means that the cable is easily discharged, and the control system must react faster in order to keep the voltage within the limits. It is assumed that the cable provides enough capacitance, such that none additional capacitors are installed on either of the terminals. The inductance and resistance in the cable also affects the dynamics, and should be modeled with accuracy. A high cable inductance will create a time-delay before a change in voltage on one side is present on the other side, since a voltage $v_L = \frac{di}{dt}$ is induced to compensate for the change in voltage. The two cables are 80 kV ABB XLPE-technology, but the system is operated at ±60 kV. The following cable data are obtained from a request to ABB:

$$\begin{aligned} C &= 0.26[\tfrac{\mu F}{km}] \cdot 70km &&= 19.6 \quad \mu F \\ R &= 0.1[\tfrac{\Omega}{km}] \cdot 70km &&= 7 \quad \Omega \\ L &= 0.18[\tfrac{mH}{km}] \cdot 70km &&= 12.6 \quad mH \end{aligned} \tag{4.13}$$

Regarding the proposed 5 km cable from Troll A to the Wind Farm, the same values are scaled with $\frac{5}{70}$, resulting in the following parameters:

$$\begin{aligned} C_w &= 19.6 \cdot \tfrac{5}{70} &&= 1.4\mu F \\ R_w &= 7 \cdot \tfrac{5}{70} &&= 0.5 \quad \Omega \\ L_w &= 12.6 \cdot \tfrac{5}{70} &&= 0.893 \quad mH \end{aligned} \tag{4.14}$$

The complete DC-network model shown in Fig. 4.6.

The losses in the HVDC-cable can be calculated under steady-state conditions:

$$\begin{aligned} P_{loss} &= 2R \cdot I_{DC}^2 \\ &= 2R \cdot \left(\frac{P_T}{V_T}\right)^2 \end{aligned} \tag{4.15}$$

where V_T is the DC-voltage at Troll A, I_{DC} is the current in the cables, and P_T is the active power at the Troll connection point, see Fig. 4.6. Equation (4.15) can be used to plot the cable losses for variable power demand P_T and constant voltage at Kollsnes, see Fig. 4.7. The blue line shows (4.15), while the black line shows a simulation scatter plot. The two curves are seen to be equal, hence validating (4.15). The figure illustrates an important benefit with the wind power integration. If the Synchronous Motor consumes 45 MW, the

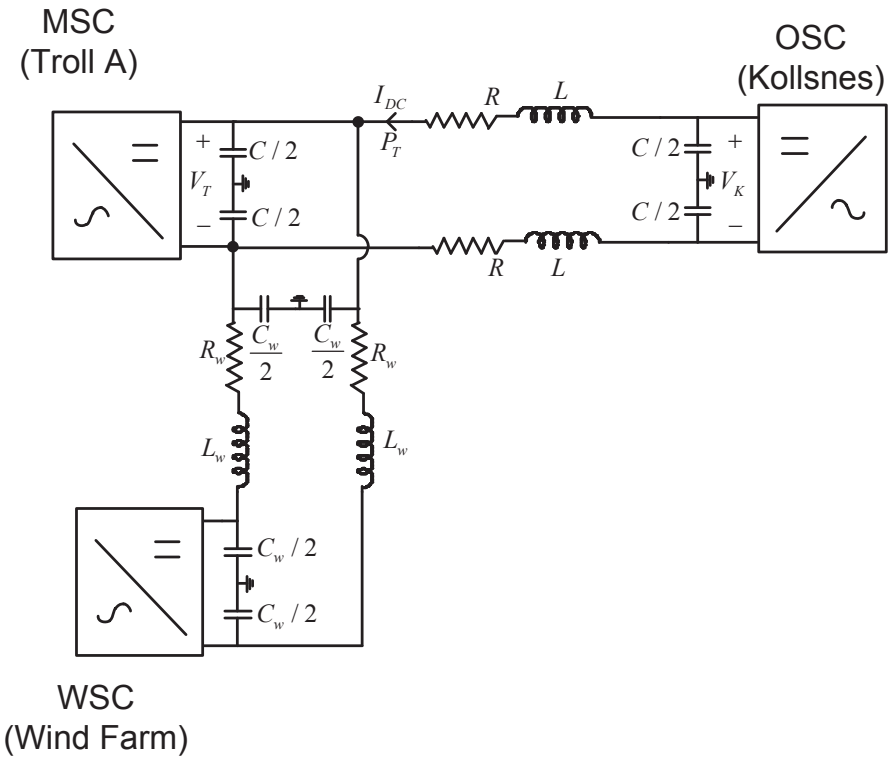

Fig. 4.6: DC-network model

losses are $P_{loss} = 2.0$ MW without any wind power. If 20 MW wind is injected to the DC-cable, the active power $P_T = 45 - 20 = 25$ MW, and the losses are reduced with 1.4 MW to $P_{loss} = 0.6$ MW. The losses in the WSC and transmission system of the wind farm is not taken into consideration in this calculation, since an offshore wind farm will have transmission losses regardless of how it is integrated to the grid. It is remarked that the losses in the HVDC-cable are large, partly because the cable is operated at a lower voltage than the design limit.

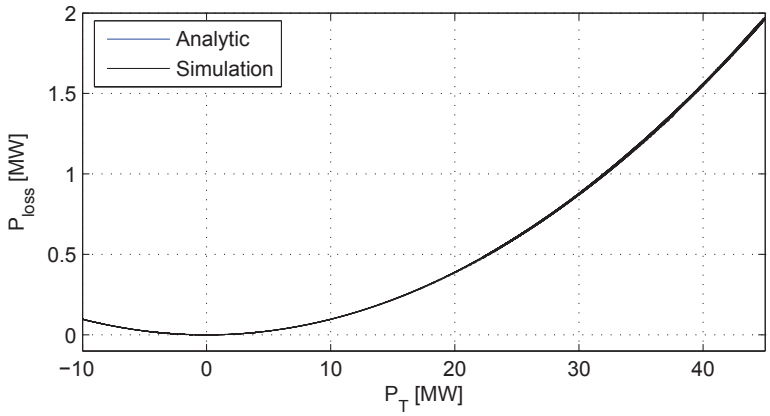

Fig. 4.7: Loss in HVDC-cable, from equation (4.15) and simulation

4.6 Onshore Side Converter Control

The VSC located at Kollsnes will be used to control the DC-cable voltage and the reactive power to the grid. The control structure is almost equal to the SSC in section 3.6, and the models and equations will not be repeated here. The compensation element $V_{DC,comp}$ is omitted because it is impossible to separate the charging current from the load current. Also, the resistive cable drop for each of the cables is estimated and compensated for with the term $2R \cdot I_{DC}$. With this strategy, the OSC will keep the voltage at the MSC constant, as long as the parameters and measurements are correct. Fig. 4.8 shows the block diagram of the OSC.

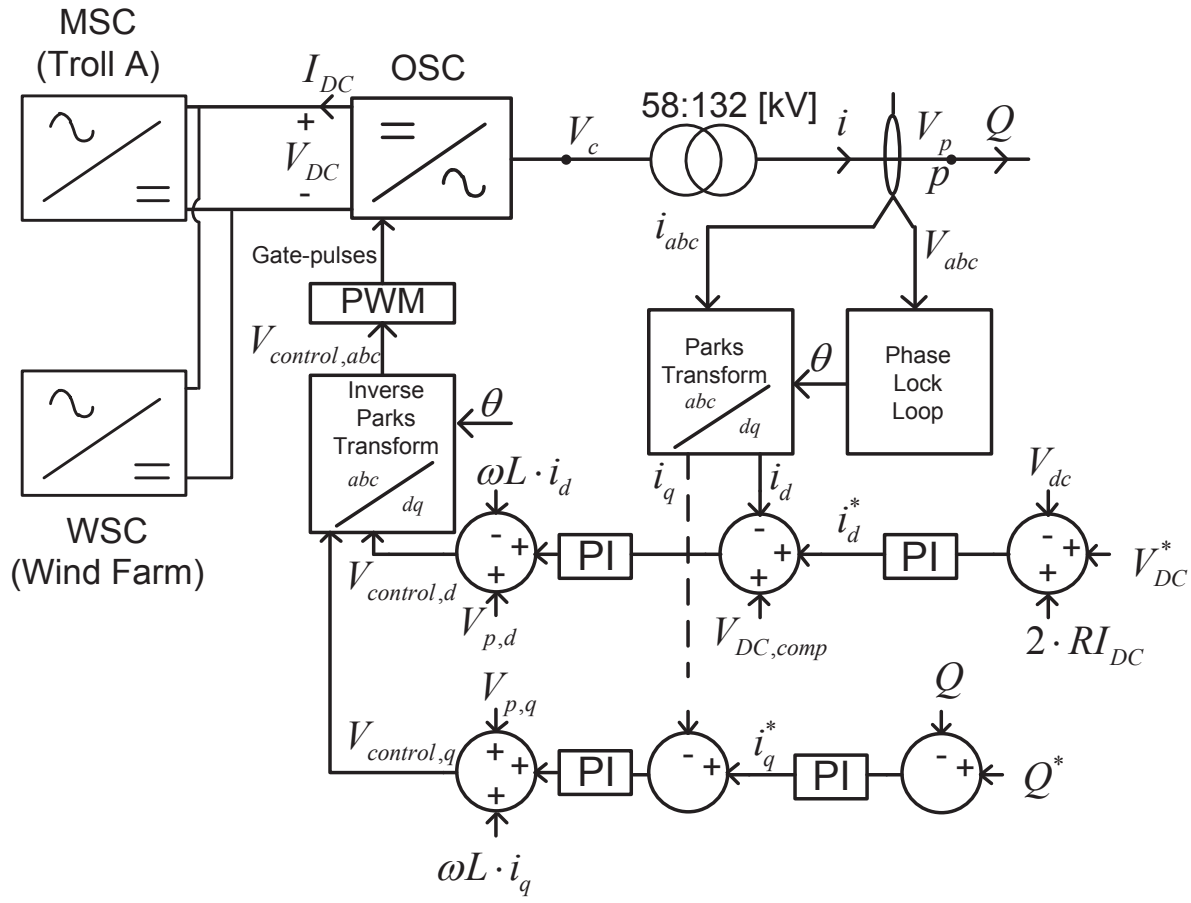

Fig. 4.8: Onshore Side Converter Block Diagram With Controls

The converter is actually implemented with LCL-filters on the AC-side, but these are omitted in this model since harmonics are neglected. The transformer series inductance and resistance are the equivalent L and R in the corresponding Fig. 3.8.

4.7 Wind Side Converter Control

The details behind the wind farm integration are now given, refer to Fig. 4.9. The wind turbine model is the same as in System 1, so that sections 3.1-3.6 can be used as a reference. This section will mainly focus on the VSC between the wind farm and the platform. For convenience, it is denoted Wind Side Converter (WSC). Its main objective is to provide a voltage that is constant in magnitude in the wind farm. In this way, the control system in the wind turbines will have stable conditions, and be able to deliver maximum power according to the strategy from section 3.5. The WSC will not contribute to DC-link control since the active power flow is decided by the wind turbine, and hence not controllable.

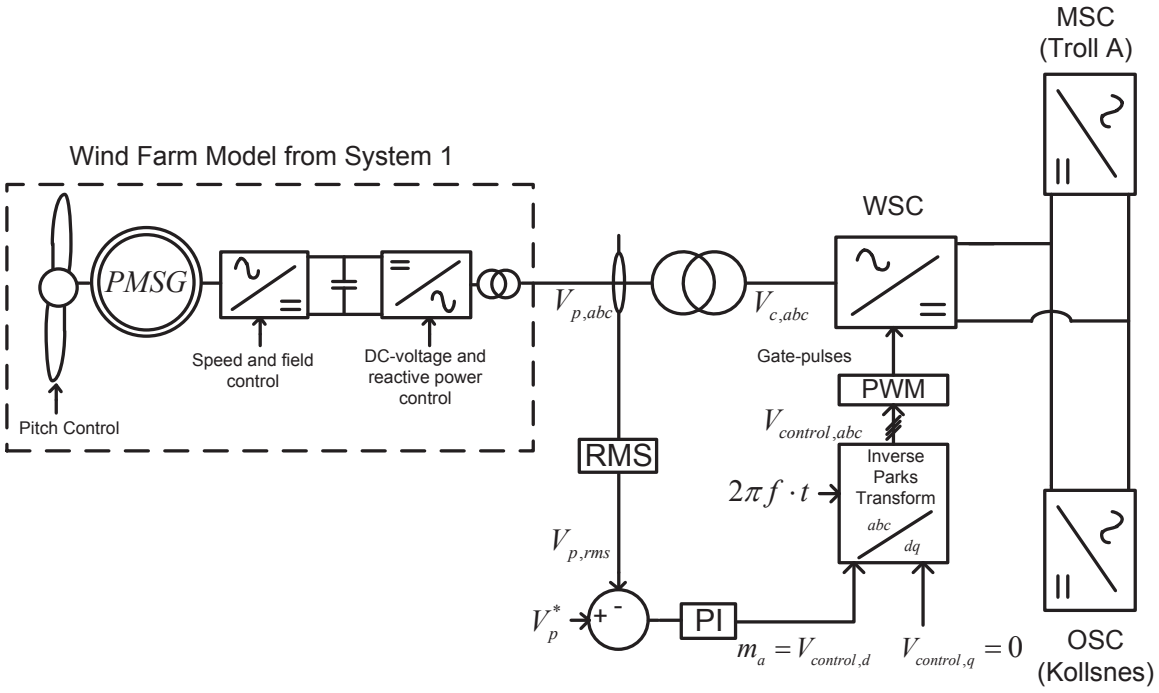

Fig. 4.9: Wind Farm Connection Proposal

Control of the AC voltage magnitude is done in the same way as [10], refer also to [42] for a mathematical derivation of the strategy. The voltage V_p is controlled through the modulation index $m_a = \frac{(\hat{V}_{c,an})_1}{\frac{V_{DC}}{2}}$, where $(\hat{V}_{c,an})_1$ is the peak of the fundamental harmonic in the line-to-neutral converter voltage V_c [20]. The transformer is used as an inductive filter, and no extra filtering is considered since the model neglects harmonics. The control block diagram is shown in Fig. 4.9, where m_a is used as $V_{control,d}$, while $V_{control,q} = 0$. Substitute this into (A.2) in appendix A and yield:

$$\begin{bmatrix} v_{c,a} \\ v_{c,b} \\ v_{c,c} \end{bmatrix} = V_{c,nominal} \cdot m_a \cdot \begin{bmatrix} \cos(2\pi f \cdot t) \\ \cos((2\pi f \cdot t - \frac{2\pi}{3})) \\ \cos((2\pi f \cdot t + \frac{2\pi}{3})) \end{bmatrix} \tag{4.16}$$

The output sent to the PWM is seen to be a balanced set of three-phase voltages, with amplitude $V_{c,nominal} \cdot m_a$. The transfer function between V_p and V_c depends on the dynamics of the rest of the system [42]. Because of this dependency, the PI-controller in Fig. 4.9 is tuned experimentally.

Chapter 5

Simulations on System 1

This chapter contains simulations on System 1. Section 5.1 gives the most important numerical data used in the simulation. Simulations representing normal system operation including wind speed fluctuations and induction motor start are presented in section 5.2. Testing and discussions regarding reactive support in the wind farm is covered in section 5.3 and section 5.4. The final simulation case concerns sudden loss of wind power, and is found in section 5.5. The chapter is concluded with a discussion in section 5.6.

5.1 Numerical Parameters

The most important numerical parameters in System 1 are given in Table 5.1 and Table 5.2. See appendix F for additional parameters.

Parameter	**Value**
Rating	20 MW
Terminal Voltage	690 V
Generator Side Rated Frequency	50 Hz
System Side Rated Frequency	60 Hz
Grid Side Filter L	9.497 μH =0.15 pu
Grid Side Filter R	0.2384 m Ω = 0.01 pu
DC-link Capacitor	$0.08F$ = 2.53 ms
Total Turbine Inertia	5s

Table 5.1: Wind Turbine Parameters

Parameter	**Value**
Generator Rating	50 MW
Maximum Load	40 MW
Platform Voltage	13.8 kV
Platform Frequency	60 Hz
Governor Droop K_{gov}	25 pu
Fuel Time Constant T_{fuel}	0.4s
Generator Inertia	3s
Transmission Cable Length	10 km
Transmission Cable Inductance	3.5 mH
Transmission Cable Capacitance	2.6 μF

Table 5.2: Oil Platform and Transmission Parameters

5.2 Normal System Operation

This section presents simulations during normal operation of System 1. The wind profile from section 5.1 is applied. The platform has initially 30 MW of induction motor load running, and at $t = 60$ s, an additional 5 MW motor is started. The simulation results are presented in two parts. In the first part the focus lies within the wind farm, in order to examine the overall performance of the control system. The second part is devoted to the total system, where the active and reactive powers are shown, in addition to the system voltage and frequency.

Generator Side Variables

The performance of the wind farm under variable wind conditions is now evaluated. The wind profile from section 5.1 is applied, and the simulation has a duration of 100 s. The behavior of the wind farm is described with respect to the different periods. Fig. 5.1 shows the simulation results.

Wind Speed Below Rated ($t < 45s$)

The generator speed reference is constantly changing, and the speed controller attempts to minimize the error. Due to the large inertia of the turbine, there are no rapid changes in ω, see Fig. 5.1 b). The active power is fluctuating because it is used to accelerate and decelerate the generator according to the deviation between ω and ω^*, see Fig. 5.1 c). Lastly, it is observed that the pitch control is not active when the wind speed is below rated, and this is according to the chosen control strategy from section 3.2.

Wind speed Gust ($10 < t < 20$)

The gust is a rapid change in the wind speed, and it is seen in Fig. 5.1 b) that ω^* is dropping as the wind speed decreases. The speed controller is able to adjust ω according to ω^* with a small time-delay. The decrease in mechanical torque contributes to the deceleration, and in addition the electrical torque is increased in order to keep better track of ω^*. When the wind speed increases back to the pre-gust value, there is a time-delay between the speed and its reference caused by the inertia and the relatively slow control system. The control system could have been made faster, but this would introduce larger power fluctuations to the grid.

Wind Speed Above Rated ($t > 45$ s)

When the mean wind speed is larger than 12 m/s, the mechanical torque exceeds the rated value. This enables the pitch control described in section 3.2, and it is seen that both ω and P are eventually limited to 1 pu. A small overshoot in the power is tolerated.

Finally, it is observed that the DC-link voltage is kept constant with small error during the whole simulation. The start-up of the motor does not disturb the wind farm in any way, except for the 0.5 % increase in DC-link voltage that is visible in Fig. 5.1 e).

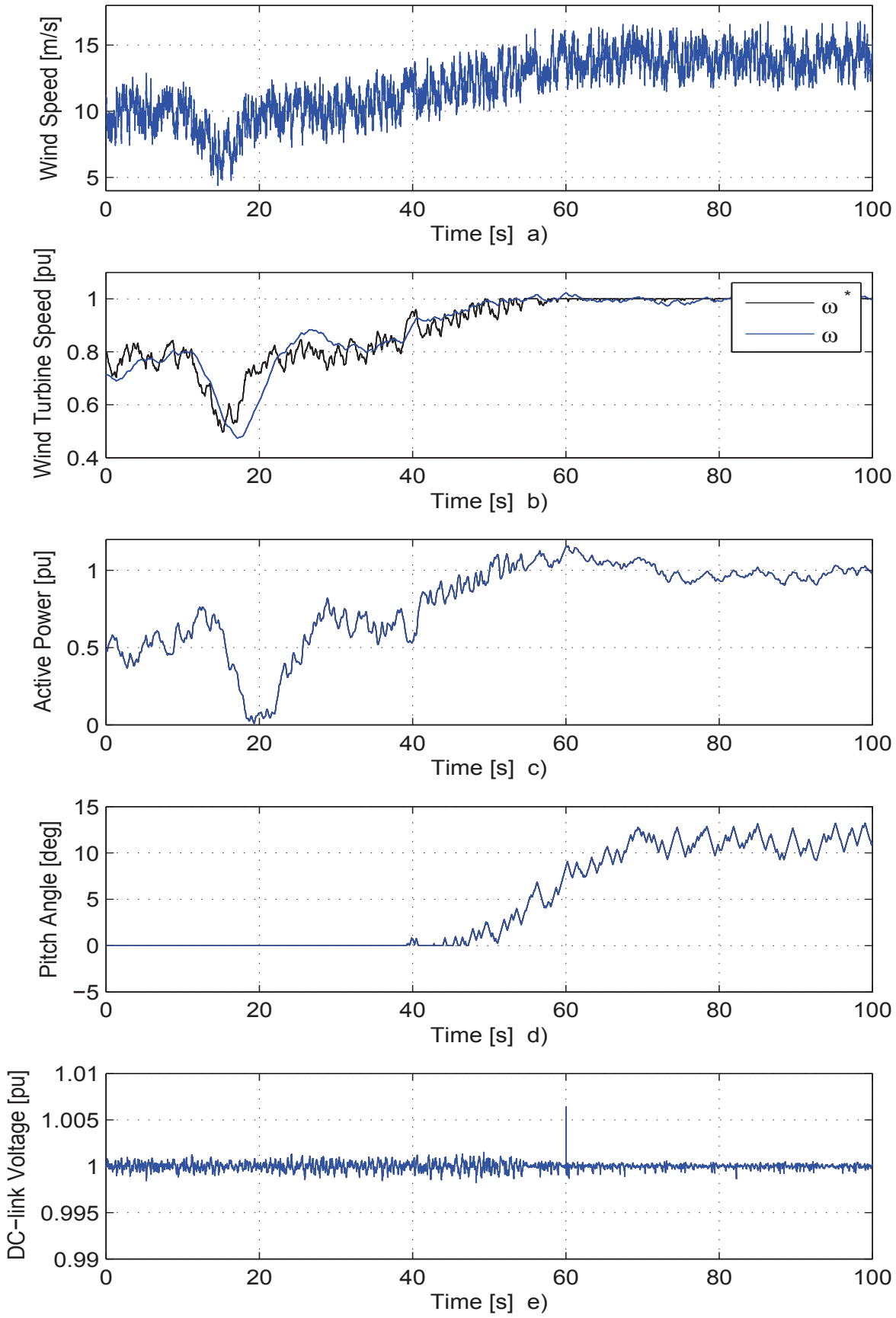

Fig. 5.1: Motor Start and Wind Fluctuations - Generator Side

System Side Parameters

The oil platform is affected by the wind farm and its variable power production. This section shows the platform frequency and voltage along with the active and reactive powers from the wind farm, oil platform and induction motor load. Note that all powers are referred to the oil platform. See section 5.2 for a description of the simulation case. The results are presented in Fig. 5.2.

The active power from the wind farm, gas turbine and induction machines are shown in Fig. 5.2 a). It is observed that the gas turbine governor system is able to compensate for the variable wind power such that the load has close to constant power. There is a sudden change in load power during the motor start at $t = 60$ s, and it is seen that the gas turbine delivers all the required accelerating power. The wind farm is just producing maximum power regardless of the system state.

The reactive power is shown in Fig. 5.2 b). The wind farm has the objective of producing zero reactive power at all times. However, the reactive power Q_{wind} lies around 2 MVAr since the cable capacitance produces reactive power that is larger than the amount consumed by the cable inductance, see (3.13. The reactive power required to start the induction motor is very large, but the gas turbine does not exceed its rated apparent power of 50 MVA since the active power production is only around 15 MW. If the wind power production was lower at this instant, the motor could most likely not be started, since the synchronous generator does not have sufficient rating.

The platform voltage is shown in Fig. 5.2 c). During the period of fluctuating wind it has a ripple with peak-to-peak magnitude $\Delta V < 0.4$ kV. The stationary IEC-requirements in [55] are $+0.83/-1.38$ kV, so the minimum requirements are fulfilled successfully. During the motor start the voltage drops to 12.2 kV, but this is within the transient grid code limits (11.04-16.56 kV) [55]. The voltage drop is caused by the time-delay in the AVR system, since there is a time-constant associated with the excitation system. The field voltage will stay constant for a short duration while the current is increased, leading to a drop in the terminal voltage until the field voltage is increased.

The system frequency is shown in Fig. 5.2 d). The frequency will have steady-state variations according to the droop constant, in addition to fluctuations caused by the wind power changing faster than the gas turbine and governor system can react. The frequency has peak-to-peak values of 59.7-60.9 Hz, but the stationary grid code allows 57-63 Hz [55].

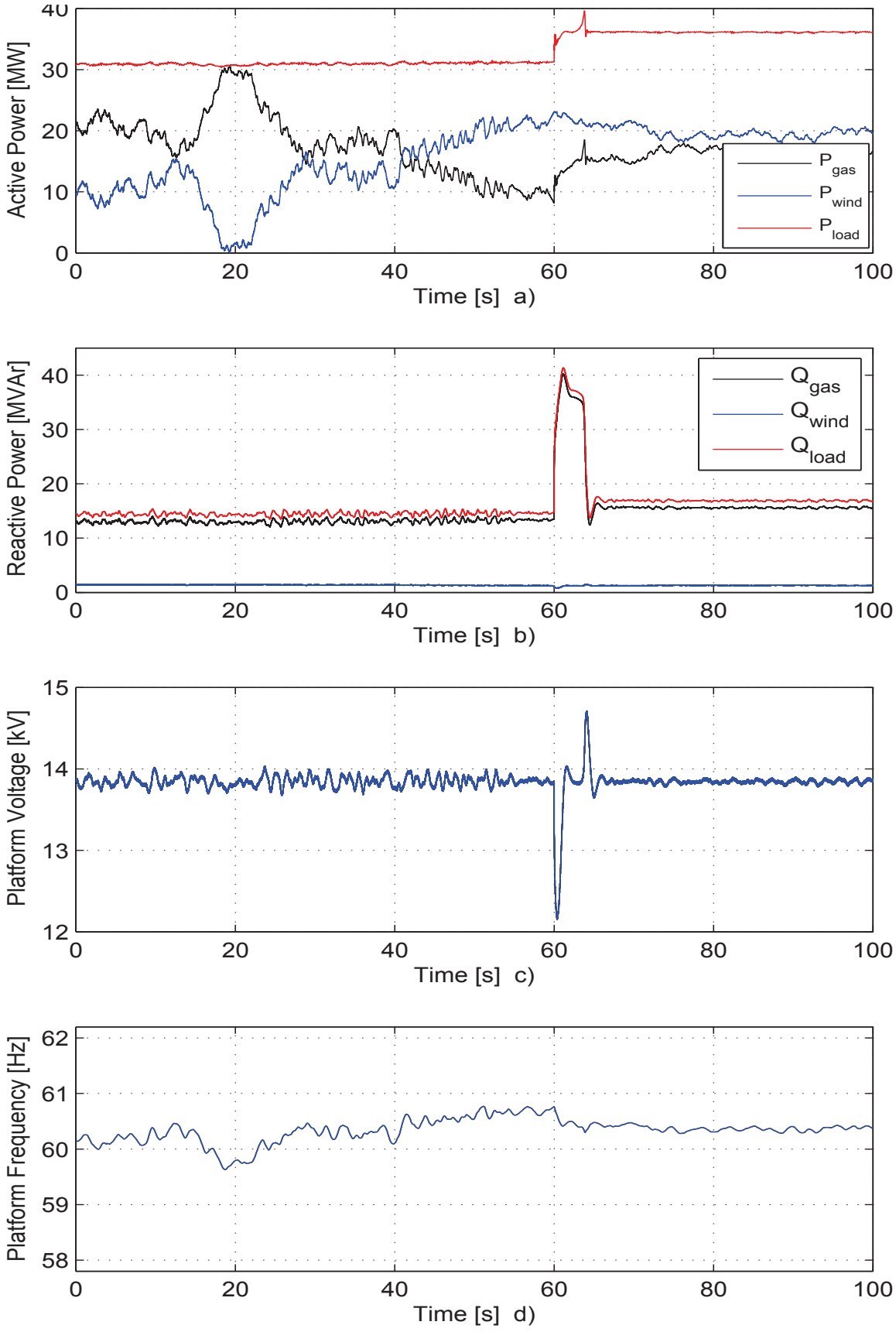

Fig. 5.2: Motor Start and Wind Fluctuations - System Side

5.3 Reactive Support from Wind Farm

The response of the voltage-droop regulator in the System Side Converter is now presented. Refer to section 3.6.2 and Fig. 3.8 for theory and model implementation.

The offset Q_0^* is set to zero, and the gain K_v will be assigned different values, such that the results can be compared.

5.3.1 Large Motor Start

A 5 MW motor is now started at the platform, with 35 MW load initially running. The wind speed is fluctuating, but within high values, such that $16 < P_{wind} < 20$ [MW]. Fig. 5.3 shows the transient for $K_v = \{0, 3, 6, 9, 12\}$. The motor is started at $t = 1$ s. Fig. 5.3 a) shows the platform voltage, and the transient is heavily reduced with the proposed voltage-droop controller in the wind turbines. The oscillations decrease with an increasing K_v, though the effect of increasing from 9 to 12 is minor. Fig. 5.3 b) shows the reactive power from the wind farm, as seen from the platform. The cable produces some reactive power which is included in Q_{wind}. This could be compensated for by choosing $Q_0^* < 0$ in the control implementation presented in section 3.6. It is seen that the shape of the reactive power is equal to the negative voltage offset, indicating that the reactive power controller is performing satisfactory.

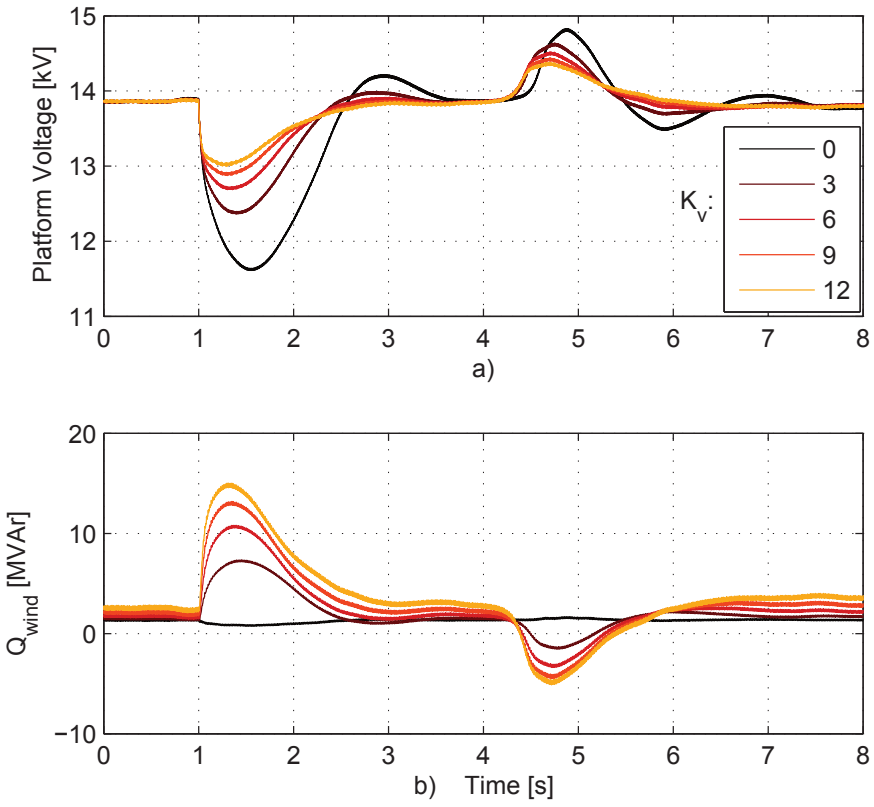

Fig. 5.3: 5 MW Motor Start with variable K_v

5.3.2 Critical Motor Start

The limitations of the voltage-droop controller are now investigated through a simulation case where a 10 MW motor is started. Fig. 5.4 shows the simulation results for $K_v = \{0, 12\}$. The voltage is not able to recover with $K_v = 12$, and the reactive power from the wind farm is not equal to the rated value 20 MVAr. This is mainly because of the Q-limitation in the inverter which was explained in 3.6.2. In addition, the submarine cable decreases its reactive power production and turns into a consumer, as seen in Fig. 5.4 b) when $K_v = 0$. Equation (3.13) explains the fact that the reactive power from a submarine cable is heavily dependent on the voltage. With voltage-droop control implemented, the net reactive power from the wind farm and sea cable is around 6 MVAr, but this is not enough to bring the voltage back to nominal value. With a smaller wind farm or a longer submarine cable, the net reactive power from the wind farm referred to the oil platform would decrease, and may turn negative. This would decrease the chances of voltage recovery, see section 5.6 for a further discussion.

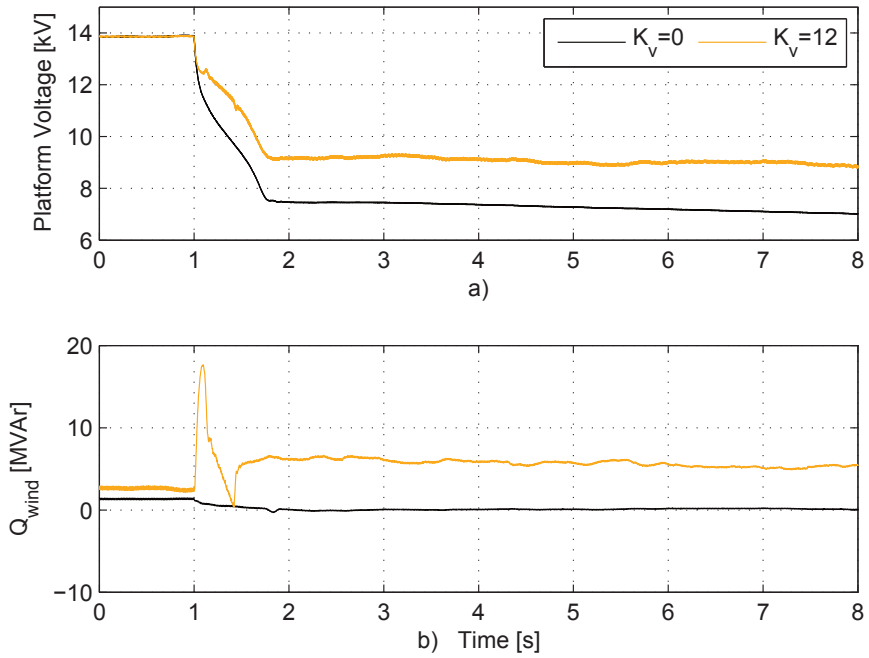

Fig. 5.4: 10 MW Motor Start with variable K_v

The voltage collapse that is present in Fig. 5.4 will lead to a shutdown of the system. Since this is highly undesirable in an oil platform, it is explored further in the following section.

5.4 Voltage Recovery after Disturbances

As explained in section 3.10.2, there are certain events that can provoke a permanent voltage collapse in a platform. A voltage dip will decelerate the directly connected motors to a state where they consume a large amount of reactive power, and this may saturate the synchronous generator such that the AVR cannot recover the voltage. As explained in section 5.3, the reactive power from wind turbine inverters with voltage droop is limited in a low-voltage situation. It is therefore necessary with an over-rated synchronous generator such that the required reactive power can be provided.

Fig. 5.5 shows a 10 MW motor start at $t = 1$ s, with 30 MW initial load, the same case as in section 5.3.2. The behavior is investigated for different ratings of the synchronous generator, namely 50, 60 and 80 MVA. The wind farm does not have voltage-droop implemented except in one case with 50 MVA. The AVR is able to recover the voltage for both 60 and 80 MVA, but a voltage collapse occurs for 50 MVA both with and without V-droop in the wind farm. Fig. 5.5 b) shows the reactive power consumed by the induction motor load. With a rating of 80 MVA, more reactive power can be provided, so that the corresponding voltage dip is small. The 60 MVA case requires longer recovery time, and it seems like the system is on the edge of collapse.

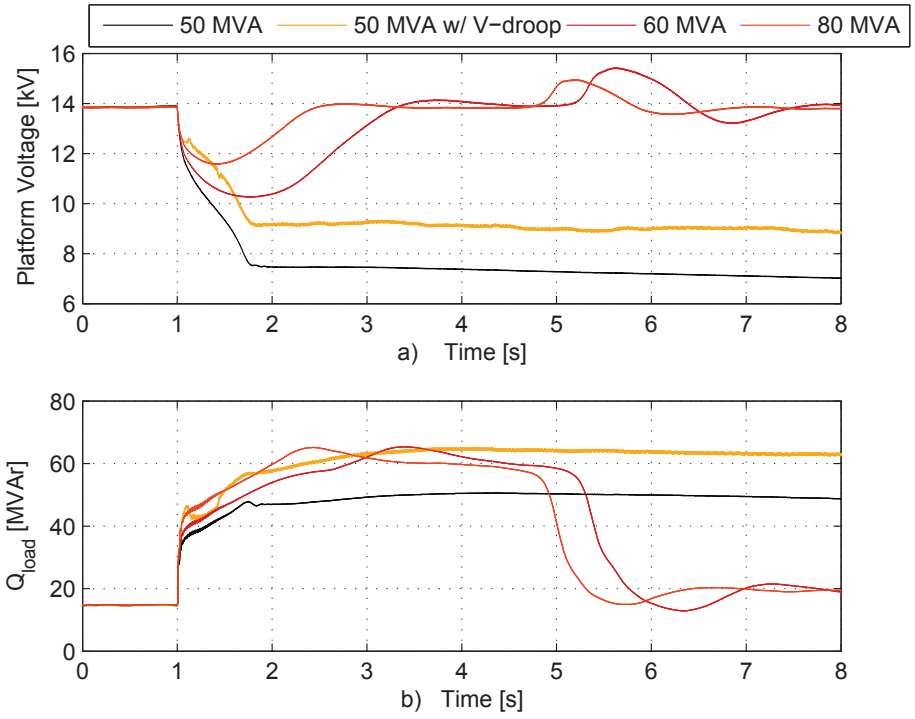

Fig. 5.5: 10 MW Motor Start with variable generator rating

The results show that to increase the rating of the synchronous generator with 10 MVA is more effective than to have 20 MVAr available reactive power in the wind farm. This contradicting fact is caused by the decreased capability of the wind turbine inverters during low voltage conditions, see section 3.6.2. The limitations and suggestions for improvements are discussed in section 5.6.

5.5 Sudden Loss of Wind Power

Certain events can provoke a disconnection of the wind farm. Some components may fail such that the protection system will open a breaker. The cable can be damaged or tore apart by anchors of ships. Even though these cases occur rarely, they have to be considered during the system design process. This section presents simulation results where the cable to the wind farm has suddenly been disconnected. The simulations investigate how the platform recovers from the disturbance. It is followed by a discussion related with how the wind farm control system should be designed to avoid damage on equipment during such events.

Fig. 5.6 a) shows the active power flow in the system. At $t = 2$ s the wind farm is disconnected such that P_{wind} drops to zero. P_{sync} is the power flowing out of the synchronous generator, which is seen to compensate very fast for the loss in wind power. However, this is not the same power that is generated by the gas turbine, represented by P_{gas}. The difference between the two curves represents the withdrawal of rotational energy, which again leads to a frequency drop shown in Fig. 5.6 d). The time-delay in P_{gas} is characterized by the dominant time constant in the gas turbine $T_{fuel} = 0.4$ s. The actual response has a duration in the range of this value. The frequency is seen to stabilize at a new steady-state value after the disturbance, according to the governor setting and increased power output.

Fig. 5.6 c) shows the RMS-voltage on the platform. It increases right after the disconnection because the power output of the generator increases. This is explained in section 3.9. After about 0.4 s, the voltage starts to decrease, and is eventually brought back to the reference value. This is due to the delayed operation of the AVR and excitation system.

The reactive powers are shown in Fig. 5.6 b). Q_{load} oscillates as a result of oscillations in the voltage. The generator reactive power Q_{gen} is quickly adjusted such that it is equal to Q_{load}. Note that reactive is defined to be positive into the load, out of the generator, and from the wind farm.

Apart from the oscillations that occur right after the disconnection, the results are promising with respect to whether the oil platform will ride through this event or not. Oscillations are normal during large disturbances in power systems, and the frequency and voltage are kept safely within the transient grid code limits in appendix G and [55]. The ride-through capabilities are dependent upon how fast the AVR and gas turbine can adjust the reactive and active power, respectively. In a system with slower units, the transient may lead to system shutdown if the voltage or frequency drops below the tolerated limits. Load shedding, where one or several large motors are disconnected right after the loss of wind power can improve the system stability. To sacrifice a few units is a small price to pay if the alternative is to disconnect the whole platform.

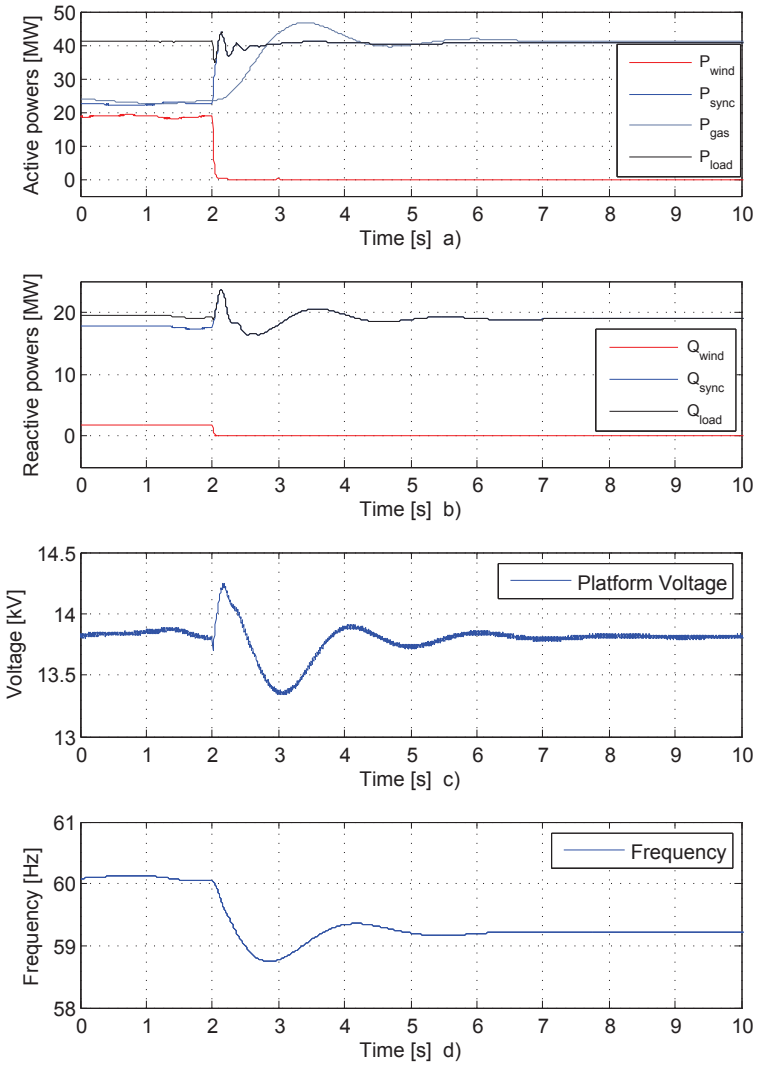

Fig. 5.6: Loss of Wind Power

The wind turbines have to be shut down during a disconnection event, or whenever the wind speed exceeds a limit denoted cut-out speed [30]. The following discussion is included in order to highlight the problems and to discuss some of the available technologies that can safely disconnect a wind turbine. The main challenge during a disconnection is that the turbines are generating power while there is no load to consume it. The pitching mechanism described in section 3.2 will eventually turn the generated power to zero, but the control system has to ensure that the power is dissipated until the blades are fully pitched. This may take in range of 10 seconds. Mechanical brakes are normally installed in the hub of the turbine, and they will limit the rotational speed to some extent. The DC-link in the converter can be equipped with a chopper circuit such that the DC-voltage is kept within safe limits, but the chopper resistor can only consume a limited amount of power. The turbines can have some power dissipating units on the system side, such as a large resistor. However, a resistor that shall consume the rated power of a wind turbine for several seconds requires a large space. As mentioned before, space is a limited resource in offshore environments. However, the problems mentioned in this section are not specific to the layout of System 1, but a general challenge for onshore and offshore wind farms.

5.6 Discussion

The wind farm model has been implemented and tested thoroughly. The control systems are working as intended. The simulations cases have been selected in order to highlight the main challenges that have been discovered. This section discusses the results with respect to the challenges and possible improvements.

The submarine transmission cable is 10 km, and is considered as relatively short. During normal operation it has similar effect to a capacitor bank, since the net reactive power is positive. This is favorable since it can supply some of the reactive power required by the load. However, it has been shown that during voltage dips the reactive power from the cable decreases and may even change direction. A change in direction is negative for the system stability, since the synchronous generator and wind farm inverter need to supply more reactive power in order to recover from the voltage dip. It has been shown in the simulations that both the synchronous generator and wind farm inverter are saturated during a large motor start, meaning that they deliver maximum reactive power. It is assumed that a longer transmission distance between the wind farm and oil platform would increase this negative effect. If the distance exceeds a certain value, the cable will consume more reactive power than the wind farm can deliver, such that the benefit of having reactive power control in the wind farm is dominated by the disadvantage related with the cable. Refer to section 3.7.

If wind power is integrated with an existing oil platform, measures should be taken to ensure that the added components do not increase the risk of voltage collapse or similar events. The type of cable should be chosen with care, in addition to the type of transformer and voltage ratings. It should also be considered to install additional reactive compensation units. One possible system improvement is to increase the rating of the wind turbine inverter, such that it can deliver more reactive power. However, it has been argued in section 3.6.2 that shunt compensation units like the wind turbine inverter have reduced capability during low-voltage transients. To install additional series compensation units is an effective solution, but they are expensive and have problems related with reliability since they are not easily disconnected. To install ordinary capacitor banks in shunt is a cost-efficient choice, but they have also reduced capability in a low-voltage situation. To find the best solution requires economical considerations, and will not be treated further. It is remarked that compensation units most likely have to be placed in the wind farm since the strict space and weight requirements on a platform make it hard to place additional equipment here.

It has been shown that the wind farm inverters can provide dynamic reactive power control in order to support the voltage control in the oil platform. It is also possible to implement frequency control in the wind turbines. The control structure can be similar to the governor droop control in the gas turbine. The wind turbines should increase or decrease their output according to the deviation between the nominal and actual frequency. Depending on how the control is implemented, the Maximum Power Point Tracking (MPPT) ability of the turbines will be weakened, since they no longer have complete control of the power and hence the torque. The MPPT and frequency support control systems both wants to decide the power output of the turbine, so a weighing between the two objectives has to be developed in order to avoid control conflict. In contrast to a generating unit that has control over its power generation, the wind turbine can only provide frequency support for a limited amount of time. The surplus or deficit power will lead to an unwanted accel-

eration or deceleration of the turbine, and the speed has to be kept within its design limits. The simulation results in this chapter show that the frequency transients in the different events do not exceed the grid code limits in [55]. It is therefore considered as redundant to implement frequency support for System 1. The possibility should however be evaluated for similar systems, especially if the gas turbine and governor system has larger delays associated with it. It is also an interesting opportunity in onshore wind power, where the grid code is far more strict. Some countries even demand that every power plant above a certain rating should contribute to primary and secondary frequency control routines.

The gas turbine model used in the simulations performs satisfactory, but a slower unit can lead to undesired frequency oscillations. It would be beneficial to have a short-term estimation of the wind power production, such that the gas turbine can start to increase or decrease its production prior to a wind speed change. If several wind speed measurement units are placed in the area nearby the turbines, it is possible to forecast the wind power. Frequency oscillations in the system can then be reduced if the measurements are used in the correct manner. The information can also be utilized to increase the performance of the pitch and speed control systems in the turbines. The measurements can tell the control system to increase the pitch angle right before a speed increase, and the generator can start to adjust the speed toward the new reference according to the maximum-power-point tracking objective. To examine these possibilities is recommended as further work.

Chapter 6

Simulations on System 2

This chapter contains simulation on System 2: Integration wind power with Troll A. The purpose behind the simulations is to first check the performance of the proposed control system from chapter 4. Secondly, overall system simulations are carried out that can indicate if System 2 represent a feasible configuration that should be performed further research on.

Section 6.1 gives the most important numerical data used in the simulations. The following sections 6.2, 6.3 and 6.4 demonstrates the response of the control system in each converter individually. The complete system is then simulated in section 6.5. The wind profile described in appendix F is used. In addition, two set-point changes in the SM speed ω is invoked during the simulation. Section 6.6 presents a simulation where the whole wind farm power is suddenly lost, while the chapter is concluded with a discussion in section 6.7

6.1 Numerical Parameters

This section gives the most important parameters in System 2. Ratings of voltages, frequencies and powers are obtained from [49], while impedances and inertias are adjusted in simulations such that proper operation is achieved. Screenshots of the simulation model are given in appendix H. The data for the wind farm is equal to System 1, and can be found in Table 5.1. Data for the synchronous motor and MSC is found in Table 6.1 and appendix F, while Table 6.2 gives the data for the OSC and Kollsnes AC grid. The DC-network parameters are stated in section 4.5, and the WSC data is found in Table 6.3.

Parameter	**Value**
Rating of Motor	45 MW
Terminal Voltage	40.6 - 58 kV
Frequency	42-63 Hz
Rated Frequency	60 Hz
Switching Frequency	2 kHz
Stator Inductances (L_d and L_q)	1.25 pu
Inertia	3 s

Table 6.1: Synchronous Motor and MSC data

Parameter	Value
Switching Frequency	2 kHz
Maximum Load	45 MW
Converter AC voltage	58 kV
Transformer ratio	(58:132) kV
Kollsnes Grid Inductance	0.0 H
Transformer Leakage Inductance	0.03569 mH =0.15 pu
Transformer Resistance	0.74755 Ω =0.01 pu

Table 6.2: Onshore Side Converter Data

Parameter	Value
Switching Frequency	2 kHz
Power Rating	20 MW
Nominal AC-frequency	60 Hz
Nominal AC-voltage	58 kV
Transformer ratio	(58:22) kV
Transformer Leakage Inductance	0.03569 mH =0.08 pu
Transformer Resistance	0.74755 Ω =0.0044 pu
Generator Inertia	3s

Table 6.3: Wind Side Converter Data

6.2 Test of MSC Control System

The DC-side of the MSC at Troll A will now be connected to a constant DC-source in order to test the proposed control system of the synchronous motor. Recall that the control objectives are to adjust the rotational speed ω according to an external reference ω^*. In addition, the stator flux is kept at its rated value and the total stator current is minimized in order to reduce losses.

To test the controller through two changes in operation points is proposed. The system is initially operating with $\omega = 1$ pu. At $t = 4$ s, ω^* is ramped down to 0.7 pu according to the rate limiter in Fig. 4.2. At $t = 28$ s, the speed ramped back to 1 pu.

Fig. 6.1 shows the results of this simulation. Both ω, i_d and i_q are regulated toward their references successfully. The maximum electrical torque is sufficient to provide the required acceleration such that the deviation between ω and ω^* is zero. This would not be the case without the rate limiter of ω^* in Fig. 4.2, since the inertia of the motor limits how fast the motor can be accelerated.

The field current controller is not so effective in eliminating steady-state error, as seen in Fig. 6.1 d). This is because of the large time-constants present in its transfer function from Fig. 4.3. This will lead to a small deviation between the stator flux ψ_s and the rated flux $\psi_{s,rated}$. This is illustrated in Fig. 6.1 e), where the motor terminal voltage v_c is compared to the voltage that should have been applied to yield nominal flux according to (4.9). A deviation occurs during the transients associated with the periods of acceleration, but the error is negligible in steady-state.

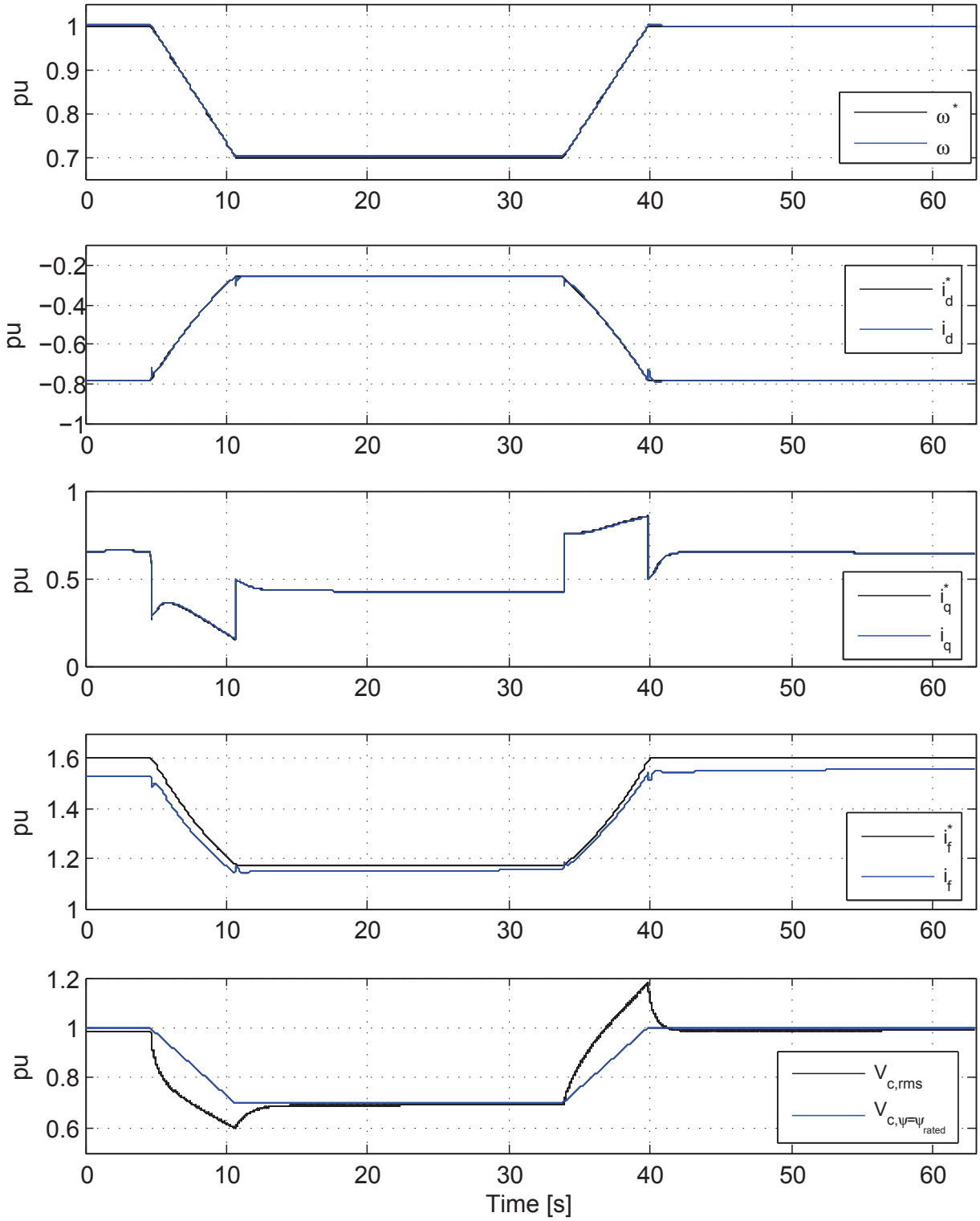

Fig. 6.1: Simulation of SM connected to constant DC-link voltage

6.3 Test of OSC Control System

The control system in the OSC will now be tested according to the objectives from section 4.6 and the tuning performed in appendix D. The objectives are to control the DC-voltage at Troll A, and the reactive power flow from the OSC to the onshore grid in Kollsnes. Voltage control is achieved without any telecommunication, so the cable voltage drop is estimated based on the cable resistance and current, see section 4.6.

Fig. 6.2 a) shows the reactive power that is injected into the grid at Kollsnes. At $t = 0.1$ s the reference reactive power Q^* is increased from 0 to 0.5. The response is fast, contains no overshoot, and settles within 0.25 s. Note that the reactive power is affected by the DC-voltage control at $t = 0.3$ s and $t = 0.5$ s. It is not possible to completely remove the cross-coupling between the controllers of V_{DC} and Q, meaning that fast dynamics in one of the controllers will affect the response in the other. The cross-coupling effects shown in the simulations are so small that they are considered acceptable.

Fig. 6.2 b) shows the response of the DC-voltage controller. V_T is initially controlled to 120 kV, and the reference is set to 100 kV at $t = 0.3$ s. At $t = 0.5$ s, the reference is reset to 120 kV. The response is very fast, with the transient at $t = 0.3$ shown in detail in Fig. 6.2 c). A small overshoot is present, and the settling time lies in the range of 20 ms. Oscillations occur when $V_T^* = 100$ kV because the PI-regulator is tuned with base in a operating point equivalent to $V_T = 120$ kV, and will not work properly at $V_T = 100$ kV. However, the overshoot and oscillations do not represent any problem in the performance of the controller, and the results are considered satisfactory. It is remarked that V_T responds immediately after the change in V_K, indicating that the duration and magnitude of the transient cable inductance voltage $V_L = L\frac{di}{dt}$ is negligible.

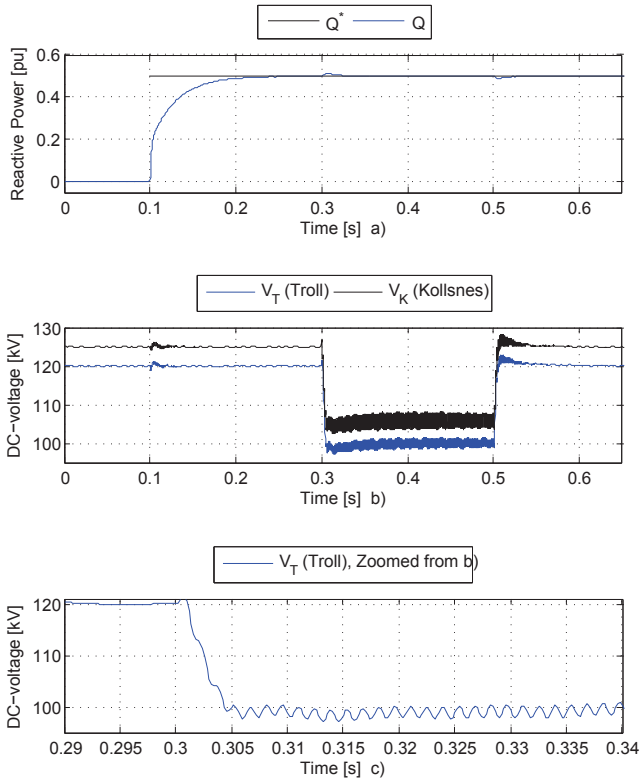

Fig. 6.2: Testing of OSC Control System

6.4 Test of WSC Control System

In the following section, the control system in the WSC is tuned and tested in order to validate the behavior that is expected according to section 4.7. The control objective is to control the AC-voltage on the 22 kV side of the transformer in Fig. 4.9. The response of the controller should be as fast as possible, but the integration time constant must be set to a value larger than the dominant electrical time constant in order to avoid oscillations. It is assumed that this time constant is smaller than 0.04 s, meaning the PI integration time constant T_i can be set equal to 0.4 s. The gain K_p is adjusted through a series of simulations in order to obtain a fast response without overshoot. The following control parameters are found to be adequate:

$$\begin{aligned} T_i &= 0.04 \\ K_p &= 0.2 \end{aligned} \tag{6.1}$$

The response of the controller is tested in a simulation where the voltage set point V_p^* is initially 1 pu, and is changed with a step to 0.5 pu at $t = 0.05$ s. The results are shown in Fig. 6.3. Fig 6.3 a) shows the phase voltages, while Fig. 6.3 b) shows the estimated RMS-voltage along with the control system reference. The response is observed as smooth and with no overshoot. The settling time is 0.15 s. The control system performance is considered as satisfactory.

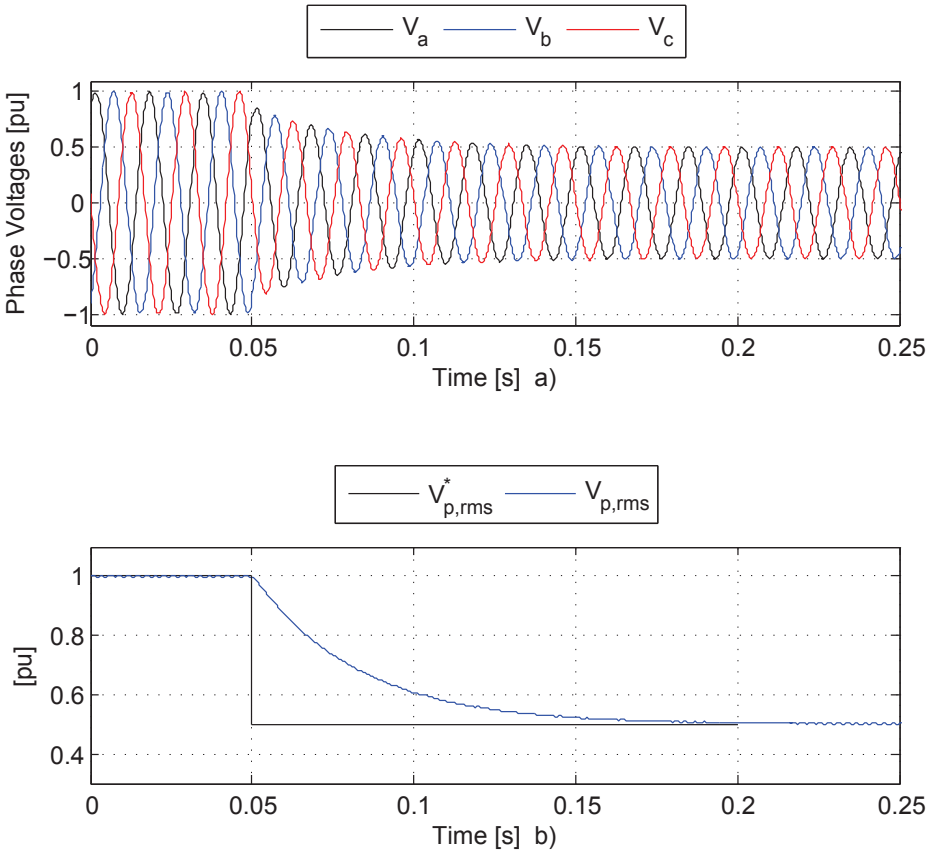

Fig. 6.3: Testing of WSC Control System

6.5 Normal System Operation

The complete system is now simulated together, in order to observe the behavior under normal conditions. To gain a realistic scenario, the wind speed profile from appendix F is used, such that the active power from the wind farm will be equal to Fig. 5.1 c). The DC-voltage at Troll A is controlled to 120 kV, while the AC-voltage at the WFC is controlled to 58 kV. Speed set-point changes in the SM at Troll A are invoked at $t = 70$ s and $t = 85$ s. The reactive power in the OSC is controlled to zero. Fig. 6.4 shows the result of the simulation.

Fig. 6.4 a) shows the speed of the SM ω along with its reference ω^*. Similar to the results in section 6.2, there is no deviation between ω and ω^*. The operation of the SM is therefore not affected by changes in the wind power during normal operation. This is an important result, and a necessary requirement according to section 4.2.

Fig. 6.4 b) shows the active power flow in the DC-network. P_K and P_T are the powers leaving Kollsnes and entering Troll A, respectively. They are equal besides the losses in the cable, and these losses are seen to increase with increasing power. P_{wind} is the power entering Troll A from the wind farm, and it evidently fluctuates in the same way as Fig. 5.1 c). Finally, P_{SM} is the power entering the MSC and consumed in the motor. It is constant except for the periods of acceleration and deceleration, and this implies that the wind farm does not affect the gas compressor in a negative manner.

Fig. 6.4 c) shows the DC-voltages at Kollsnes and Troll, denoted V_K and V_T respectively. The control objective is to have $V_T = 120$ kV, and this is achieved through the whole simulation, except for small overshoots when the power to the SM changes. Some ripple must be tolerated since the cable capacitance is small, and is therefore easily discharged. The voltage at Kollsnes V_K varies in order to compensate for the resistive voltage drop in the cables.

Finally, Fig. 6.4 d) shows the AC RMS-voltage at the WSC. It is controlled to 58 kV according to the objectives. A small deviation is observed at the same instants as V_T has deviations. The control system in the VSC assumes a constant DC-voltage, and the PI-regulator that controls the AC-voltage is not able to compensate for fast changes in the DC-voltage. The steady-state ripple of ± 0.15 kV is caused by the analog RMS-calculations in PSCAD.

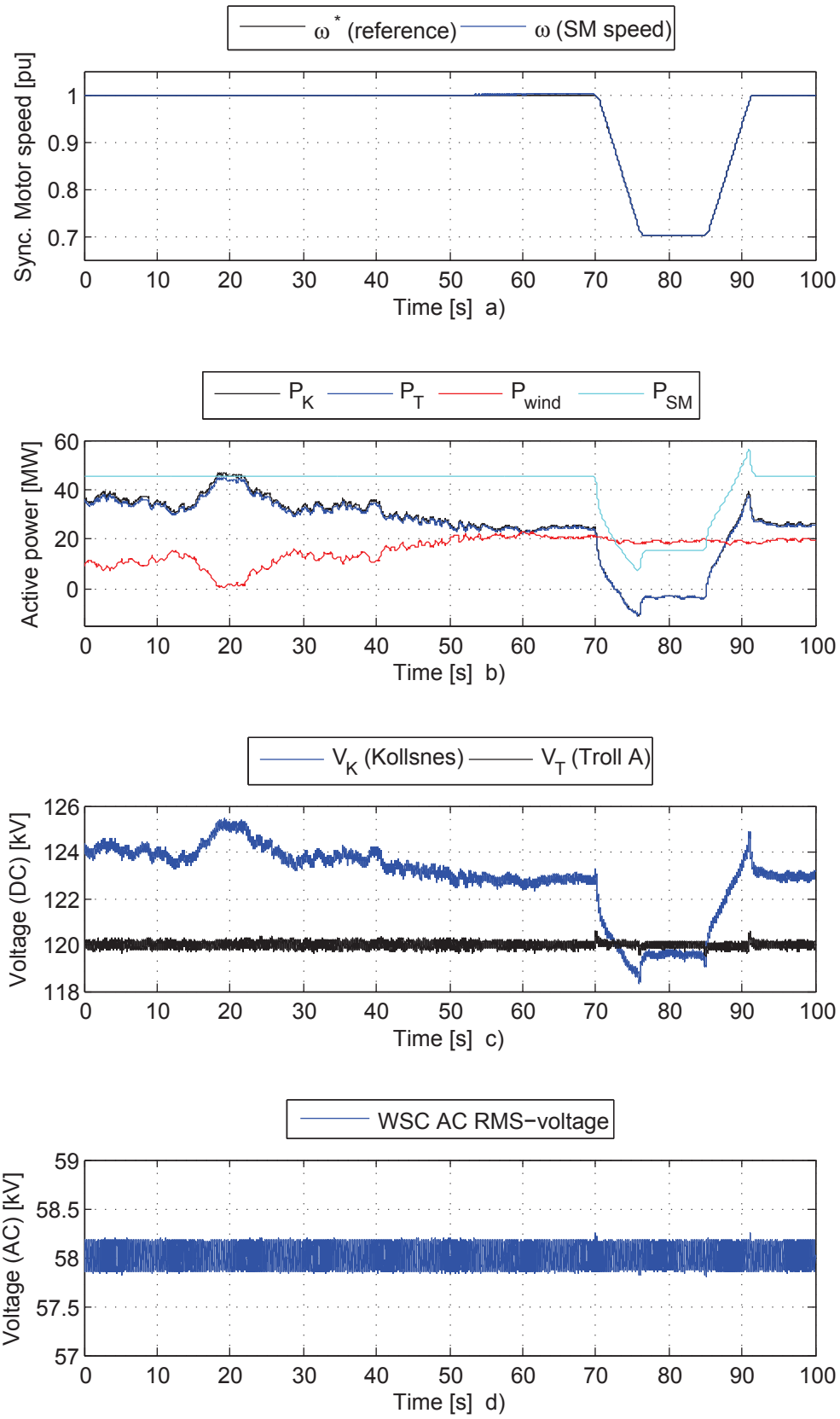

Fig. 6.4: Simulation of System 2 with Wind Fluctuations

6.6 Sudden Loss of Wind Power

The operation of the wind farm can be disturbed to such an extent that it is necessary to disconnect it from the grid. See section 5.5 for causes that may lead to disconnection. This section present results from a simulation where the wind farm is disconnected with a three-phase circuit breaker. The sudden drop in active power creates a challenge for the rest of the system. The DC-voltage is expected to drop rapidly since the MSC will draw some power from the stored energy in the DC-cable until the DC-voltage control system is able to restore the voltage.

Fig. 6.5 a) shows the speed of the SM along with the reference, and it is not affected by the loss of wind power. This result is important in the process of determining whether the wind farm can reduce the availability of the MSC, as loss of all wind power is one of the most critical scenarios that can occur in the wind farm.

Fig. 6.5 b) shows the active power flow in the system, with the same notation as in Fig. 6.4 b). It takes ≈ 0.0025 s before the circuit breaker has completely blocked the power flow, and additional 0.003 s before the OSC has increased the power P_K with an amount corresponding to the lost wind power. The power P_{SM} that is transferred through the MSC has a small oscillation during this period, but the duration and amplitude of the oscillation is so small that the motor speed is unaffected. The combined inertia of the synchronous motor and the gas compressor corresponds to a stored amount of energy equal to 3 seconds of 45 MW. The duration of the disturbance introduced by the loss of wind power lies in the range of 20 ms, so its influence on the speed of the synchronous motor will be negligible.

Fig. 6.5 c) shows the DC-voltages at Kollnes and Troll, denoted V_K and V_T, respectively. Both voltages drop suddenly at the instant of wind power loss, but the voltage is restored after about 20 ms. Some low-amplitude oscillations are present since the DC-voltage has dropped outside the nominal working point, but they die out after approximately 50 ms. The same oscillations are visible in the active powers P_K and P_T, they originate from the interaction between the control system and the cable RLC-network.

Fig. 6.5 shows the AC RMS voltage on the terminals of the WSC. It is seen that the WSC is able to restore the voltage after 0.02 s, even though it has no current flowing through after the wind power is lost. The simulation verifies one of the important abilities of the VSC, namely to operate a grid that is running at no-load. Note that the oscillations in the RMS-voltage arise from the analog RMS-calculation in PSCAD.

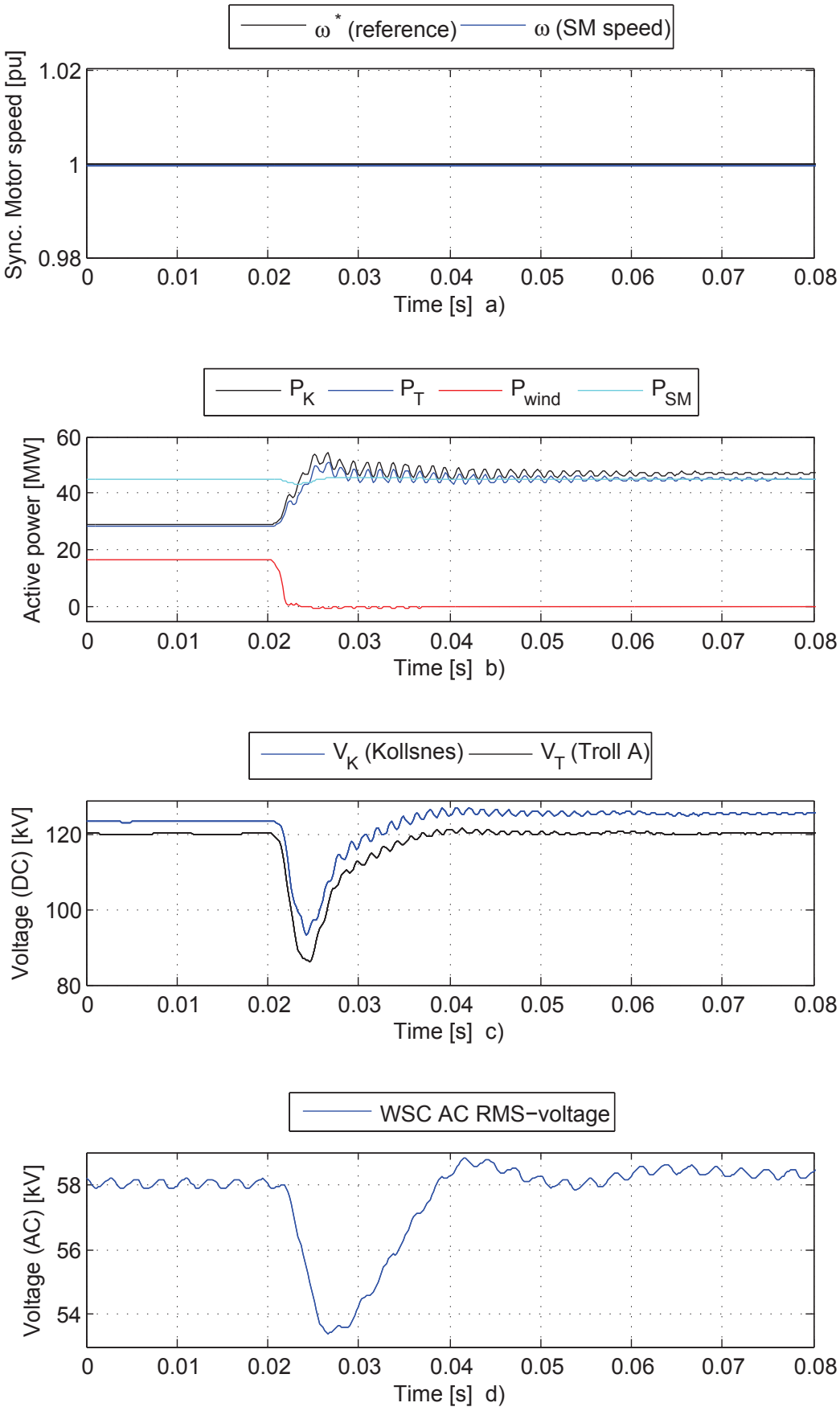

Fig. 6.5: Simulation of System 2 with Loss of Wind Power

6.7 Discussion

The control system that has been implemented for the Synchronous Motor is controlling the speed as expected. However, improvements could have been done to the other control functionalities. The objectives of having rated flux and minimized stator current should be used, but the implementation contains no feedback to check whether the objectives actually are satisfied. The objectives are not met if the simplifications from section 4.3.1 does not apply, or if measurements are erroneous. Inaccurate parameter estimations will also affect the control system performance. It is remarked that the flux in a machine cannot be measured, so an estimation is required in any case. However, it has been confirmed in the simulations that both rated flux and minimized current is achieved. The purpose of modeling the synchronous motor is not to optimize and yield a robust control system, but to see how it is affected by the added wind power. The details regarding measurements and control of flux is therefore considered as out of scope for the thesis. The reference [54] gives an excellent derivation and explanation on control of a field excited synchronous motor.

The average VSC model has been used for all simulations related with System 2. It is important to discuss the validity of its use. The power flow through the converter in the average model is smooth and is not affected by the switching operation, since the switching frequency is assumed to be infinite. In a real converter, the power entering the DC-link will follow the switching pattern such that a sudden power change occurs at every turn-on or turn-off of one converter leg. If the DC-link energy storage, mainly represented by the cable capacitance, is too small, the switching operation will introduce significant ripple in the DC-voltage. The DC energy storage can be quantified by the equivalent capacitance time constant $C_{pu} = 1.568$ ms, see appendix D. This time constant represents the time it takes to charge the capacitance from zero to rated voltage with nominal power applied. The actual switching frequency of the converter is 2 kHz, meaning that there in average will be $2000 \cdot 0.001568 = 3.14$ switching actions per leg during the time period equal to C_{pu}. This number should be significantly larger. The close to instantaneous injection or removal of power during a turn-on or turn-off is likely to affect the DC-link voltage in a more significant manner than the average model simulations show. The control system can not compensate for the high-frequent oscillations in DC-voltage. It has been attempted to perform simulations with a detailed VSC-model, but oscillations in the DC-voltage have lead to instability. This raises the question whether additional capacitance is used to provide more energy storage. A request to [49] have confirmed this suspicion, but information regarding the configuration and parameter values are not available.

There are some challenges related with System 2 that the simulations do not cover. The technology related with breaking of DC-currents are not yet mature for a high-voltage system with this rating. To ensure relay selectivity and secure operation of a multi-terminal VSC system is considered as a major challenge. To include simulations with faults on the DC-side followed by breaker actions should be included in further research.

A final remark can be stated regarding System 2. The configuration represents a huge leap in technology, and a large number of challenges must be addressed before the system can be realized. It is likely that offshore wind power can be integrated with oil platforms in simpler manners. However, the focus of this thesis lies in the opportunity of VSCs, and System 2 is interesting in this respect. In addition, many of the emphasized conclusions can be transferred to other and simpler topologies.

Conclusions

Two offshore power systems have been modeled in order to investigate whether they represent feasible ways to interconnect offshore wind power with oil platforms. This section contains the most important conclusions that have been drawn.

System 1 consists of an offshore wind farm and an oil platform connected together in islanded operation. It is concluded that wind turbines equipped with Voltage Source Converters have promising features in islanded power systems. The opportunity of dynamic voltage support is a valuable supplement to the oil platform voltage control system. Frequency support in the wind farm can be implemented as well, but this is found to be redundant in the actual system. The transmission system between the wind farm and oil platform, mainly consisting of transformers and a submarine cable, shows undesirable behavior during voltage dips. Additional reactive compensation units may have to be installed to ensure that the wind farm does not increase the risk of system shutdown during disturbances. It is questioned whether the gas turbine and AVR models that are used represent realistic behavior. They seem to react very fast to disturbances, such that frequency and voltage deviations are kept safely within the grid code limits. Systems with slower units may not satisfy the requirement given by the grid code.

System 2 consists of a VSC-HVDC connection between Kollsnes and the platform Troll A. It is proposed to integrate wind power on the DC-side of the Troll A VSC-terminal. This requires multi-terminal VSC, which is not yet commercially available. However, it is concluded that the control systems developed are able to maintain proper operation the system during the simulation cases that are investigated. The DC-voltage control system on Kollsnes is able to estimate and control the voltage at Troll successfully. The losses in the HVDC cable are high since the system is operated at a lower voltage than the cable is designed for. The proposed wind power integration will reduce the losses significantly.

The results obtained indicate technical feasibility for both systems. However, the thesis must only be viewed as a preliminary study, and more detailed investigations should succeed it. The results are heavily dependent upon the simulation parameters, and this is quantified in a sensitivity analysis on System 1 performed in the conference paper in appendix J. The model data has to be refined in order to yield more accurate models. In addition, new simulation cases should be defined, in particular short circuit analysis and other transients that require a more detailed model of the VSCs.

System 1 and 2 show only two possible ways of integrating wind power with oil and gas platforms. Some general conclusions can be drawn that is independent of the system layout. Offshore power systems are far weaker than a typical onshore grid. This introduces requirements to the wind farm technology, since it has to be an active component in the grid in order to avoid decreased stability properties. Regardless of AC- or DC-connection, islanded or grid-connected, the role of power electronics and VSC seem significant in order to have stable operation conditions in the offshore environments. They bring more controllability and flexibility into the respective systems, which makes the integrations more favorable.

Further Work

This thesis must be viewed as a preliminary study that only investigates some of the electrical aspects regarding interconnection of offshore wind and oil platforms. The following section contains some topics that it is encouraged to perform further research on.

First of all, new topologies have to be defined. A comparative study is necessary in order to identify which type of connection that is most feasible. However, this choice is dependent on the specific platform that should be electrified. Other configurations that should be considered are for example an AC-connection to the onshore grid. In addition, it is possible to have an offshore AC-grid, and send the power to shore through point-to-point VSC-HVDC. Norwegian research communities have devoted large resources to these topics.

It is encouraged to perform a more detailed data collection process. The results obtained are only relevant for the particular set of parameters, so the parameter and model uncertainties must be taken into account when drawing conclusions. The sensitivity analysis approach is valuable in this respect, and it is suggested to perform a broader and more thorough sensitivity study related with offshore power systems.

It is also suggested to perform a broad range of simulations with the detailed VSC model in order to explore simulation cases with faster dynamics than the average model can examine. In addition, laboratory experiments should verify and support the conclusions obtained from detailed VSC model simulations.

Bibliography

[1] Sustainable development in the european union. Eurostat- the European Comission.

[2] Norwegian oil production through 35 years. Accessed on www.norway.org.

[3] Norwegian Petroleum Directorate. The petroleum resources on the norwegian continental shelf, 2010. Accessed on www.npd.no.

[4] P. de Almeida and P.D. Silva. The peak of oil production–Timings and market recognition. *Energy Policy*, 37(4):1267–1276, 2009.

[5] Oljeindustriens Landsforening. Alternativ kraft til norsk sokkel, 2007. Accessed on www.olf.no.

[6] TF Nestli, L. Stendius, MJ Johansson, A. Abrahamsson, and PC Kjaer. Powering troll with new technology. *ABB REVIEW*, (2):15–19, 2003.

[7] Zero Emission Resource Organization (Zero). Et krafttak fra land - hvordan kraft fra land kan redusere utslippene fra norsk sokkel, 2007. Accessed on www.zero.no/publikasjoner/.

[8] Norwegian Ministry of the Environment. Storting proposition no. 34 (2006-2007), accessed on http://regjeringen.no.

[9] Norwegian Water Resources and Energy Directorate. http://nve.no/no/Konsesjoner/Konsesjonssaker/Vindkraft/.

[10] L. Xu, L. Yao, and C. Sasse. Grid integration of large DFIG-based wind farms using VSC transmission. *IEEE Transactions on Power Systems*, 22(3):976–984, 2007.

[11] W.He, G.Jacobsen, T.Anderson, F.Olsen, T.Hanson, M.Korpaas, T.Toftevaag, J.Eek, K.Uhlen, and E.Johansson. The potential of integrating wind power with offshore oil and gas platforms. *Wind Engineering, 2/2010*, 2010.

[12] HU Dong, SHI Gang, CAI Xu, and W. Jian-feng. Impact of wind power generator on stability of offshore oil platform power systems [j]. *Power System Technology*, 9, 2009.

[13] GS Stavrakakis and GN Kariniotakis. A general simulation algorithm for the accurate assessment of isolated diesel-wind turbines systems interaction. part i. a general multimachine power system model. *IEEE Transactions on Energy Conversion*, 10(3):577–583, 1995.

[14] GN Kariniotakis and GS Stavrakakis. A general simulation algorithm for the accurate assessment of isolated diesel-wind turbines systems interaction. part ii: Implementation of the algorithm and case-studies with induction generators. *IEEE Transactions on Energy Conversion*, 10(3):584–590, 1995.

[15] Q. Jiageng, L. Zongxiang, and M. Yong. Research on isolated diesel-wind power system equipped with doubly fed induction generator. In *The 8th IEE International Conference on AC and DC Power Transmission, 2006. ACDC 2006.*, pages 246–250. IET, 2006.

[16] AMO Haruni, A. Gargoom, ME Haque, and M. Negnevitsky. Dynamic operation and control of a hybrid wind-diesel stand alone power systems. In *Twenty-Fifth Annual IEEE Applied Power Electronics Conference and Exposition (APEC), 2010*, pages 162–169. IEEE, 2010.

[17] P. Mahat, Z. Chen, and B. Bak-Jensen. Gas turbine control for islanding operation of distribution systems. 2009.

[18] Atle Rygg Aardal. Modelling and simulation of an offshore wind farm connected to an oil platform as an islanded system. Technical report, Norwegian University of Science and Technology, 2010.

[19] D.O. Neacsu. Space vector modulation–an introduction. In *Proceedings of The 27th Annual Conference of the IEEE Industrial Electronics Society, IECON*, volume 1, pages 1583–1592, 2001.

[20] Tore Undeland, Ned Mohan, and William Robbins. *Power Electronics - Converters, Applications and Design*. Wiley, 2003.

[21] K. Eriksson. Hvdc light and development of voltage source converters. In *IEEE T&D*, 2002.

[22] Siemens. Hvdc plus - technology, benefits, applications. accessed on: http://www.siemens.com.

[23] B. Gemmell, J. Dorn, D. Retzmann, and D. Soerangr. Prospects of multilevel vsc technologies for power transmission. In *Transmission and Distribution Conference and Exposition, 2008. IEEE/PES*, pages 1–16. IEEE, 2008.

[24] Ned Mohan. *Anvanced Electric Drives*. Mnpere, 2001.

[25] Jan Machowski, Janusz W. Bialek, and James R. Bumby. *Power System Stability - Stability and Control*. Wiley, 2008.

[26] Temesgen Haileselassie, Tore Undeland, and Marta Molinas. Multi-terminal vsc-hvdc system for integration of offshore wind farms and green electrification of platforms in the north sea. *Nordic Workshop on Power and Industrial Electronics(NORPIE)*, 2008.

[27] Cuiqing Du. *The control of VSC-HVDC and its use for large industrial power systems*. PhD thesis, Chalmers University of Technology, 2003.

[28] V. Blasko and V. Kaura. A new mathematical model and control of a three-phase AC-DC voltage source converter. *IEEE Transactions on Power Electronics*, 12(1):116–123, 1997.

[29] ABB. XLPE Submarine Cable Systems - User's Guide.

[30] J.F.Manwell, J.G.McGowan, and A.L.Rogers. *Wind Energy Explained*. IEEE Series on Power Engineering, 2002.

[31] B. Liu, X. Peng, and T. Undeland. Centralized power control strategy of offshore wind farm with permanent magnetic generators. In *IEEE 6th International Power Electronics and Motion Control Conference, 2009. IPEMC'09.*, pages 1075–1079. IEEE, 2009.

[32] J. Zhang, M. Cheng, Z. Chen, and X. Fu. Pitch angle control for variable speed wind turbines. In *Third International Conference on Electric Utility Deregulation and Restructuring and Power Technologies, 2008. DRPT 2008.*, pages 2691–2696. IEEE, 2008.

[33] JG Slootweg, SWH De Haan, H. Polinder, and WL Kling. General model for representing variable speed wind turbines in power system dynamics simulations. *IEEE Transactions on Power Systems*, 18(1):144–151, 2003.

[34] J. B. Ekanayake, L. Holdsworth, X. G. Wu, and N. Jenkins. Dynamic modeling of doubly fed induction generator wind turbines. *IEEE Transactions on Power Systems*, 18(2):803–809, 2003.

[35] J.T.G Pierik, J.Morren, E.J.Wiggelinkhuizen, S.W.H.de Haan, T.G.van Engelen, and J.Bozelie. Electrical and control aspects of offshore wind farms ii. Technical report, Delft University of Technology, 2004.

[36] V. Akhmatov, A. H. Nielsen, J. K. Pedersen, and O. Nymann. Variable-speed wind turbines with multi-pole synchronous permanent magnet generators. part i: Modelling in dynamic simulation tools. *Wind Engineering*, 27(6):531–548, 2003.

[37] M. Chinchilla, S. Arnaltes, and J. C. Burgos. Control of permanent-magnet generators applied to variable-speed wind-energy systems connected to the grid. *IEEE Transactions on Energy Conversion*, 21(1):130–135, 2006.

[38] M. Yin, G. Li, M. Zhou, and C. Zhao. Modeling of the wind turbine with a permanent magnet synchronous generator for integration. In *IEEE Power Engineering Society General Meeting, 2007.*, pages 1–6. IEEE.

[39] Maria Oana Mora. Sensorless vector control of pmsg for wind turbine applications. Master's thesis, Aalborg University, 2009.

[40] J. Liu, H. Nian, J. Li, and R. Zeng. Sensorless control of pmsg for wind turbines based on the on-line parameter identification, 2009.

[41] Chandra Bajracharya. Control of vsc-hvdc for wind power. Master's thesis, Norwegian University of Science and Technology, 2008.

[42] Temesgen Haileselassie. Control of multiterminal vsc-hvdc (MTDC) systems. Master's thesis, Norwegian University of Science and Technology, 2008.

[43] F. Katiraei and MR Iravani. Power management strategies for a microgrid with multiple distributed generation units. *IEEE Transactions on Power Systems*, 21(4):1821–1831, 2006.

[44] S.K. Yee, J.V. Milanovic, and F.M. Hughes. Overview and comparative analysis of gas turbine models for system stability studies. *IEEE Transactions on Power Systems*, 23(1):108–118, 2008.

[45] J. Smith and M. Chen. *Three-Phase Electrical Machine Systems - computer simulation*. Wiley, 1993.

[46] W. I. Rowen. Simplified mathematical representations of heavy-duty gas turbines. *Journal of engineering for power*, 105(4):865–869, 1983.

[47] P. Anderson and A. Fouad. *Power System Control and Stability*. Mnpere, 2002.

[48] S.J. Chapman. *Electric Machines Fundamentals*. McGraw Hill, 2005.

[49] Statoil. E-mail correspondance with specialists.

[50] P. Jones, L. Stendius, and ABB Sweden. The Challenges of Offshore Power System Construction-Troll A, Electrical Power delivered successfully to an oil and gas platform in the North Sea. *EWEC*, 2006.

[51] M. Hyttinen and K. Bentzen. Operating experiences with a voltage source converter (hvdc-light) on the gas platform troll a. *Energex, Stavanger, Norway*, 2006.

[52] Tore Undeland, Marta Molinas, Jon Are Suul, and Chandra Bajracharya. Understanding of tuning techniques of converter controllers for vsc-hvdc. *Nordic Workshop on Power and Industrial Electronics(NORPIE)*, 2008.

[53] SML Kabir and R. Shuttleworth. Brushless exciter model. In *IEE Proceedings - Generation, Transmission and Distribution*, volume 141, pages 61–67. IET, 1994.

[54] Jon Are Wold Suul. Control of variable speed pumped hydro power plant for increased utilization of wind energy in an isolated grid. Master's thesis, Norwegian University of Science and Technology, 2006.

[55] IEC. IEC 61892 - Mobile and Fixed Offshore Units.

[56] JW Umland and M. Safiuddin. Magnitude and symmetric optimum criterion for the design of linear control systems: what is it and how does it compare with the others? *IEEE Transactions on Industry Applications*, 26(3):489–497, 2002.

Appendix A

Park Transform

The Park Transform that is used is voltage-invariant, and given by [42]:

$$\begin{bmatrix} v_d \\ v_q \\ v_0 \end{bmatrix} = \frac{2}{3} \cdot \begin{bmatrix} \cos(\theta) & \cos(\theta - \frac{2\pi}{3}) & \cos(\theta + \frac{2\pi}{3}) \\ -\sin(\theta) & -\sin(\theta - \frac{2\pi}{3}) & -\sin(\theta + \frac{2\pi}{3}) \\ \frac{1}{2} & \frac{1}{2} & \frac{1}{2} \end{bmatrix} \cdot \begin{bmatrix} v_a \\ v_b \\ v_c \end{bmatrix} \tag{A.1}$$

The inverse transform is [42]:

$$\begin{bmatrix} v_a \\ v_b \\ v_c \end{bmatrix} = \begin{bmatrix} \cos(\theta) & -\sin(\theta) & 1 \\ \cos(\theta - \frac{2\pi}{3}) & -\sin(\theta - \frac{2\pi}{3}) & 1 \\ \cos(\theta + \frac{2\pi}{3}) & -\sin(\theta + \frac{2\pi}{3}) & 1 \end{bmatrix} \cdot \begin{bmatrix} v_d \\ v_q \\ v_0 \end{bmatrix} \tag{A.2}$$

During balanced conditions, $v_0 = 0$.

Appendix B

Tuning Criteria

Two criteria are applied in the tuning process of the different controllers, namely modulus and symmetrical optimum. See [56] and [52] for a thorough description of the criteria, the results and applications will be stated below.

B.1 Modulus Optimum

The modulus optimum criterion is applied to systems with transfer functions as shown in Fig. B.1. It is assumed that $T_a >> T_b$. The optimal values for T_i and K_p is then [56]:

$$\begin{aligned} T_i &= T_a \\ K_p &= \frac{T_a}{2K \cdot T_b} \end{aligned} \tag{B.1}$$

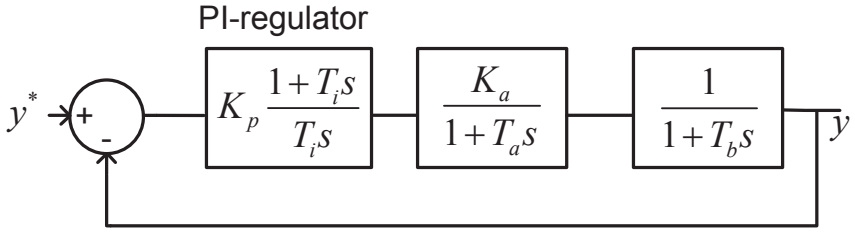

Fig. B.1: Modulus Optimum Transfer Function

B.2 Symmetrical Optimum

When the open loop transfer function contains two integrators as in Fig. B.2, modulus optimum will give a marginal stable system with a phase margin equal to zero. This is not feasible, so another technique is applied. The idea behind symmetrical optimum is to use the controller zero to increase the phase of the closed-loop transfer function bode plot, before it is decreased by the pole in T_a. In order to achieve this, $T_i = a^2 T_a$, where the constant a is set to 2 and 3 in [56] and [52], respectively. The value $a = 3$ is chosen here, yielding the following control parameters [52]:

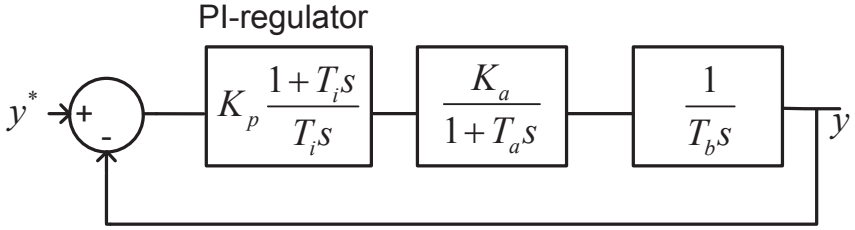

Fig. B.2: Symmetrical Optimum Transfer function

$$\begin{aligned} T_i &= 9 \cdot T_a \\ K_p &= \frac{T_b}{3K \cdot T_a} \end{aligned} \tag{B.2}$$

Appendix C

Tuning of System 1 Controllers

This chapter is taken from [18], and calculates the control parameters of System 1.

C.1 Inner Current Controller Tuning

The modulus optimum criterion is applied in the tuning process of the inner controller:

$$\begin{aligned} T_i &= \frac{L_{pu}}{R_{pu}} \\ K_p &= \frac{L_{pu}}{2T_a} \end{aligned} \tag{C.1}$$

L_{pu} and R_{pu} are the per-unit filter inductance and resistance between the converter and the connection point, see Fig. 3.8. T_a is the first-order time-delay of the converter, which is equal to $\frac{1}{2f_s}$ where f_s is the frequency of the PWM-carrier [52].

Applied to the SSC, the following control parameters are found:

$$\begin{aligned} T_{i,grid} &= \frac{0.15}{(2\pi \cdot 60) \cdot 0.01} = 0.03978 \\ K_{i,grid} &= \frac{0.15 \cdot 2 \cdot 5000}{2 \cdot (2\pi \cdot 60)} = 1.9893 \end{aligned} \tag{C.2}$$

The values from (C.2) are also found to be adequate also in the GSC. A simulation of the SSC inner current step response is carried out for both the detailed and average VSC-model. The DC-link has a constant voltage and the DC-side is connected to an infinite bus. The results are shown in Fig. C.1 with blue and green lines for i_d and i_q, respectively. The average model simulation is red. Both i_d and i_q are responding very quickly to the step change. The settling time is less than 1 ms. There is no overshoot in the response, but i_d is slightly affected by the step change in i_q. It is observed that the average model gives a good approximation to the detailed model.

C.2 Pitch Control Tuning

There are several objectives that the pitch controller should achieve. Its main function is to limit the mechanical torque from the wind to the rated value during high wind speeds. But it should also ensure that the mechanical stress acting on the pitching motor does not create fatigue damage. This will cause frequent maintenance and shorter lifetime. There is a trade-off between the ability to follow the reference angle and the mechanical strain on the motor and blades. The control parameters are obtained after comparing several runs of the system, giving the following values in pu:

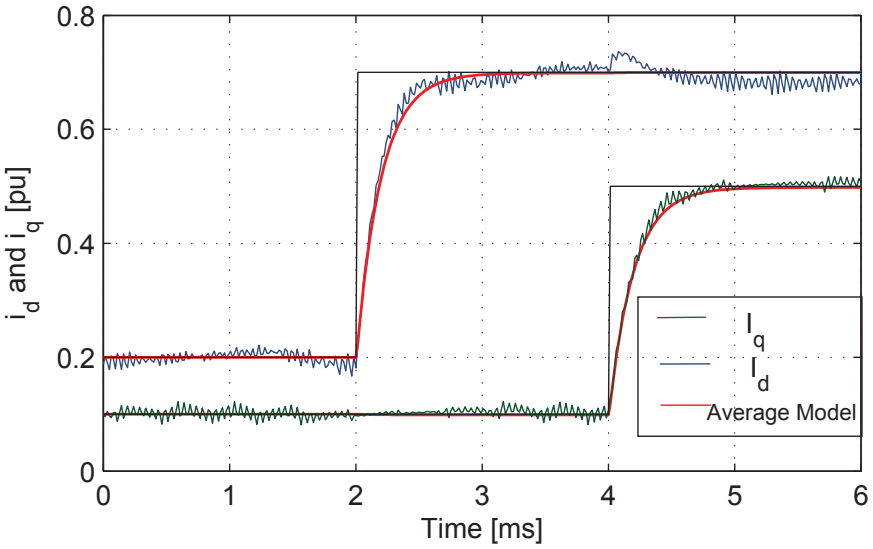

Fig. C.1: Inner current step responses

$$T_\beta = 0.2$$
$$K_\beta = 5 \tag{C.3}$$

The rate limiter from Fig. 3.4 is set to 3 deg/sec. This is a conservative number, values between 2 to 8 are found in other literature.

C.3 Speed Control Tuning

The tuning of the speed control loop of the generator is more complex than the inner current controller. The aerodynamical processes impose nonlinearities on the system. Analytical techniques could be applied, see [39]. In this work, the control values are found through simulation. Only the GSC is part of these simulations, and the DC-voltage is set constant.

The working point is chosen as $K_\omega = 3$ and $T_\omega = 1$. Both variables are changed in range of these values, keeping the other variable fixed. In Fig. C.2 K_ω is changed from 1 to 6. The resulting P and ω are shown. A high K_ω gives a good tracking of the reference speed shown in black, and it is seen that both the overshoot and settling time decreases when K_ω increases. The drawback with a high gain is that the ripple in output power is large. This follows from the fact that if the turbine is allowed to accelerate faster, the control system must permit faster changes in the electrical torque, see (3.6). Faster changes in torque is analogous with faster changes in power since the rotational speed variations are slow. Following this reasoning, a suitable trade-off between speed tracking and power fluctuations must be chosen.

In Fig. C.3 T_ω is varied from 0.5 to 4 while $K_\omega = 3$. From control theory, a low value of integration time means that it takes shorter time to build up the integrator output, hereby yielding a faster response. Regarding the simulations in Fig. C.3, a high value seems best both regarding power fluctuations and speed tracking. However, a too high T_ω would give a long delay before the speed reaches its reference. This would give lower output power

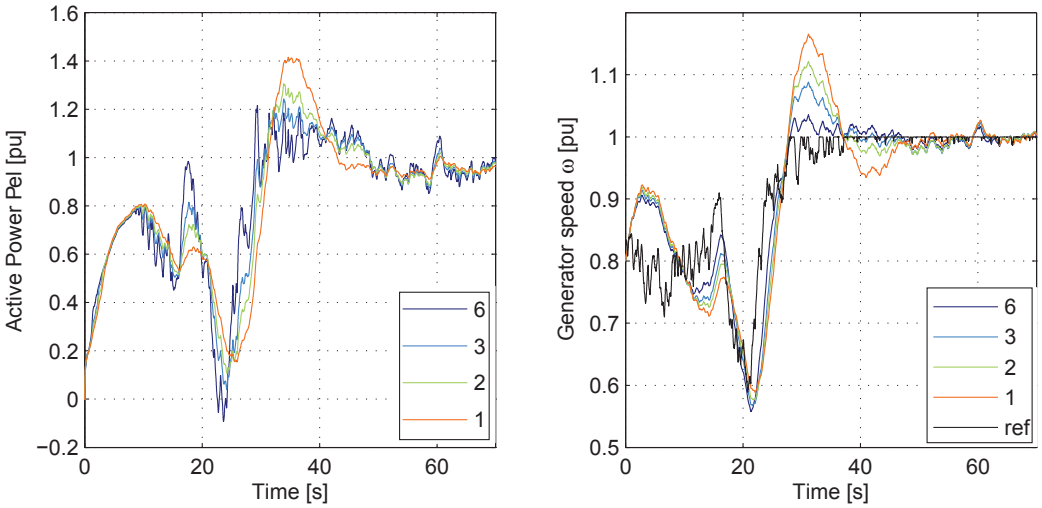

Fig. C.2: Varying K_ω with $T_\omega = 1$

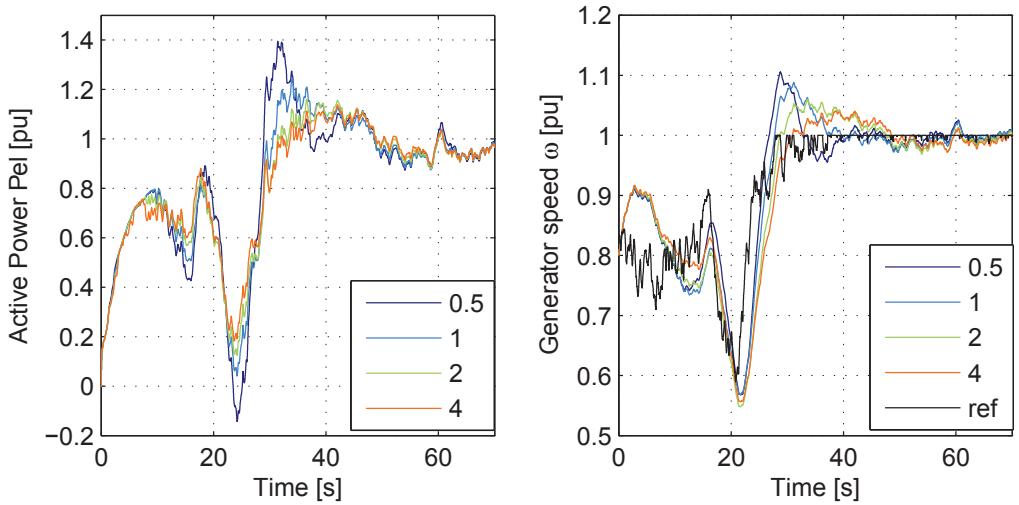

Fig. C.3: Varying T_ω with $K_\omega = 3$

since the ability to follow λ_{opt} is weakened.

Following the discussion above, tracking of the speed reference is improved with either an increase in K_ω or a decrease in T_ω. At the same time, both these actions create larger electrical power spikes. Based on the simulations and discussions, the following values are chosen:

$$\begin{aligned} T_i &= 4 \\ K_p &= 3 \end{aligned} \tag{C.4}$$

C.4 DC-link Voltage controller

The DC-link controller is tuned by using the symmetrical optimum tuning criteria . This gives the following values for the gain and integration time [56] [41]:

$$\begin{aligned} T_i &= a^2 T_{eq} \\ K_p &= \frac{C}{aK \cdot T_{eq}} \end{aligned} \tag{C.5}$$

T_{eq} is the first order time constant of the inner control loop, C is the per unit DC-link capacitance, $K = \frac{V_{p,d}}{V_{DC}}$ is equal to 1pu during normal operation, and a is a degree of freedom in the controller. Both $a = 2$ and $a = 3$ are used in the literature [56] [41], here $a = 3$ will be used. The control parameters are then:

$$\begin{aligned} T_i &= 9 \cdot 2 \cdot 10^{-4} = 0.0018 \\ K_p &= \frac{5 \cdot 10^{-3}}{3 \cdot 2 \cdot 10^{-4}} = 8.333 \end{aligned} \tag{C.6}$$

A simulation where the reference in V_{dc} is changed from 1 to 0.9 pu is performed. The AC-side is connected to an infinite bus, and the DC-side is just the capacitor. This is not a realistic simulation, since the voltage reference always is equal to 1pu during operation. Some of the assumptions and simplifications to (3.11) will not be valid. However, since the change in reference is small, the simulation will give a good impression of the controller dynamics. The simulation shows that the controller have a fast response with a settling

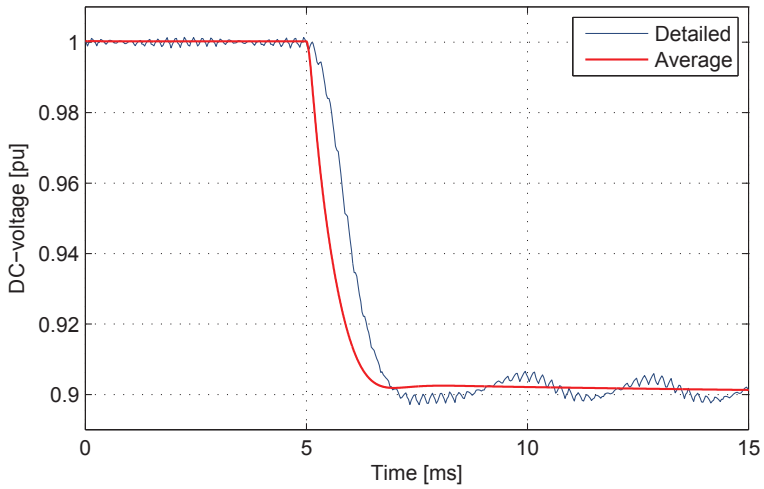

Fig. C.4: Step response in V_{dc}

time of $2ms$. The average model simulation is shown with red, and has a similar response, except from a smaller time-delay and less oscillations. The symmetrical optimum tuning technique yield a small overshoot in the response [41]. This is observed for both models.

Appendix D

Tuning of System 2 Controllers

D.1 SM Stator Current Control Tuning

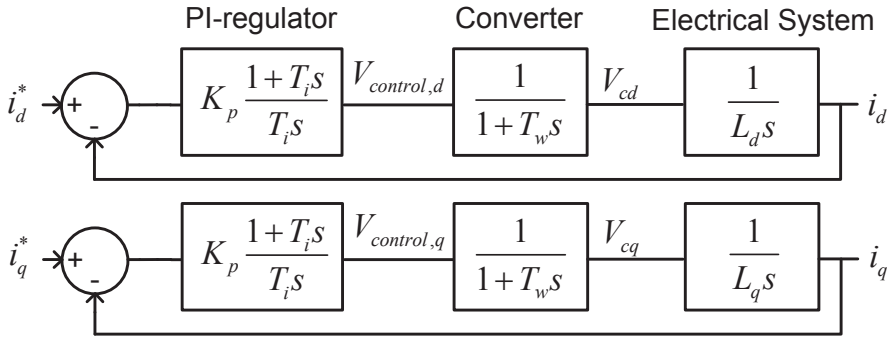

Fig. D.1: Block Diagram of SM Current Control

As the resistance in the stator is neglected, the open loop transfer function contains two pure integrators as shown in Fig. D.1. The symmetrical optimum tuning criteria is then applied, yielding the following control parameters:

$$\begin{aligned} T_i &= 9 \cdot \frac{1}{2 \cdot 2000} = 0.0025 \\ K_p &= \frac{1.25}{2 \cdot \pi \cdot 60} \frac{1}{2 \cdot 0.0025} = 6.632 \end{aligned} \tag{D.1}$$

The resulting closed loop transfer function is of high order since no pole is cancelled by the controller zero. A simplified first-order model is found from a step-response simulation in Matlab. The exact response is plotted, and a first-order simplification is obtained by trial and error. The exact and simplified responses are shown in Fig. D.3, and they match well except from the overshoot in the exact response.

The following simplified transfer function will represent the current control loop when designing outer controllers:

$$\begin{aligned} \frac{i_d}{i_d^*}(s) &= \frac{1}{1 + 0.0015s} \\ \frac{i_q}{i_q^*}(s) &= \frac{1}{1 + 0.0015s} \end{aligned} \tag{D.2}$$

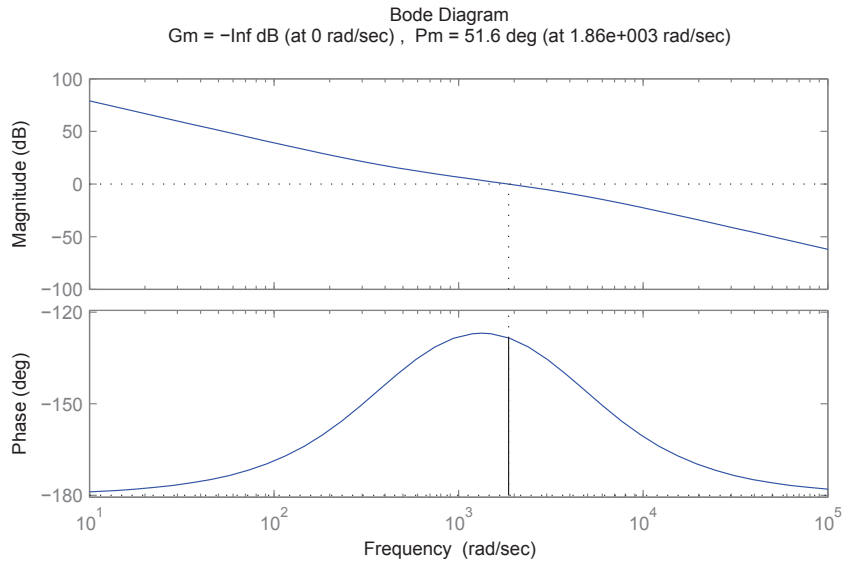

Fig. D.2: Bode Diagram of SM Current Control

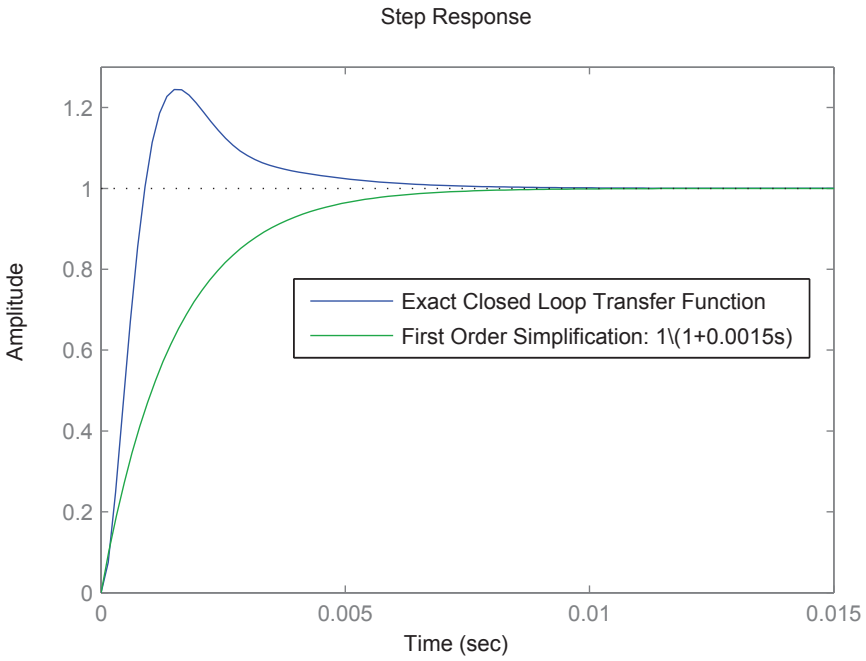

Fig. D.3: Step response of Current Control Loop

D.2 Tuning of SM Field Current Controller

This section describes the tuning process of the field current controller of the synchronous motor in section 4.4. The simplified closed loop transfer function of the field current control is repeated in Fig. D.4. The numerical values for the time-constants are $T_{fv} = 1s$ and $T'_{d0} = 6.6$.

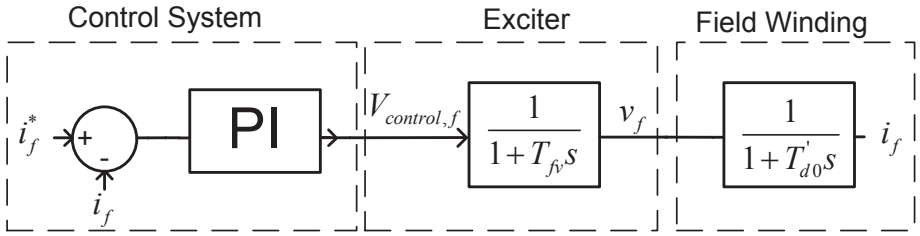

Fig. D.4: Block Diagram of Field Current Control

The modulus optimum criteria could be applied, but the condition $T'_{d0} >> T_{fv}$ is not satisfied. Still, the controller pole is used to cancel the domiant T'_{d0}. However, if the gain from (B.1) is used, one would get $K_p = \frac{6.6}{2 \cdot 1} = 3.3$. This value yield a too high phase margin, so the gain is increased to $K_p = 10$ in order to get a smaller phase margin.

Fig. D.5 show the Bode plot when $T_i = 6.6$ and $K_p = 10$. These control parameters are found to be adequate, and will be used in the simulations.

$$\begin{aligned} T_i &= 6.6 \\ K_p &= 10 \end{aligned} \tag{D.3}$$

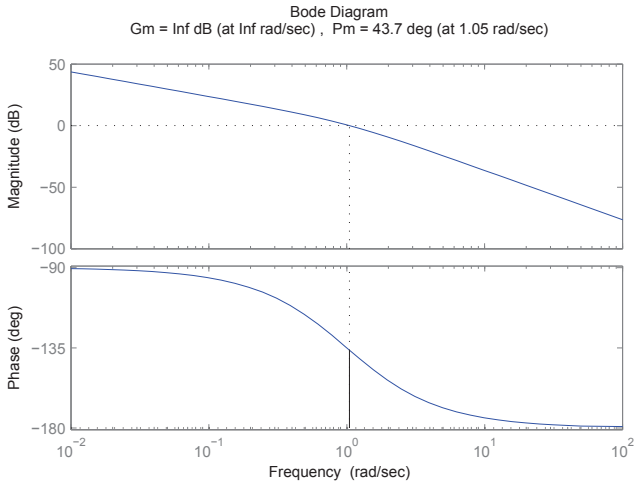

Fig. D.5: Bode Diagram with $T_i = 6.6$ and $K_p = 10$

D.3 Tuning of SM speed controller

The speed controller of the synchronous motor in section 4.4 is tuned according to the symmetrical optimum criterion from section D. The closed loop transfer function is repeated in Fig. D.6.

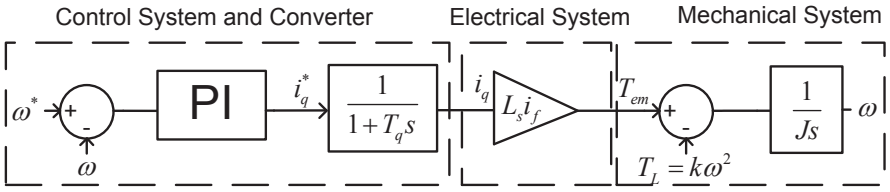

Fig. D.6: Block Diagram of Speed Control

Note that the first order simplification from (D.2) is used, such that $T_q = 0.0015$. The controller parameters are found directly from (B.2) and are given in (D.4). However, the gain $L_s i_f$ in Fig. D.6 is not constant since the field current i_f varies. The rated value is assumed for the tuning process, hence $L_s i_f = 1$.

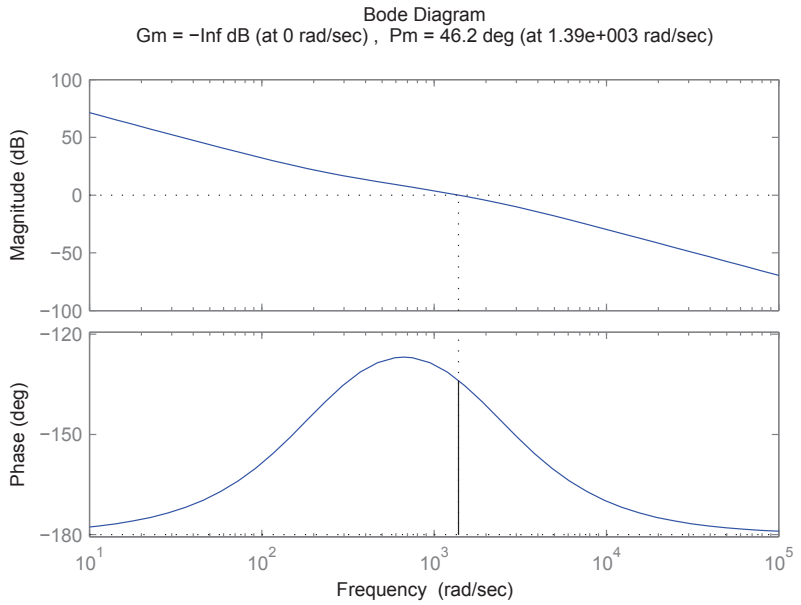

Fig. D.7: Bode Diagram with $T_i = 0.0045$ and $K_p = 2000$

$$
\begin{aligned}
T_i &= 9 \cdot 0.0015 = 0.0135 \\
K_p &= \frac{3}{3 \cdot 0.0015} = 666.7
\end{aligned}
\tag{D.4}
$$

D.4 Tuning of DC-link Controller

The DC-link voltage controller from section 4.6 is tuned according to the symmetrical optimum criterion from section B. The closed loop transfer function is given in Fig. D.8.

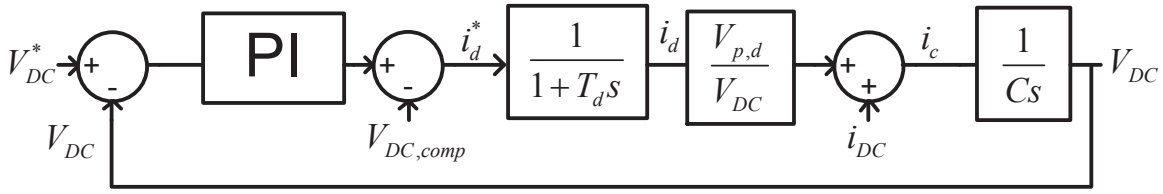

Fig. D.8: Transfer Function of DC-voltage control

Note that the first order simplification of the current from [42] is used, such that $T_d = 2\frac{1}{2 \cdot f_s} = 5 \cdot 10^{-4}$. The gain $\frac{V_{p,d}}{V_{DC}} = \frac{120}{94.71}$ can be recognized in (3.11). The per unit Capacitance is calculated from $C_{pu} = \frac{\frac{1}{2}CV_{DC}^2}{S_n} = \frac{0.5 \cdot 9.8 \cdot 10^{-6} \cdot (120 \cdot 10^3)^2}{2 \cdot 45 \cdot 10^{-6}} = 1.568 \cdot 10^{-3}$. The controller parameters are calculated from (B.2) and are given in (D.4).

$$
\begin{aligned}
T_i &= 9 \cdot 0.0005 = 0.0045 \\
K_p &= \frac{3 \cdot 1.568 \cdot 10^{-3}}{\frac{120}{94.71} \cdot 0.0005} = 0.825
\end{aligned}
\tag{D.5}
$$

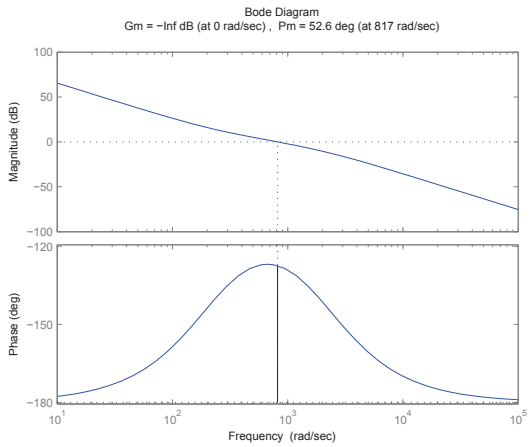

Fig. D.9: Bode Diagram of DC-voltage Controller

Appendix E

Derivation of i_d^* and i_f^*

This section gives the derivation of the references i_d^* and i_f^* used to control the synchronous motor in section 3.9. This work is proposed by the author. The optimization problem is formulated as:

$$\begin{aligned}
&Minimize\{F\} \\
&F = i_d^2 + i_q^2 \\
&v_{cd}^2 + v_{cq}^2 = \omega|\psi_s| \\
&v_{cd} = \omega L_s i_q \\
&v_{cq} = \omega L_s i_d + \omega L_m i_f \\
&T_{em} = L_m i_f i_q
\end{aligned} \tag{E.1}$$

where the values of ω and T_{em} are fixed. Two variables a and b are defined in order to facilitate the derivation. The goal is to express F in terms of a single variable so that ordinary differentiation can be applied. All variables except from a are substituted:

$$\begin{aligned}
a &= \frac{v_{cd}}{\omega} \quad b = \frac{v_{cq}}{\omega} \\
|v_c| &= \sqrt{v_{cd}^2 + v_{cq}^2} = \omega \cdot |\psi_{s,rated,pu}| = \omega \implies a^2 + b^2 = 1 \\
i_d &= \frac{b}{L_s} - \frac{T_{em}}{a} \\
i_q &= \frac{a}{L_s} \\
F &= \frac{a^2}{L_s^2} + \frac{b^2}{L_s^2} - \frac{2T_{em}b}{L_s a} + \frac{T_{em}^2}{a^2} \\
&= \frac{a^2}{L_s^2} + \frac{1-a^2}{L_s^2} - \frac{2T_{em}\sqrt{1-a^2}}{L_s a} + \frac{T_{em}^2}{a^2} \\
&= \frac{1}{L_s^2} - \frac{2T_{em}}{L_s}\sqrt{\frac{1}{a^2} - 1} + \frac{T_{em}^2}{a^2}
\end{aligned} \tag{E.2}$$

The minimum value of F occurs either on the boundary, i.e. $a \pm 1$, or when $\frac{dF}{da} = 0$. If $a = \pm 1$, then $b = v_{cd} = 0$, causing $i_q = 0$ and $T_{em} = 0$, contradicting the requirement of a fixed torque. The condition $\frac{dF}{da} = 0$ is then used in the rest of the derivation:

$$\begin{aligned}
\frac{dF}{da} = 0 \qquad &= -\frac{2T_{em}}{L_s} \frac{\frac{-2}{a^3}}{\sqrt{\frac{1}{a^2} - 1}} + \frac{-2T_{em}^2}{a^3} \\
&= \sqrt{\frac{1}{a^2} - 1} - \frac{1}{L_s T_{em}} \\
a \qquad &= \frac{L_s T_{em}}{\sqrt{(L_s T_{em})^2 + 1}} \\
b \qquad &= \sqrt{1 - a^2} = \frac{1}{\sqrt{(L_s T_{em})^2 + 1}}
\end{aligned} \tag{E.3}$$

i_f^* and i_d^* can now be calculated in terms of a and b:

$$\begin{aligned}
i_f^* \qquad &= \frac{L_s T_{em}}{L_m a} \\
&= \sqrt{1 + (L_s T_{em})^2} \\
i_d^* \qquad &= \frac{b - L_m i_f}{L_s} \\
&= -\frac{L_s T_{em}^2}{\sqrt{(L_s T_{em})^2 + 1}}
\end{aligned} \tag{E.4}$$

Appendix F

Additional Parameters

F.1 PMSG-parameters

Table F.1 show the per-unit parameters for the wind turbine PMSG. All reactances and time-constant are specified at unsaturated conditions.

Parameter	**Value**
Armature Time Constant $[T_a]$	0.332 s
d-axis reactance $[X_d]$	0.4 pu
q-axis reactance $[X_q]$	0.51 pu
Transient d-axis reactance $[X'_d]$	0.3 pu
Subtransient d-axis reactance $[X''_d]$	0.22 pu
Subtransient q-axis reactance $[X''_q]$	0.29 pu
Open d-axis transient time constant $[T'_{d0}]$	10 s
Open d-axis subtransient time constant $[T''_{d0}]$	0.001 s
Open q-axis subtransient time constant $[T''_{q0}]$	0.034 s
Air gap factor	1.0 pu

Table F.1: PMSG Parameters

F.2 Synchronous Generator Parameters

Table F.2 show the parameters of the synchronous generator on the oil platform in System 1. The values are found in [47].

Parameter	**Value**
Armature resistance $[R_a]$	0.0031 pu
d-axis reactance $[X_d]$	1.7 pu
q-axis reactance $[X_q]$	1.64 pu
Transient d-axis reactance $[X'_d]$	0.245 pu
Subtransient d-axis reactance $[X''_d]$	0.185 pu
Subtransient q-axis reactance $[X''_q]$	0.185 pu
Open d-axis transient time constant $[T'_{d0}]$	5.9 s
Open d-axis subtransient time constant $[T''_{d0}]$	0.033s
Open q-axis subtransient time constant $[T''_{q0}]$	0.076 s
Air gap factor	1.0 pu

Table F.2: Synchronous Generator Parameters

F.3 Synchronous Motor Parameters

Table F.3 show the parameters of the synchronous motor on Troll A in System 2. The values are found in [47].

Parameter	**Value**
Armature resistance $[R_a]$	0.0 pu
d-axis reactance $[X_d]$	1.25 pu
q-axis reactance $[X_q]$	1.25 pu
Transient d-axis reactance $[X'_d]$	0.209 pu
Transient q-axis reactance $[X'_q]$	0.3 pu
Subtransient d-axis reactance $[X''_d]$	0.11 pu
Subtransient q-axis reactance $[X''_q]$	0.116 pu
Open d-axis transient time constant $[T'_{d0}]$	6.6 s
Open q-axis transient time constant $[T'_{q0}]$	0.85 s
Open d-axis subtransient time constant $[T''_{d0}]$	0.04s
Open q-axis subtransient time constant $[T''_{q0}]$	0.1 s
Air gap factor	1.0 pu

Table F.3: Synchronous Motor Parameters

F.4 Wind Profile

A wind speed profile based on [33] is applied to simulations both in System 1 and System 2. The profile is shown in Fig. 5.1 a). The mean wind speed is initially 10 m/s. At $t = 10$ s there is a gust with amplitude -3 m/s and duration of 10 s. At $t = 30$ s a ramp increases the mean wind speed to 14 m/s during 30 s. Recall from section 3.1 that the wind speed which produces rated output is 12 m/s.

The following data describes the noise in the wind:

- Number of Noise Components: 250
- Noise Amplitude Controlling Parameter: 10 [rad/s]
- Surface Drag Coefficient: 0.0192
- Turbulence Scale: 600m
- Time Interval for Random Generation: 0.35 s

Appendix G

Summary of IEC-61892

Table G.1 shows the data from IEC-61892 that is used in this report. The data is shown both as per unit and with respect to the operating values on the platform in System 1.

Parameter	**Per Unit**	**Platform Base**
Transient voltage limits	0.9-1.06 pu	11.04-16.56 kV
Stationary voltage limits	0.8-1.2 pu	12.42-14.63 kV
Transient frequency limits	0.9-1.1 pu	54-66 Hz
Stationary frequency limits	0.95-1.05 pu	57-63 Hz

Table G.1: IEC-61892 key data

Appendix H

PSCAD Simulation Model

The most relevant parts of the simulation models are shown in the next pages. 6 screenshots are made, and they are given in the following order:

- System 1: Wind farm and submarine cable model
- System 1: Average model system side converter (SSC)
- System 1: Average model generator side converter (GSC)
- System 1: Detailed model generator side converter (GSC) (For Illustration)
- System 1: Oil platform model
- System 2: Main View

The converter models are not shown for System 2, because they share so many similarities with the converters in System 1.

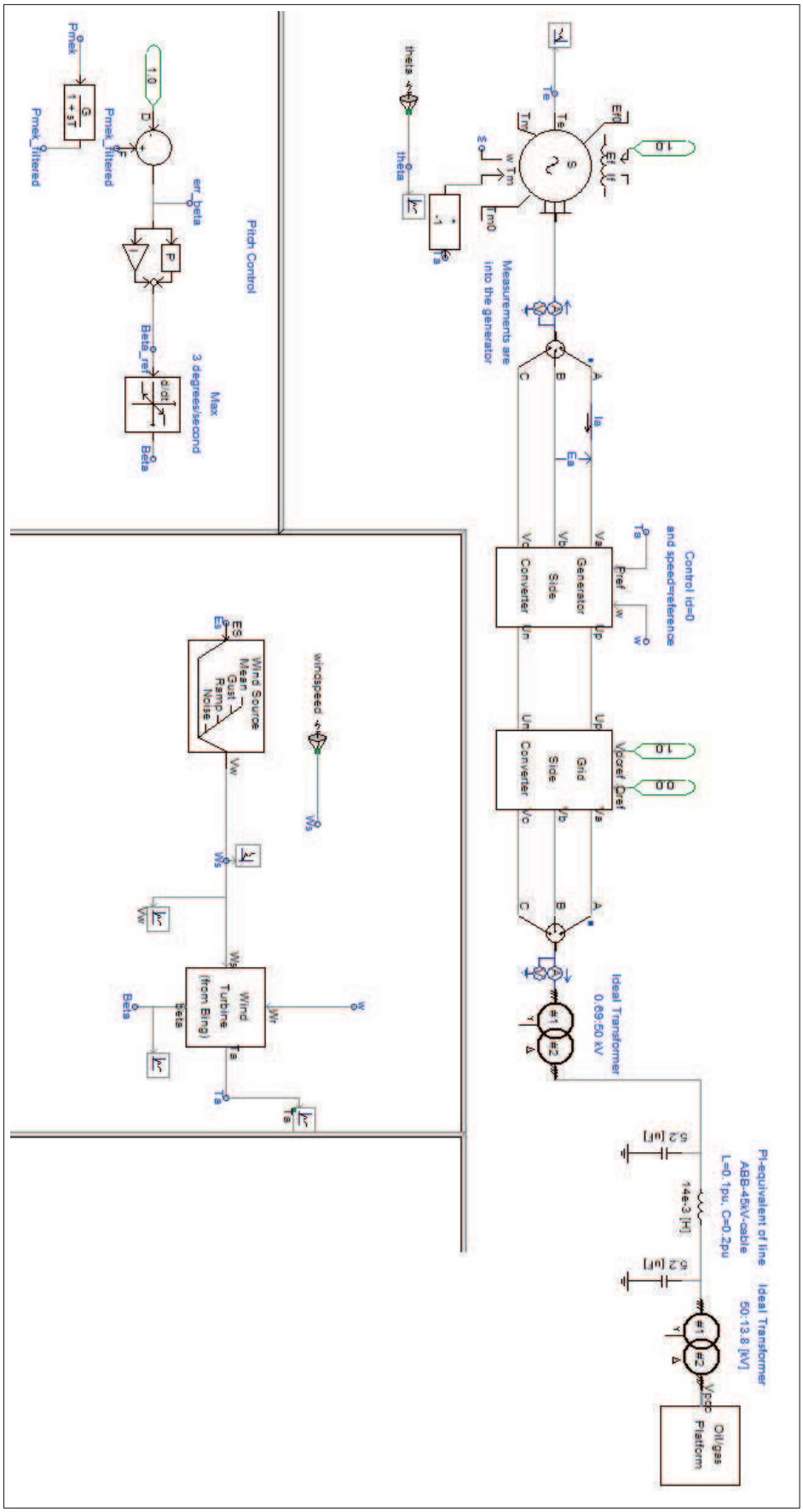
Pmek
G
1 + sT
Pmek_filtered
1.0
D
F
Pmek_filtered
err_beta
I
P
Beta_ref
dbdt
Beta
Max
3 degrees/second
Pitch Control
theta
theta
-1
Ta
Te
Tm
w Tm
Tm0
Measurements are
into the generator
Ia
Ea
Control id=0
and speed=reference
Ta
Pref
w
Generator
Side
Converter
Grid
Side
Converter
Vdcref
Qref
Ideal Transformer
0.69:50 kV
#1
#2
Pi-equivalent of line
ABB-45kV-cable
L=0.1pu, C=0.2pu
14e-3 [H]
Ideal Transformer
50:13.8 [kV]
Vpcc
Oil/gas
Platform
windspeed
Ws
Wind Source
Mean
Gust
Ramp
Noise
Vw
Wind
Turbine
(from Bing)
Beta
Ta
w

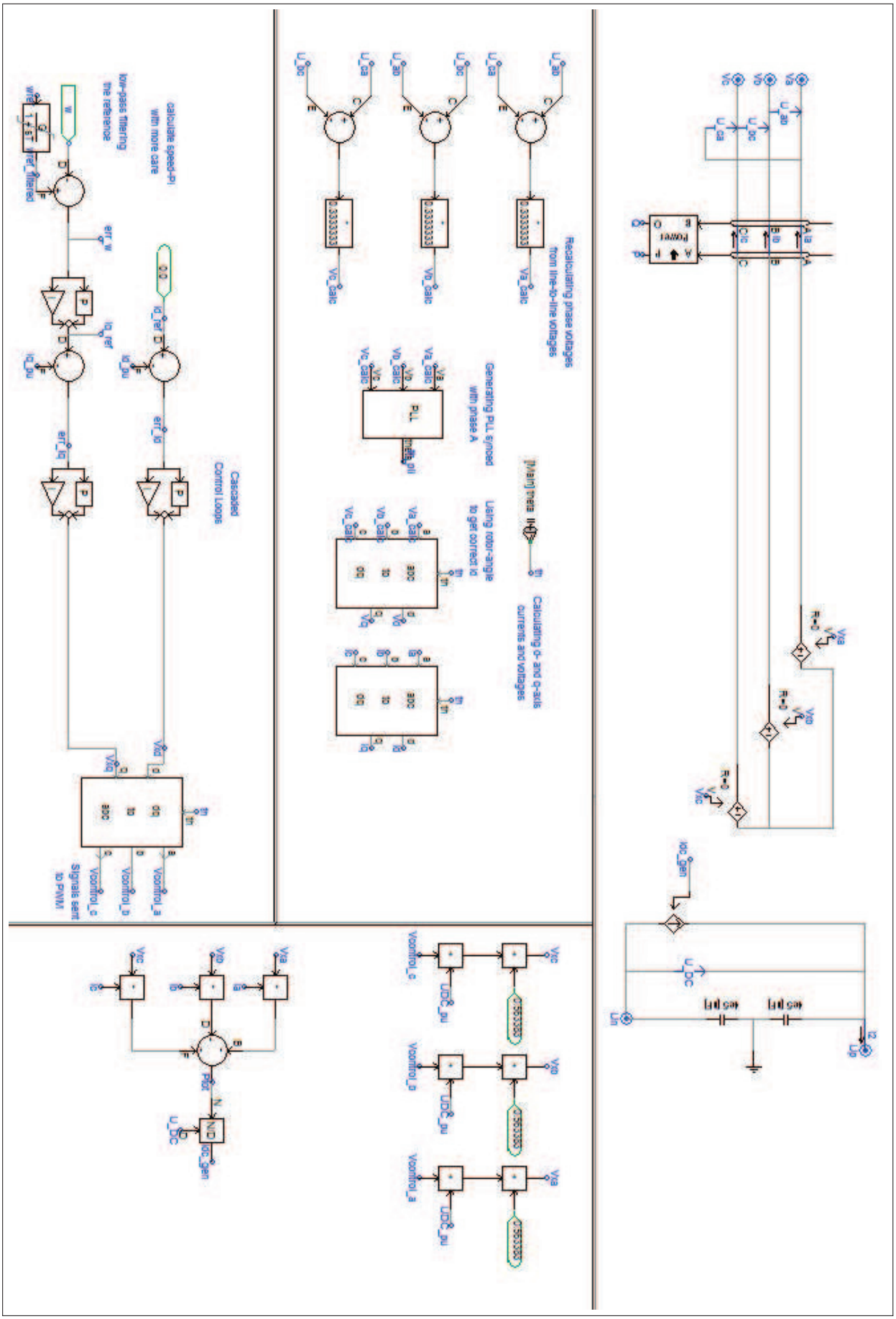
Recalculating phase voltages from line-to-line voltages
Generating PLL sy/nsed with phase A
Using rotor-angle to get correct id
Calculating d- and q-axis currents and voltages
Cascaded Control Loops
calculate speed-PI with more care
low-pass filtering the reference
Signals sent to PWM
Power
PLL
abc
dq
to
Udc_gen
U_DC

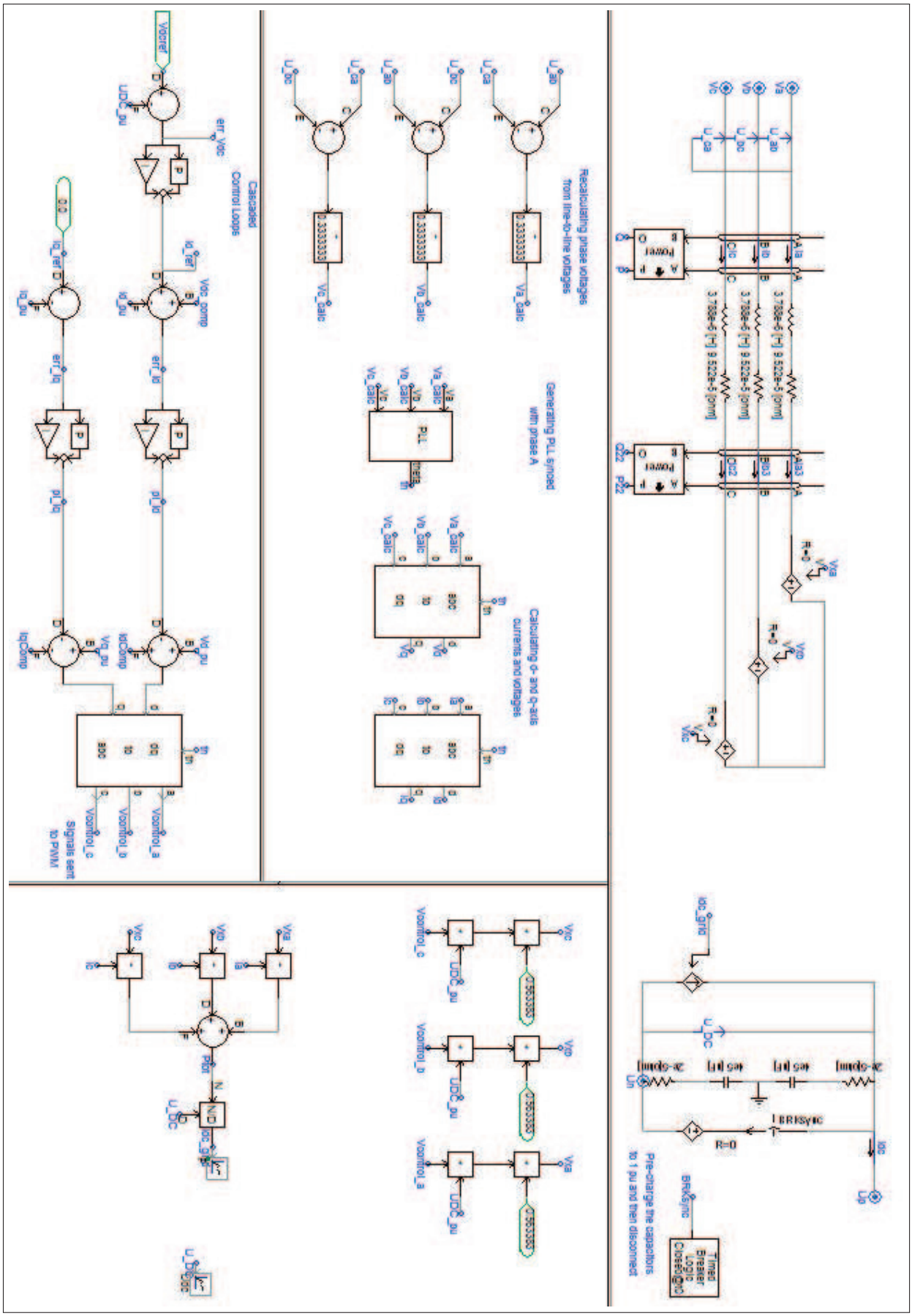
Vdcref
err_Vdc
Cascaded
Control Loops
id_ref
iq_ref
err_id
err_iq
pi_id
pi_iq
Vdc_comp
idComp
iqComp
Vd_pu
Vq_pu
Voconfrol_a
Voconfrol_b
Voconfrol_c
Signals sent
to PWM
Recalculating phase voltages
from line-to-line voltages
Va_calc
Vb_calc
Vc_calc
Generating PLL synced
with phase A
PLL
Calculating d- and q-axis
currents and voltages
abc
dq
Va
Vb
Vc
Vxa
Vxb
Vxc
Power
R=0
Idc_grid
U_DC
BRKSync
Timed
Breaker
Logic
Pre-charge the capacitors
to 1 pu and then disconnect
Idc
Ug
UDC_pu
U_DC_calc

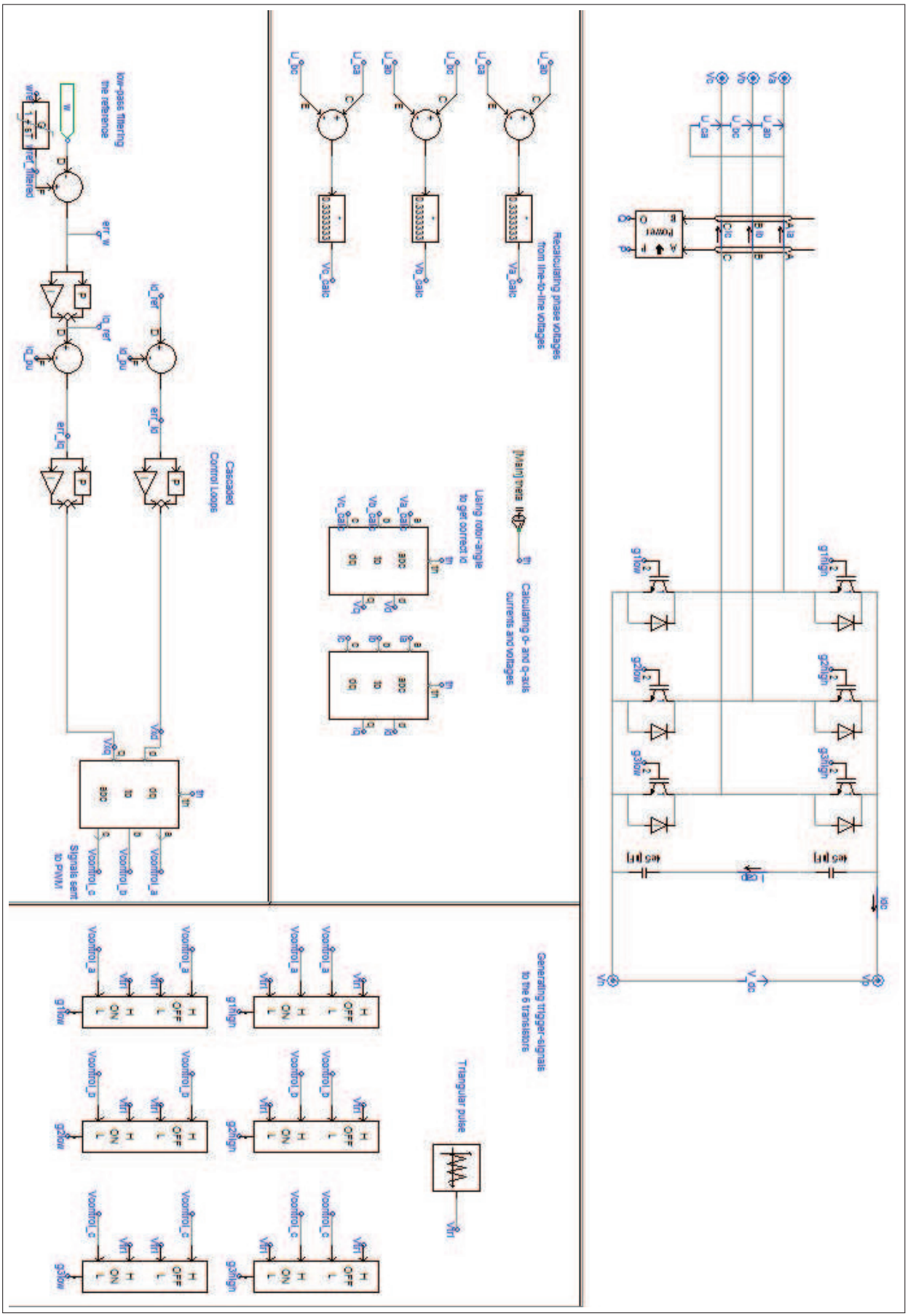
Low-pass filtering the reference
Cascaded Control Loops
Signals sent to PWM
Recalculating phase voltages from line-to-line voltages
Using rotor-angle to get correct id
Calculating d- and q-axis currents and voltages
Generating trigger-signals to the 6 transistors
Triangular pulse

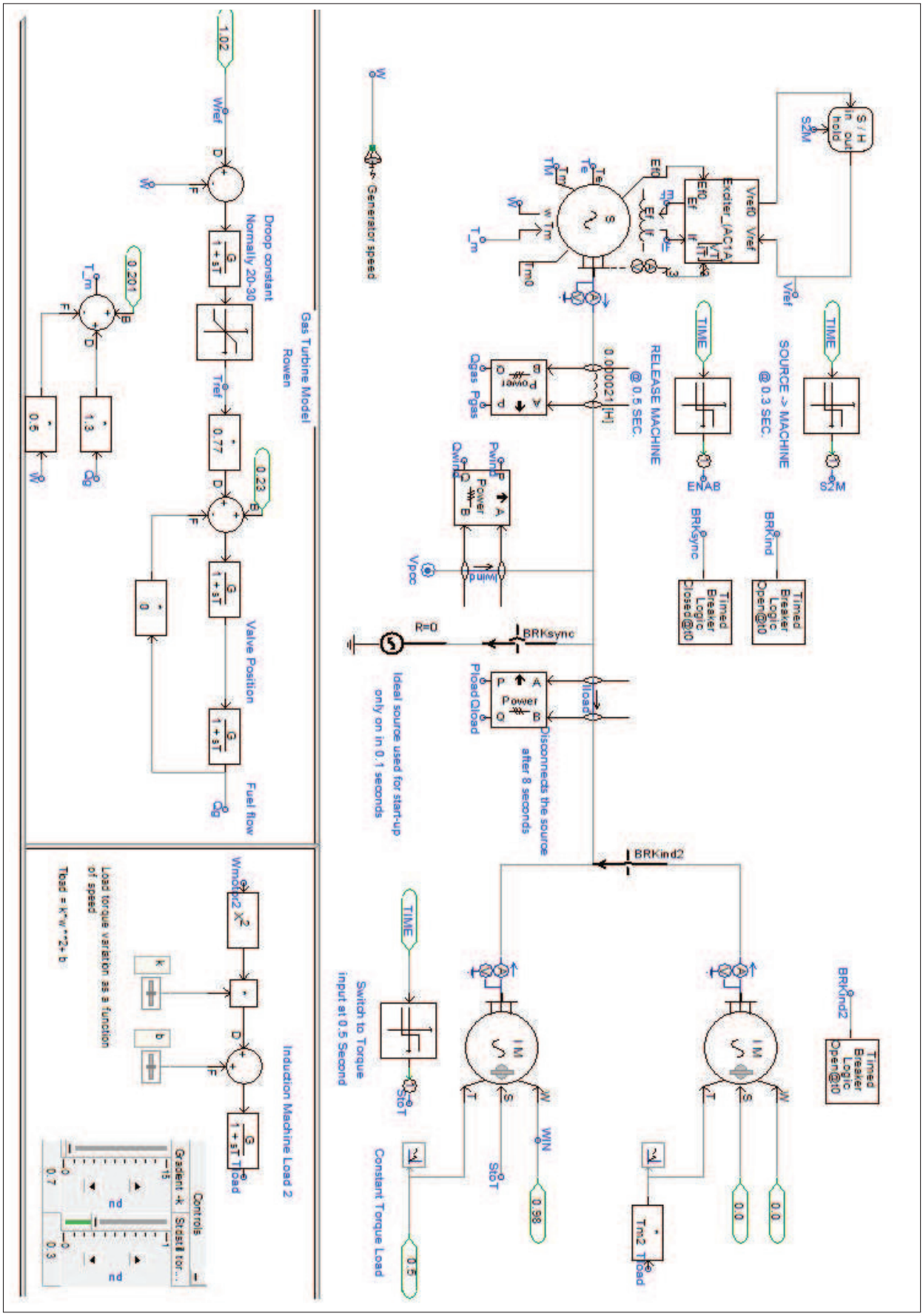
Gas Turbine Model
Rowen
Droop constant
Normally 20-30
Valve Position
Fuel flow
Induction Machine Load 2
Load torque variation as a function of speed
Tload = K*w**2+ b
Generator speed
RELEASE MACHINE @ 0.5 SEC.
SOURCE -> MACHINE @ 0.3 SEC.
Disconnects this source after 8 seconds
Ideal source used for start-up only on in 0.1 seconds
Switch to Torque input at 0.5 Second
Constant Torque Load
BRKsync
BRKind2
R=0

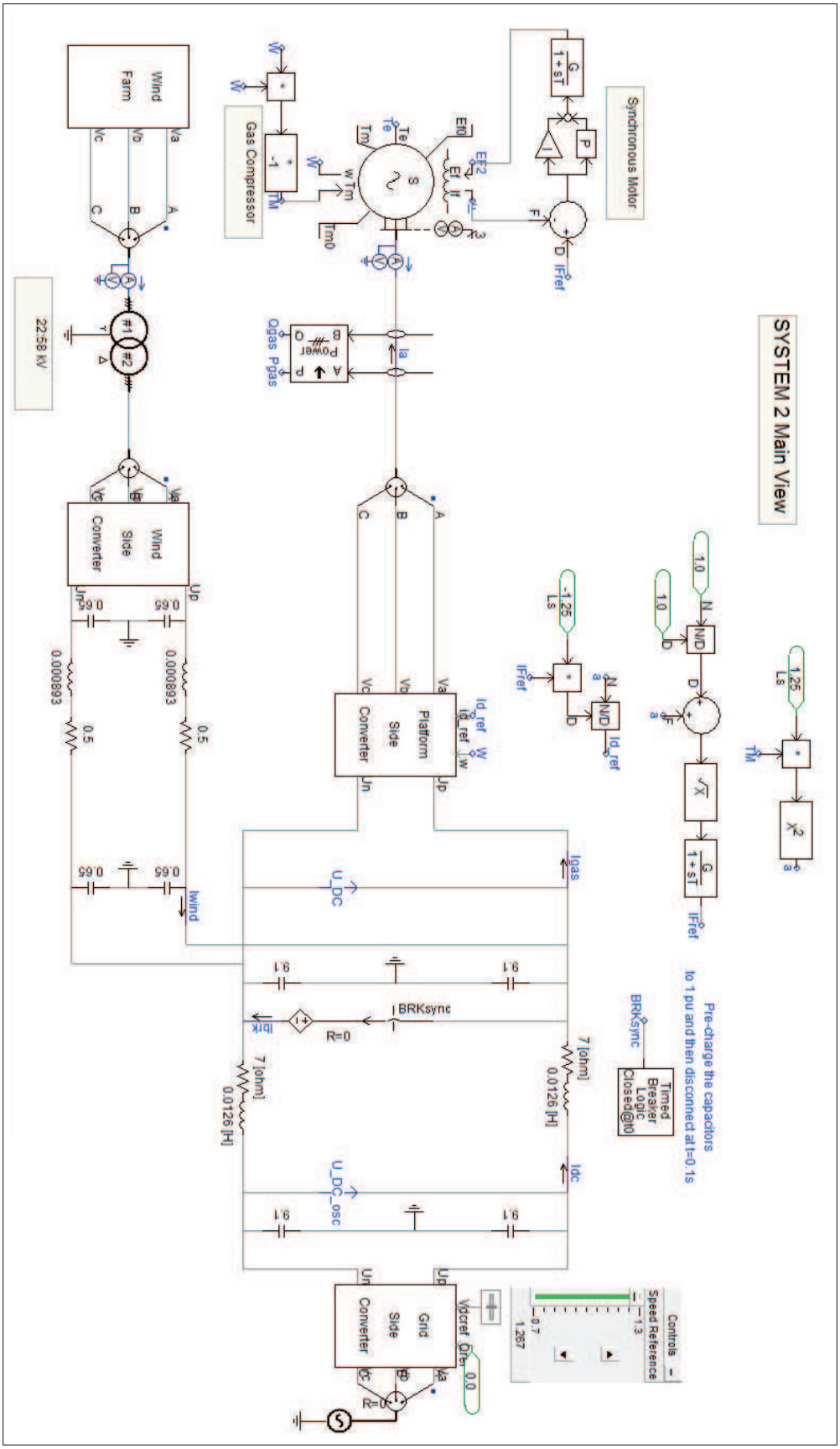
SYSTEM 2 Main View
Synchronous Motor
Gas Compressor
Wind Farm
22:58 kV
Wind Side Converter
Platform Side Converter
Grid Side Converter
U_DC
U_DC_osc
Igas
Iwind
Idc
BRKsync
R=0
7 [ohm]
0.0126 [H]
0.000893
0.5
0.65
9.1
Pre-charge the capacitors to 1 pu and then disconnect at t=0.1s
Timed Breaker Logic
Controls
Speed Reference

Appendix I

Additional plots and Matlab-code

I.1 MPPT-plot

The following scripts generate Fig. 3.2 and 3.3.

```
R=37.5;
A=pi*R^2;
rho=1.29;
k=0.5*rho*A;
hold on;
j=1;
tab2=colormap(hot);
colorindex=3;
subplot(1,2,1);
for w=0.5:0.1:2
    hold on;
    v=0:0.1:25;
    lambda=w*R./v;
    CP=cp(0,lambda);
    P=k.*CP.*v.^3;
    j=j+1;
    plot(v,P,'Color',tab2(colorindex,:))
    colorindex=colorindex+3;
end
axis([0 25 0 5e6]);
hold off;
subplot(1,2,2);
hold on;
tab2=colormap(hot);
colorindex=3;
w=2;
for beta=1:3:30
    v=0:0.1:25;
    lambda=w*R./v;
    CP=cp(beta,lambda);
    P=k.*CP.*v.^3;
    plot(v,P,'Color',tab2(colorindex,:))
    colorindex=colorindex+5;
end
axis([0 25 0 5e6]);
```

```
function tmp=cp(beta,lambda)
l2=lambda_i(beta,lambda);
tmp=0.5.*(116./l2 - 0.4.*beta - 5).*exp(-21./l2);

function tmp=lambda_i(beta,lambda)
tmp=1./(1./(lambda+0.08.*beta)-0.035./(beta.^3+1));


beta=0;
lambda=0:0.01:15;
%Calculation Cp from the above functions
C_P=cp(beta,lambda);

plot(lambda,C_P);
axis([0 14 0 0.5]);
```

I.2 Induction Motor Load Profile

The constants b and k are chosen as 0.2 and 0.8, respectively. See Fig. I.1 for a plot of the profile.

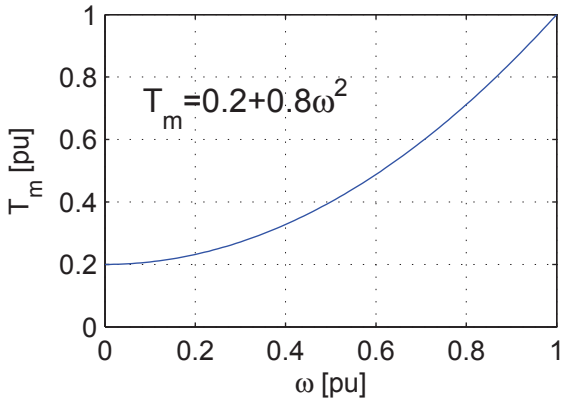

Fig. I.1: Induction Motor Load Profile

I.3 Induction Motor torque-slip plot

Fig. I.2 show how different values of rotor resistance R_2 have impact on the torque-slip profile. The Matlab code for the plot is also given.

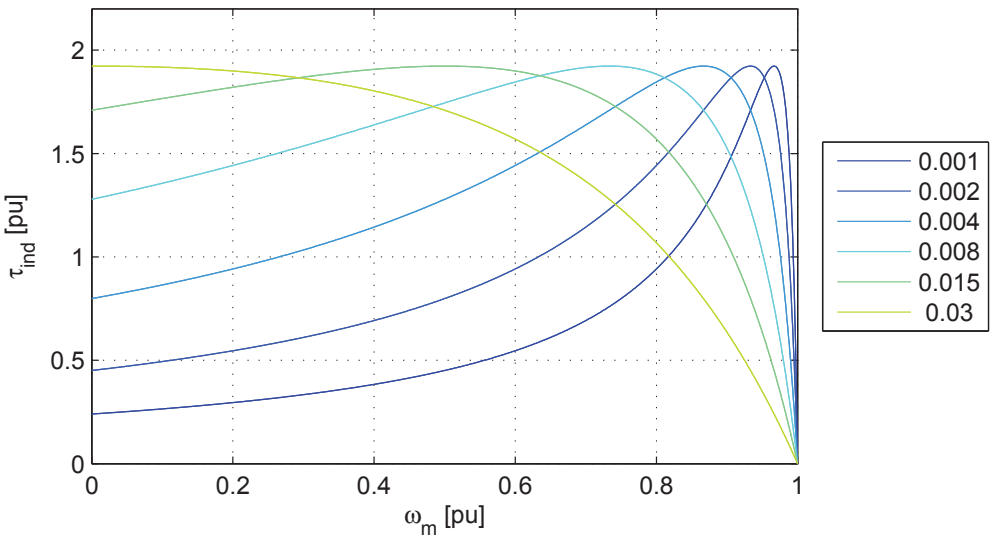

Fig. I.2: Torque-slip characteristics for different R_2

The following code generates Fig. I.2.

```
%Defining reactances/resistances
Rth=0.03;
Xth=0;
X2=0;

%Thevenin Voltage set to 1pu
Vth=1;

%Defining slip range
s=-0.0051:0.001:1;
hold on;

%Colors
tab=colormap(jet);
c1=tab(1,:);
c2=tab(15,:);
c3=tab(30,:);
c4=tab(45,:);

%Defnining the rotor resistances
R2tab=[0.001 0.002 0.004 0.008 0.015 0.03];
for i=1:length(R2tab);
    R2=R2tab(i);
    wsync=1;
    T=(0.05*2/1.3).*3*Vth*R2./...
        (s.*wsync.*((Rth+R2./s).^2+(Xth+X2)^2));
    w=wsync.*(1-s);
    plot(w,T,'Color',tab(i*6,:));
end

%Plotting
axis([0 1 0 2.2]);
box on;
grid on;
legend(num2str(R2tab.'),'Location','EastOutside');
xlabel('\omega_m [pu]');
ylabel('\tau_{ind} [pu]');
```

Appendix J

Paper presented at EPE Wind Energy Chapter

This paper was presented at the EPE Wind Energy Chapter conference that took place in Trondheim 9-11. May 2011. It contains a brief system description of System 1, in addition to the sensitivity analysis that also is presented in the thesis.

Parametric sensitivity of Transients in an Islanded System with an Offshore Wind Farm Connected to an Oil Platform

†Atle Rygg Årdal, Salvatore D'Arco, Raymundo E. Torres-Olguin , Tore Undeland and ‡Kamran Shrarifabadi

† Norwegian University of Science and Technology (NTNU)
O. S. Bragstads plass 2E,
7034 Trondheim, Norway
Tel.: +47 73594210
Fax: +47 73594279
E-Mail: ardal@stud.ntnu.no
URL: http://www.ntnu.no

‡ Statoil ASA
NO-0246-Oslo, Norway
Tel: 047 480 99 053
E-Mail : kamsh@statoil.com
URL: http://www.statoil.com

Keywords

«Adjustable speed generation system», « Converter control »,
«Control methods for electrical system», «Simulation», «Wind energy»,

Acknowledgements

The work presented in this paper has been partly supported by the project "Power Electronics for Reliable and Energy Efficient Renewable Energy Systems" (http://www.sintef.no/OPE) at SINTEF Energy Research. The project is financed by The Norwegian Research Council, Wärtsila, Statkraft and GE Energy and sponsored by Westcode.

Abstract

Electrical power on offshore oil platforms is normally generated by gas turbines installed on board. Preliminary feasibility studies indicate that interconnecting these oil installations with wind farms can reduce the fuel consumption with significant environmental and financial benefits.
The paper presents a sensitivity analysis of the voltage and frequency variations for typical transients on an oil platform interconnected to a wind farm. The system dynamics are calculated by running multiple simulations batches on a model developed in PSCAD. Results obtained can be a valuable aid for further studies, as they can identify in advance the parameters that are most important, and that should be modeled more accurately.

Introduction

Offshore oil platforms are conventionally operated as islanded electrical systems since electrical power is locally generated by gas turbines. These turbines have a relatively low efficiency due to strict volume constraints and operation requirements. Considering that the power demand on an offshore installation ranges from tens up to hundreds of MW, this translates into fuel consumption with a significant environmental impact in terms of CO_2 emissions. As an example, platforms on the continental shelf are estimated to contribute as a quarter of the entire Norwegian CO_2 emissions [1]. Furthermore, apart from environmental considerations, taxation on emissions already active in some countries stimulates even more the interest in reducing emissions. A recent trend is electrification of oil platforms with cable connections from shore. However, the connection to the shore can be quite complex especially for distances over few tens of km where AC transmission is impractical and an HVDC technology is required.

Offshore wind farms are an emerging technology still limited by higher costs but credited with a huge potential. Compared to land-based wind farms, the offshore wind installations benefit of more steady wind conditions, negligible visual and acoustic impact, and a large availability of potential sites. In this context, the scenario of offshore wind energy conversion systems (WECS) interconnected to supply local offshore oil platforms can be appealing to lower operating costs. One of the assumptions for the European offshore grid initiative is to connect offshore consumers like oil platforms to the offshore wind generation facilities via an offshore super grid. Even if this configuration has not been implemented yet, preliminary studies indicate its technical and economical feasibility. A study performed by SINTEF and Statoil [2] investigates the amount of CO_2-reductions, and also evaluates the voltage and frequency variations during large disturbances. A few operational scenarios of a wind farm interconnected with an oil platform are simulated in [3] with a main focus on transient stability. Moreover, detailed models and simulation results are described for an islanded power system including a gas/diesel generator connected with induction machine wind turbines [4-9].

The combined system of a wind farm with an oil platform operating in islanded mode is very sensitive to transients and disturbances as load steps, faults, and abrupt variations in the wind speed. Voltage and frequency fluctuations during these transients should be assessed thoroughly and checked against the imposed limits. The common approach in literature is based on numerical simulations on simplified models of the system. However, the simulation results are affected by a large number of parameters whose accurate values can be difficult and time-consuming to collect in advance. The paper presents a sensitivity analysis of the voltage and frequency variations for a set of transients that are likely to occur on an oil platform combined with a WECS. The system dynamics are calculated by running multiple simulations batches on a model developed in PSCAD.

The paper analyzes a typical configuration of an oil platform and of a wind park based on PMSG turbines. The control implementations and the dynamic models of the components used in the simulations are described in the first part of the paper. Then a sensitivity analysis is conducted based on this simulation model by assuming possible variations ranges in the most significant parameters that can affect the transients. Results are summarized and commented in the final part of the paper.

Results obtained can be a valuable aid for further studies serving as a guideline to identify in advance the parameters influence on the system dynamic. Thus, parameters having major influence can be more accurately modeled while saving efforts on the parameters with a minor impact. In addition, the results can provide directions on how to modify/design the system to meet its requirements.

System Description

A schematic view of a notional configuration including a wind park and an oil platform is shown in Fig. 1. The wind farm is modeled as a single unit, including one aggregated Permanent Magnet Synchronous Generator (PMSG) with two Voltage Source Converters (VSC) in back-to-back. The speed of the turbine rotor is controlled in order to achieve maximum power production till nominal wind speed. The blades are actively pitched at higher wind speeds to limit the power.
The oil platform consists of a gas turbine with an associated synchronous generator (SG). The SG is equipped with a governor system in order to control the frequency, and the voltage is controlled by means of an Automatic Voltage Regulator (AVR) connected to the excitation system.
The transmission system between the wind farm and the platform is modeled with ideal transformers and a cable PI-equivalent. The cable is assumed to have a length of 40 km, with PI-equivalent data taken from [10]. Detailed descriptions of the models and control systems are outlined in the following pages.

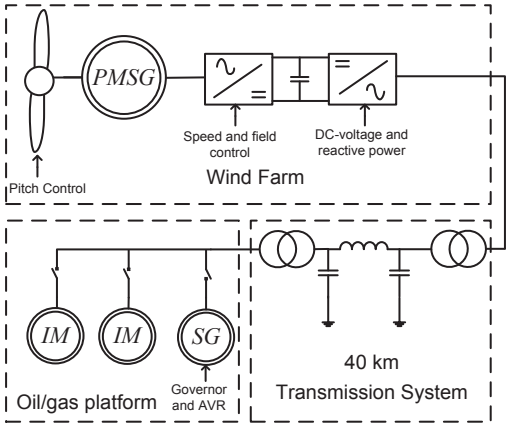

Fig. 1: Overview of Wind Farm and Oil Platform

Turbine Aerodynamics

The aerodynamical model of the wind turbine expresses the relation between mechanical power P_{mech} and wind speed v [11]:

$$P_{mech} = \frac{1}{2} C_p(\lambda, \beta) \rho A v^3 \tag{1}$$

where $A = \pi R^2$ is the rotor area, ρ is the density of air, $\lambda = \frac{\omega R}{v}$ is the Tip Speed Ratio (TSR) and β is the pitch angle [11]. The factor C_p is the ratio between the mechanical power converted and the power available in the wind flow and characterizes the efficiency of the turbine. C_p can be approximated by means of the following empirical equations [12]:

$$C_p = 0.5 \cdot (\frac{116}{\lambda_i} - 0.4\beta - 5) \cdot e^{-\frac{21}{\lambda_i}} \tag{2}$$

$$\frac{1}{\lambda_i} = \frac{1}{\lambda + 0.08\beta} - \frac{0.035}{\beta^3 + 1} \tag{3}$$

Pitch control is implemented in order to limit the mechanical torque at high wind speeds. Common regulator structures are summarized in [13]. Among these, the controller in Fig. 2 is selected for its satisfactory performances. The effectiveness of this control is affected by the mechanical constraints on the twist speed of the blades. This is modeled with a rate limiter of 3 deg/sec.

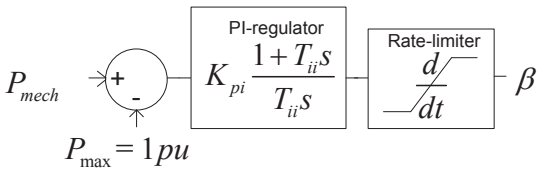

Fig. 2. Block diagram of the pitch controller

Permanent Magnet Synchronous Generator

The wind turbine is equipped with a direct driven PMSG modeled in a synchronous rotating *dq*-reference frame [14, 15]. The d-axis is aligned with the rotor flux, yielding the following dynamic equations[16, 17]:

$$v_{sd} = -R_s i_{sd} - \omega_s \psi_{sq} - \frac{d\psi_{sd}}{dt}$$
$$v_{sq} = -R_s i_{sq} + \omega_s \psi_{sd} - \frac{d\psi_{sq}}{dt} \quad (4)$$
$$\psi_{sd} = (L_{sd} + L_m) i_{sd} + \Psi_f$$
$$\psi_{sq} = (L_{sq} + L_m) i_{sq} \quad (5)$$

where v_{sd} and v_{sq} are the stator voltages in the d- and q-axis, R_s is the stator resistance, i_{sd} and i_{sq} are the stator currents flowing out of the generator and ω_s is the electrical speed of the machine. ψ_{sd} and ψ_{sq} are the flux linkages in the stator, L_{sd} and L_{sq} are the stator leakage inductances and L_m is the mutual inductance between rotor and stator. Ψ_f is the constant flux in the stator produced by the permanent magnets. The torque can then be expressed as [16]:

$$T_e = p \cdot i_{qs}[i_{ds}(L_{sd} - L_{sq}) + \Psi_f] \approx p \cdot i_{sq} \Psi_f$$
$$T_e - T_m = J \frac{d\omega_m}{dt} \quad (6)$$

where p is the number of pole pairs, T_e is the electrical torque, and T_m is the mechanical torque. J is the combined inertia of the turbine and generator, while ω_m is the mechanical speed of the machine.

Generator Side Converter Control

The WECS is controlled by two VSCs operating with sinusoidal PWM. The control structure of the Generator Side Converter (GSC) is shown in Fig. 3. The stator currents in the d- and q-axes are controlled with a fast inner loop and the cross-coupling terms from (4) are accounted for by feed-forward compensation. Two converter models are developed: a detailed model including switches and an average model that emulates infinite switching frequency. The average model was preferred for the final simulations, as its loss of precision is minor compared with the savings in computational time.

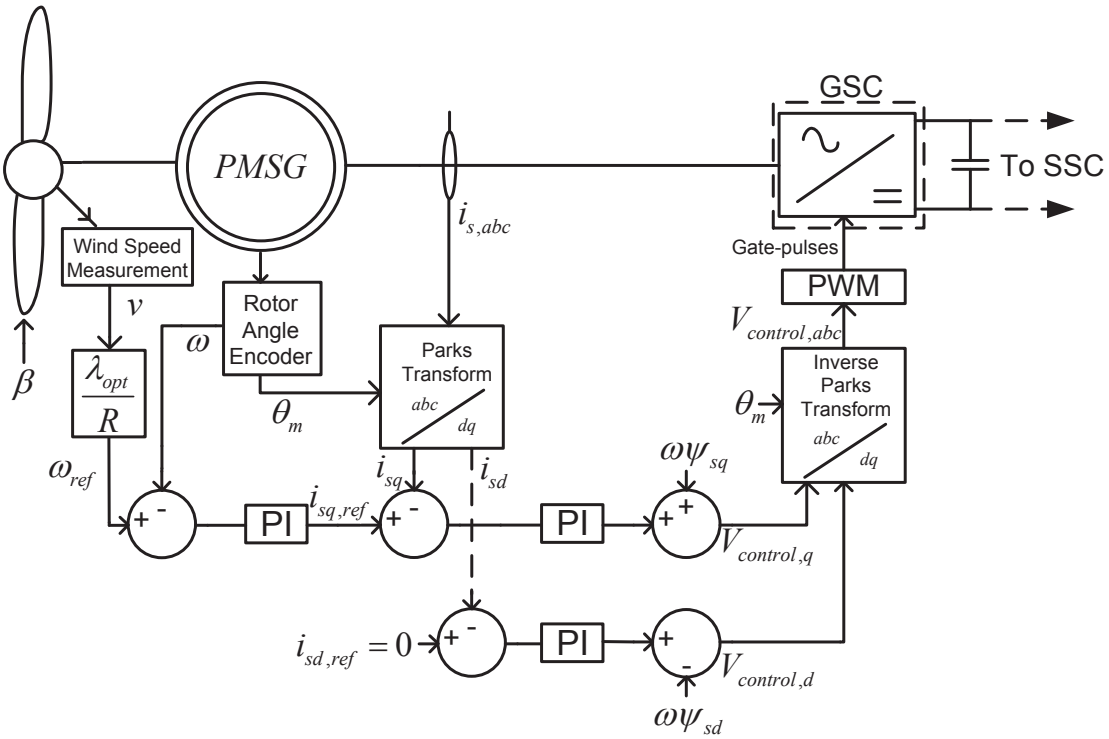

Fig. 3. Generator Side Converter (GSC) with its control structure

The control objectives are to control the flux in the machine and its rotational speed according with a Maximum Power Point Tracking (MPPT) algorithm [18]. The optimal speed reference is $\omega_{ref} = \lambda_{opt} \frac{v}{R}$ where λ_{opt} is the TSR that yields the largest C_p. Speed control is achieved by controlling i_{sq} and hence the torque, as seen from (6). In order to minimize the resistive losses, i_{sd} is controlled to zero, as this minimizes the total current for a fixed T_e. Another viable option could have been to set i_{sd} to reduce core losses through field weakening [18]. The control parameters were determined based on simulations and on the tuning techniques described in [19].

System Side Converter Control

The System Side Converter (SSC) has a control structure similar to the GSC as shown in Fig. 4. The transformation angle is phase-locked to phase A of the voltage V_p such that $V_{pq} = 0$. This is achieved through a Phase Lock Loop (PLL) whose model and equations are derived from [20]. i_d is set to control the DC-voltage, while i_q is controlled to zero in order to exchange no reactive power with the grid. $V_{dc,comp} = \frac{2V_{dc}I_{dc}}{3V_{pd}}$ is a feed-forward term caused by the DC-link current [20].

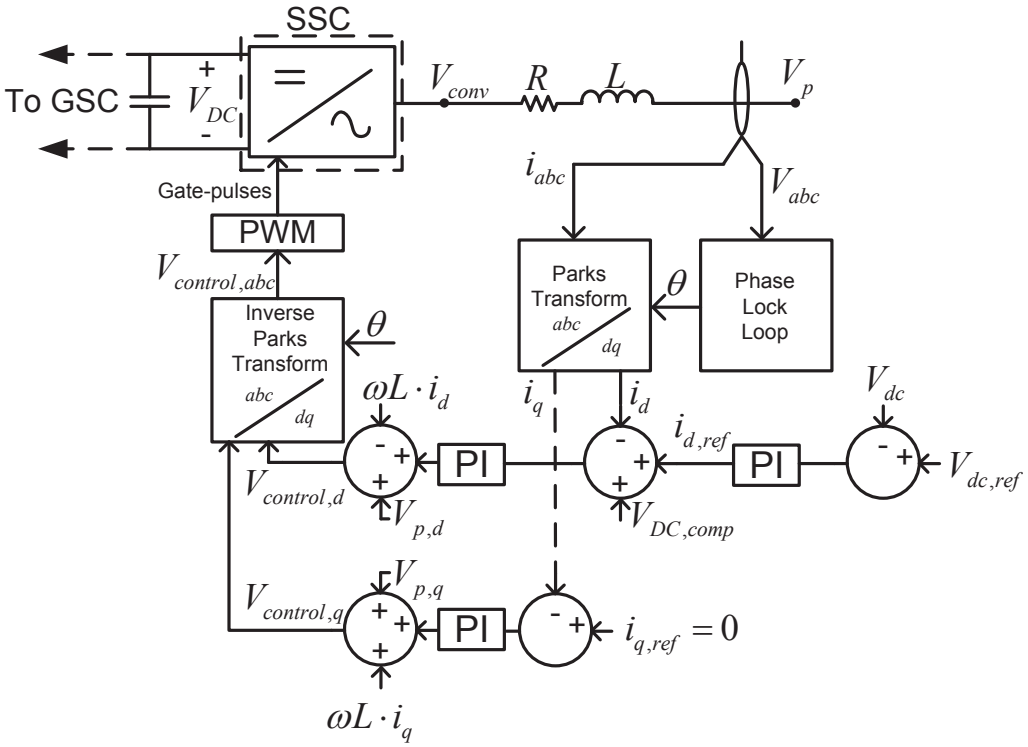

Fig. 4: System Side Converter (SSC) with its control structure

Oil/Gas Platform

The oil/gas platform is represented with a synchronous generator with a gas turbine and two squirrel cage induction motors as load. This aggregated model is a simplified representation of one or more platforms. The motors are directly connected, hence running at fixed speed. The generator parameters were selected according to the typical values reported in [21]. The typical-mode values in PSCAD are used to determine the induction motor parameters.

The gas turbine model is also important since it should reflect the behavior of an actual turbine. Several gas turbine models are available in literature and the model described in [21, 22] was adopted for the simulations. Typical numerical values for the parameters can be found in the same references.

The torque set point for the turbine T_{ref} is determined by means of a governor. The deviation between the reference rotational speed ω_{ref} and the actual speed ω is proportional to T_{ref}. See Fig. 5 for a block diagram of the model.

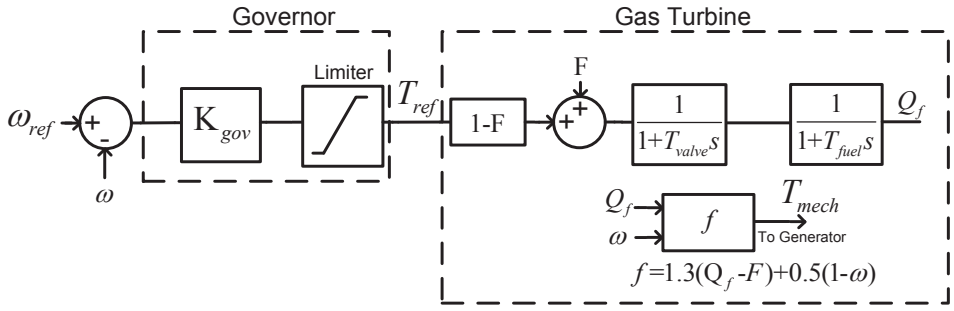

Fig. 5. Gas Turbine and Governor Model

Sensitivity Analysis

The dynamic response of the system during transients is affected by a set of main parameters dependent by the specific components assumed in the simulation. In preliminary studies these parameters are assigned equal to values in a typical range. The sensitivity analysis conducted aims to provide a quantitative estimation of the functional influence of these main parameters on transients. The parameters examined in this sensitivity analysis and their relative ranges of variation are summarized in Table I. For convenience, they are grouped in two sets, Oil Platform Synchronous Generator with Gas Turbine (OP-SGGT) and Wind Farm-Permanent Magnet Synchronous Generator (WF-PMSG). The ranges of variation are based on [23] but they have been slightly exaggerated in order to amplify their effect and provide a more clear understanding. Each of the parameters is changed individually for a predefined transient scenario and its influence on the system voltage and frequency is quantified and discussed.

Table I: Parameters and Ranges in the Sensitivity Analysis

Set	Parameter	Unit	Lowest		Typical		Highest
OP-SGGT	X_d	p.u.	1.2	1.4	1.7	1.9	2**
OP-SGGT	X_q	p.u.	1.2	1.4	1.64	1.9	2**
OP-SGGT	X'_d	p.u.	0.19	0.21	0.245	0.3	0.4*
OP-SGGT	X_d''	p.u.	0.12	0.15	0.185	0.21	0.24
OP-SGGT	X_q''	p.u.	0.05	0.1	0.185	0.3	0.5
OP-SGGT	T'_{d0}	S	1.5	3	5.9	9	15*
OP-SGGT	T''_{d0}	S	0.01	0.02	0.033	0.06	0.12
OP-SGGT	T''_{q0}	S	0.02	0.04	0.076	0.15	0.4
OP-SGGT	R_a	p.u.	0.0005	0.001	0.0033	0.1	0.2
OP-SGGT	X_p	p.u.	0.04	0.07	0.11	0.13	0.18
OP-SGGT	J	S	1*	2	4	7	10
OP-SGGT	K_{gov}	p.u.	10	15	25	40	60
OP-SGGT	T_{fuel}	S	0.1	0.2	0.4	1	3
WF-PMSG	X_d	p.u.	0.31	0.35	0.4	0.6	1
WF-PMSG	X_q	p.u.	0.3	0.4	0.51	0.8	1
WF-PMSG	J	S	2	3	5	8	12
WF-PMSG	K_ω	S	0.5	1.5	3	5	10
WF-PMSG	T_ω	S	0.3	0.6	1	2	4

*The value is excluded from the analysis because it gives too large deviations compared to the other values
** This is the lowest value that did not impose a voltage collapse

Three transient simulation cases are defined, see Table II. They are likely to reflect the most relevant disturbances that can occur in the system. The motor start and fault case are applied to the oil platform, while the variable wind speed is applied to the wind farm parameters. The motor start and fault case is not applied to the wind farm parameters because the control objectives in the wind farm does not provide voltage or frequency support. The wind farm delivers the same active and reactive power regardless of frequency and voltage.

Table II: Simulation cases

Case	Applied to
1. Start-up of a 5 MW directly connected motor	OP-SGGT
2. 30ms 3ph fault with clearing	OP-SGGT
3. Wind Speed Fluctuations	WF-PMSG

Fig. 6 shows how the frequency deviation Δf_{sys} and voltage deviation ΔV_{sys} are calculated. Here, the parameter OPSG- X_d is varied according to the range in Table I, and the motor-start is applied to each simulation. The largest deviation is identified and measured in a plot. This is done for each combination of parameter and simulation case, and the results are summarized in Table III.

.

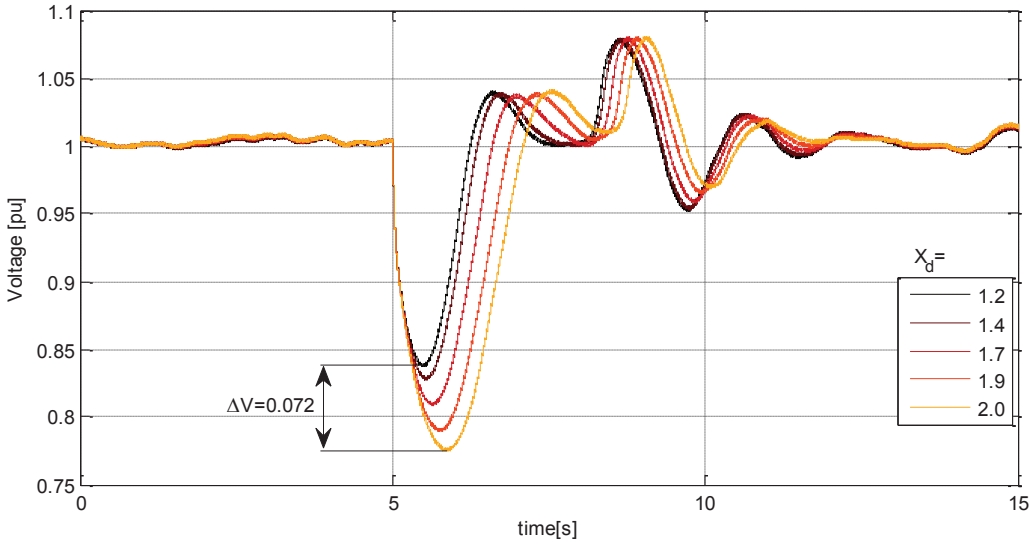

Fig. 6. OPSG- X_d under case 1) Motor Start

Results and Discussion

The sensitivity analysis indicates that the parameters examined do not have the same relative influence on the system but that some of these parameters have a major impact while other a negligible relevance.

The sub-transient parameters $X_d'', X_q'', T_{d0}'', T_{q0}''$ in OP-SGGT have no impact on the motor start case, while they have influence in the fault case. This can be justified by noticing that the fault transient is characterized by fast dynamics where the sub-transient phenomena can have a major influence. On the opposite the dynamics in the motor start up case are not fast enough to have any appreciable effect for the change of sub-transients parameters. To strengthen this statement, the stationary and transient parameters X_d, X_q, X_d', T_{d0}' show sensitive behavior to V_{sys} also in the motor start case. These parameters influence transients with slower dynamics. The last two parameters in the OP-SGGT, armature resistance R_a and Potier reactance X_p, give low Δf_{sys} and ΔV_{sys}. This indicates that accuracy in their modeling is not important.

Table III: Results

		1. Motor Start		2. Fault		3. Fluctuations	
Parameter set	Parameter	Δf_{sys}	ΔV_{sys}	Δf_{sys}	ΔV_{sys}	Δf_{sys}	ΔV_{sys}
		% pu	% pu	% pu	% pu	% pu	% pu
OP-SGGT	X_d	0.12	7.2	-	3.6		
OP-SGGT	X_q	0.12	6.5	-	1.45		
OP-SGGT	X'_d	0.17	10.9	0.13	1.8		
OP-SGGT	X_d''	-	-	0.34	2.5		
OP-SGGT	X_q''	-	-	0.24	1.5		
OP-SGGT	T'_{d0}	-	3.5	0.07	10.9		
OP-SGGT	T''_{d0}	-	-	0.05	1		
OP-SGGT	T''_{q0}	-	1.2	0.1	1.7		
OP-SGGT	R_a	-	-	0.184	0.6		
OP-SGGT	X_p	-	-	-	-		
OP-SGGT	J	1.5	0.67	1.6	1.5		
OP-SGGT	K_{gov}	5.5	4.34	3.1	0.5		
OP-SGGT	T_{fuel}	1.17	-	0.5	1		
WF-PMSG	X_d					-	-
WF-PMSG	X_q					-	-
WF-PMSG	J					0.7	1.0
WF-PMSG	K_ω					2	3.4
WF-PMSG	T_ω					1.5	-

"-" means that the results are below the following thresholds: Frequency: 0.05%, Voltage: 0.5%

None of the generator parameters in OP-SGGT has a significant influence on f_{sys}, indicating that they have low impact on the active power transfer. However, three other parameters are closely linked with the frequency dynamics. The inertia constant *J* in OP-SGGT is proportional to the energy required to accelerate the generator and does hereby decide the amount of active power required to increase the frequency to a given level. Secondly, the gas turbine fuel system time constant T_{fuel} can be interpreted as the major time delay for a power increase in the turbine to be realized. During a disturbance or load change, active power will temporarily be drawn from the energy stored in the rotational mass of the system. This can be seen in Fig. 7a , where T_{fuel} is changed in the motor start case, with variable wind speed applied. A high value of T_{fuel} leads to frequency oscillations because the response time of the gas turbine is increased, and more rotational energy is drawn before the gas turbine reacts. Finally, the droop constant K_{gov} has great impact on the frequency dynamics since it gives the relation between the steady-state frequency and the power output of the OP-SGGT. Fig. 7b shows the frequency variations under the same transient as Fig. 7a. The highest value of K_{gov} yields a high steady-state frequency, in addition to oscillations with low amplitude. A high value seems beneficial from many viewpoints but the parameter should be adjusted to the respective grid code. This will reduce the strain on the gas turbine, since the system is allowed an increased utilization of its rotational energy.

The reactances X_d and X_q in the WF-PMSG do not have any influence on f_{sys} and V_{sys} because the converter creates an electrical decoupling between the WF-PMSG and the rest of the system. However, the WF-PMSG inertia *J* affects the system even though it is on the generator side of the

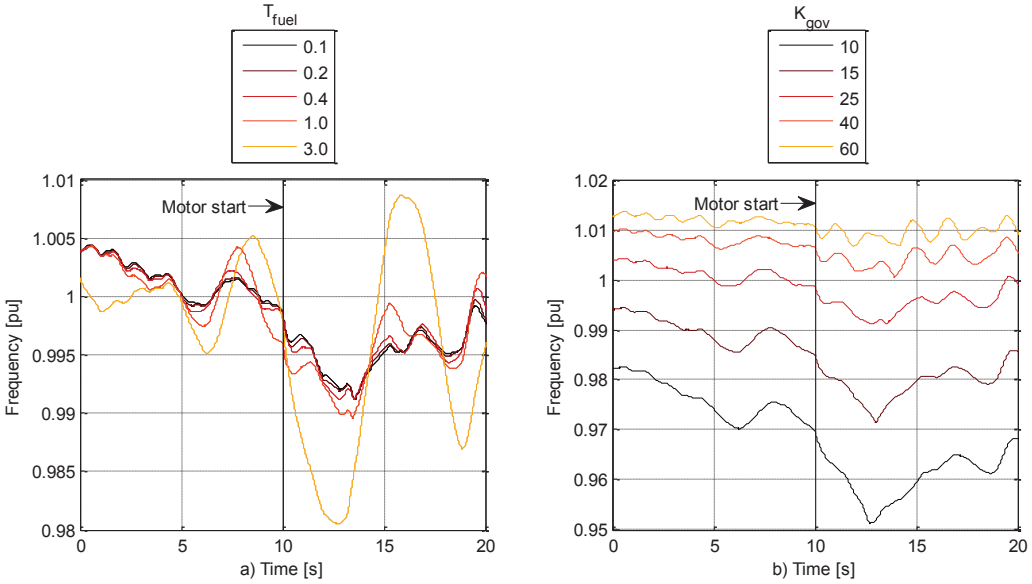

Fig. 7: f_{sys} during the motor start case, with variable wind speed. a)T_{fuel} and b)K_{gov}

converter. Since it measures the amount of energy required to accelerate the wind turbine, a higher inertia means that the turbine requires more energy in order to perform a desired increase of the rotational speed. The additional energy is drawn from the grid and causes variability in frequency and voltage. The inertia is closely linked with the wind turbine speed regulator parameters, K_{ω} and T_{ω}. The regulator parameters decide how fast the wind turbine is allowed to change its rotational speed in order to extract maximum power from the wind, and this ability should to some extent be limited in order to reduce the fluctuations in f_{sys} and V_{sys}.

Conclusions

The paper presents a sensitivity study carried out on an islanded system including an offshore wind farm and an oil platform. A PSCAD simulation model is built based on the system dynamic equations. The wind farm control system is designed such that maximum power is extracted from the wind. Main system parameters are changed individually in order to gain information on their relative importance with respect to the system voltage and frequency during transients. The study is conducted in order to facilitate the modeling process of studies on similar configurations. The knowledge of which parameters have larger influence on the system dynamics can be valuable to provide directions when collecting preliminary data of the system components.

The electrical decoupling introduced by the converters in the wind turbines removes the influence from the wind turbine generator parameters. On the contrary, the wind turbine inertia and speed control parameters are relevant, as they are linked with active power transfer that is preserved by the converter. In addition to the wind farm, the oil platform gas turbine plays an important role in the frequency dynamics, and it should be weighted with high priority to model it accurately.

The type of transient under consideration is related with the set of parameters that have largest impact on the system dynamics. A comparison between the results from a fault and a motor start revealed that the sub-transient parameters $X_d'', X_q'', T_{d0}'', T_{q0}''$ in the oil platform synchronous generator only introduce variability during the steep transients that the fault consists of.

The paper has indicated feasibility of interconnecting WECS with oil platforms, but further work should be carried out in order to obtain the optimal parameters for the regulator settings in the wind turbines and gas turbine governor.

References

[1] J. O. Lamell, T. Trumbo, and T. F. Nestli, "Offshore platform powered with new electrical motor drive system," 2005, pp. 259-266.

[2] W. He, G. Jacobsen, T. Anderson, F. Olsen, T. D. Hanson, M. Korpås, T. Toftevaag, J. Eek, K. Uhlen, and E. Johansson, "The Potential of Integrating Wind Power with Offshore Oil and Gas Platforms," *Wind Engineering,* vol. 34, pp. 125-138, 2010.

[3] D. Hu, X. Zhao, X. Cai, and J. Wang, "Impact of wind power on stability of offshore platform power systems," pp. 1688-1692.

[4] G. Stavrakakis and G. Kariniotakis, "A general simulation algorithm for the accurate assessment of isolated diesel-wind turbines systems interaction. I. A general multimachine power system model," *Energy Conversion, IEEE Transactions on,* vol. 10, pp. 577-583, 1995.

[5] G. Kariniotakis and G. Stavrakakis, "A general simulation algorithm for the accurate assessment of isolated diesel-wind turbines systems interaction. Part II: Implementation of the algorithm and case-studies with induction generators," *Energy Conversion, IEEE Transactions on,* vol. 10, pp. 584-590, 1995.

[6] Q. Jiageng, L. Zongxiang, and M. Yong, "Research on isolated diesel-wind power system equipped with doubly fed induction generator," 2006, pp. 246-250.

[7] C. T. Hsu and C. S. Chen, "Islanding operations for the distribution systems with dispersed generation systems," 2006, pp. 2962-2968 Vol. 3.

[8] A. Haruni, A. Gargoom, M. Haque, and M. Negnevitsky, "Dynamic operation and control of a hybrid wind-diesel stand alone power systems," pp. 162-169.

[9] P. Mahat, Z. Chen, and B. Bak-Jensen, "Gas turbine control for islanding operation of distribution systems," 2009, pp. 1-7.

[10] ABB, "XLPE Sumbarine Cable Systems. Attatchment to XLPE Land Cable Systems - User's Guide."

[11] J. F. Manwell, J. G. McGowan, and A. L. Rogers, *Wind energy explained*: Wiley Online Library, 2002.

[12] B. Liu, X. Peng, and T. Undeland, "Centralized power control strategy of offshore wind farm with permanent magnetic generators," pp. 1075-1079.

[13] J. Zhang, M. Cheng, Z. Chen, and X. Fu, "Pitch angle control for variable speed wind turbines," pp. 2691-2696.

[14] N. Mohan, *Advanced electric drives: analysis, control and modeling using simulink*: Mnpere, 2001.

[15] J. Machowski, J. W. Bialek, J. R. Bumby, and I. NetLibrary, *Power system dynamics: stability and control* vol. 12: Wiley, 2008.

[16] J. Pierik, E. Wiggelinkhuizen, T. Engelen, J. Morren, S. Haan, and J. Bozelie, "Electrical and Control Aspects of Offshore Wind Farms II (Erao II). Volume 2: Offshore wind farm case studies."

[17] V. Akhmatova, A. H. Nielsenb, J. K. Pedersenc, and O. Nymannc, "Variable-speed wind turbines with multi-pole synchronous permanent magnet generators. Part I: Modelling in dynamic simulation tools," *Wind Engineering,* vol. 27, pp. 531-548, 2003.

[18] M. Chinchilla, S. Arnaltes, and J. C. Burgos, "Control of permanent-magnet generators applied to variable-speed wind-energy systems connected to the grid," *Energy Conversion, IEEE Transactions on,* vol. 21, pp. 130-135, 2006.

[19] C. Bajracharya, M. Molinas, J. A. Suul, and T. M. Undeland, "Understanding of tuning techniques of converter controllers for VSC-HVDC," 2008.

[20] T. M. Haileselassie, M. Molinas, and T. Undeland, "Multi-terminal VSC-HVDC system for integration of offshore wind farms and green electrification of platforms in the north sea," vol. 4, p. 12.

[21] J. R. Smith and M. J. Chen, *Three-phase electrical machine systems: computer simulation*: Research Studies Press, 1993.

[22] I. Rowen, "Simplified mathematical representations of heavy-duty gas turbines," *Journal of engineering for power,* vol. 105, pp. 865-869, 1983.

[23] P. Kundur, N. J. Balu, and M. G. Lauby, *Power system stability and control* vol. 19: McGraw-Hill New York, 1994.

Appendix K

Paper presented at NEF technical meeting

This paper was presented at Norwegian Electrotechnical Association in Trondheim 24-25. March 2011. It is written in cooperation with Kristin Høvik and addresses the challenges and potential related with electrification of offshore oil and gas platforms. Focus is put toward the role of power electronics. Note that the paper is written in Norwegian.

The paper describes two offshore power systems, denoted System 1 and System 2. Note that this does not correspond to the systems in the thesis. System 1 in the paper originates from the thesis of Hovik, while system 2 in the paper is the same as System 1 in the thesis.

KRAFTELEKTRONIKKENS ROLLE VED ELEKTRIFISERING AV EKSISTERENDE OFFSHORE INSTALLASJONER, MED KRAFT FRA OFFSHORE VINDPARK OG KRAFT FRA LAND

Av *Atle Rygg Årdal og Kristin Høvik, Prof. Tore M. Undeland (NTNU), Dr. Ing Kamran Sharifabadi (Statoil)*

Sammendrag:

Gassturbindrevne synkrongeneratorer med lav virkningsgrad dekker offshore plattformers kraftbehov, og utgjør en stor del av Norges CO_2-utslipp. Dette kan reduseres ved kraftforsyning fra mindre utslippsintensive kilder.

Denne artikkelen diskuterer motivasjonen bak elektrifisering, og gir en oversikt over eksisterende prosjekter. Ulike teknologier som benyttes blir presentert, med hovedfokus på bruk av kraftelektronikk. Videre beskrives to alternativer til kraftforsyning av offshore oiljeplattform: Tilknyttning av kraft fra land og tilknytting av kraft fra offshore vindkraft. Systemet med kraft fra land til plattformen simuleres for tap av synkrongenerator på plattformen for å belyse problemer som kan oppstå i forbindelse med dette. Systemet med kraft fra offshore vindpark tilknyttet plattformen simuleres for start av en stor direktekoblet induksjonsmotor. Her illustreres det hvordan reaktiv effektkompensasjon fra frekvensomformere i vindturbiner kan redusere spenningsvariasjoner ved hendelser på plattformen. Simuleringer er utført i PSCAD® og MATLAB® Simulink™ SimPowerSystems™.

1 INTRODUKSJON

Global oppvarming er en stor utfordring for verdens befolkning. Konsekvensene kan bli fatale hvis det ikke iverksettes tiltak for å redusere utslippene av CO_2 og andre klimagasser. En stor del av verdens CO_2-utslipp kommer fra elektrisitetsproduksjon, og det er et sterkt fokus på både å forbedre ekstisterende produksjonsmetoder og på nye fornybare energikilder. Landbasert elektrisitetsproduksjon i Norge er i all hovedsak utslippsfri vannkraft, men gjennom overføringskabler til utlandet importeres det store mengder kullkraft i år med lite nedbør.

Olje- og gassinstallasjoner i Nordsjøen er tradisjonelt forsynt av gassturbiner. Driftstekniske krav og restriksjoner på arealbruk gjør at disse har en lav virkningsgrad, og dermed høye CO_2-utslipp per produsert energienhet. Virkningsgraden er rundt 35 % for en vanlig offshore gassturbin [1]. Den norske kontinentalsokkelen er estimert til

å stå for 29 % av Norges totale CO_2-utslipp, hvorav 90 % kommer fra elektrisitetsproduksjon [2]. En reduksjon i utslipp fra petroleumssektoren kan være en viktig bidragsyter til å nå målene som Norge har forpliktet seg til gjennom Kyotoavtalen og Gøteborgprotokollen [3].

For at elektrifisering av oljeplattformer skal føre til reduksjoner i CO_2-utslipp må den alternative energien komme fra en kilde med mindre utslipp enn det eksisterende kraftverket på plattformen. Et moderne kombinert gass- og dampkraftverk på land kan ha virkningsgrad rundt 60 %, og produserer dermed renere elektrisitet enn gassturbinene på plattformer. Flere momenter påvirker imidlertid regnestykket. Det er knyttet overføringstap til elektrifisering, og overskuddsvarme fra gassturbiner på sokkelen blir i dag utnyttet til oppvarming. Konklusjonen i [1] er at plattformer må elektrifiseres fra fornybare energikilder for å oppnå store reduksjoner i CO_2-utslipp.

Blant fornybare energikilder blir ofte offshore vindkraft trukket frem som et lovende alternativ. Potensialet er stort, men det kreves mye arbeid for å redusere de høye kostnadene som er assosiert med offshore vindkraft i dag. Få vindparker er blitt bygget, men mange prosjekter er i planleggingsfasen. 4,5 GW er meldt til NVE i norske havområder [4]. Det er gjort forskning på å koble en offshore vindpark til oljeinstallasjoner. [5] presenterer simuleringer og beregninger på et slikt system uten tilkobling til land.

CO_2-avgift på gassen som blir brukt til å lage elektrisitet er den viktigste økonomiske drivkraften til offshore elektrifisering. I tillegg representerer gassen en tapt kostnad siden den kan selges til markedet i de fleste tilfeller. På den andre siden må det kjøpes elektrisitet i en situasjon med elektrifisering fra land.

Denne artikkelen har som mål å studere elektrifisering av offshore plattformer for å på lang sikt kunne redusere bruken av gassturbiner til elektrisitetsproduksjon på oljeplattformer. Hovedfokus er på rollen til kraftelektronikk ved elektrifisering av eksisterende oljeplattformer. I avnsitt 2.1 gis det en beskrivelse av teknologien som benyttes i HVDC- og HVAC-overføring. Hvordan kraftelektronikk kan utnyttes i offshore vindturbiner diskuteres i avsnitt 0. Avsnitt 3 gir en beskrivelse av de to systemene som undersøkes, med referanser til to masterprosjekter ved NTNU. I avsnitt 4 presenteres simuleringer av systemene, for å belyse utfordringer og muligheter ved elektrifisering. Avsnitt 5 oppsummerer og konkluderer resultatene fra simuleringene, og den generelle diskusjonen i artikkelen.

2 KRAFTELEKTRONIKK I OFFSHORE SYSTEMER

Bruk av kraftelektronikk ved elektrifisering av plattformer øker kontrollmulighetene fra land og fra vindparken. Dette kapittelet gjennomgår grunnleggende omformerprinsipper, bruk av omformere i elektrifisering av plattformer via HVDC eller HVAC-kabler, og drøfter til slutt kraftelektronikk som benyttes i vindturbiner.

2.1 Kraftelektronikk ved tilknytting av HVDC og HVAC til oljeplattform

Kraftelektronikk har en sentral rolle i elektrifisering av oljeplattformer, og i flere av de dominerende generatorteknologiene i en vindpark. AC/DC-omformere er en nødvendighet i alle HVDC-anlegg, og stadig flere vindturbinprodusenter benytter frekvensomformere i sine generatorer. Det benyttes i dag hovedsakelig to teknologier for frekvensomformere. Den tradisjonelle strømstyrte omformeren, eller "current source converter" (CSC), er det billigste alternativet og den har minst tap. Begrensingene til CSC er at den krever et sterkt AC-nett for å fungere, og den tar mye plass. Dette gjør at den ikke er så attraktiv i offshore applikasjoner. Spenningsmatet omformer, også kalt "voltage source converter" (VSC), har bedre egenskaper. Figur 1 viser en prinsippskisse av VSC. Dagens teknologi muliggjør overføring av maksimalt 1200 MW ved en spenning på ± 320 kV [6].

VSC baserer seg på transistorer av typen IGBT. Med en svitsjefrekvens på 1-2 kHz er det mulig å oppnå rask kontroll og et minimum av lavfrekvente harmoniske komponenter. Videre har VSC den fordelen at den kan styre aktiv og reaktiv effekt uavhengig av hverandre, og den har bedre egenskaper under feil i AC-nettet. Valg av kontrollstrategier er sterkt tilpasset bruksområdet, og generelt er VSC en svært fleksibel komponent i kraftsystemet.

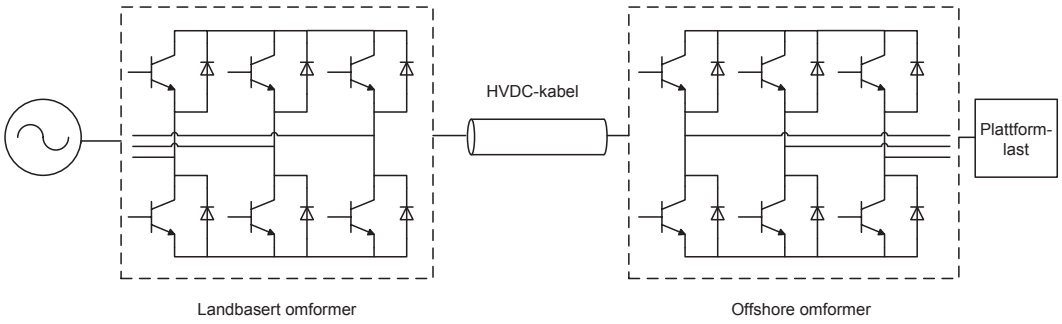

Figur 1: Voltage Source Converter i HVDC-system

Tilknyttning av kraft fra land gjennom HVDC-kabel, hvor omformerene er av CSC-type omtales med et samlebegrep ”HVDC Classic”. Det er to teknologier som benytter VSC, ”HVDC Light™” og ”HVDC Plus™” [7].

Figur 2 viser en prinsippskisse av kostnader ved å elektrifisere en plattform med kraft fra land. HVDC har større oppstartskostnader på grunn av omformere. HVAC blir dyrest for lange avstander på grunn av problemer knyttet til reaktiv kompensering. Krysningspunktet er avhengig av avstand fra land, frekvens på plattformen, plass på plattform og kostnader. For korte avstander, og kraftoverføring mellom 30-50 MVA kan HVAC anses som den mest kostandseffektive løsningen. For de lengste avstandene benyttes HVDC [8]. Krysningspunktet ligger vanligvis rundt 50-100km.

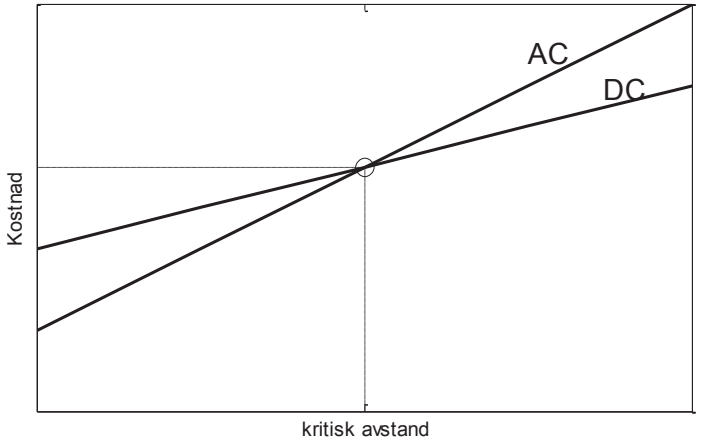

Figur 2: Kostnad for HVAC vs. HVDC

”HVDC Classic”-teknologi ble brukt da den 240 km lange HVDC-kabelen mellom Kristiansand i Norge til Tjele i Danmark ble lagt i 1977 [9]. Denne teknologien ble også benyttet da den 580 km lange HVDC-kabelen ble lagt mellom Norge og Nederland, i NorNed-prosjektet [10].

HVDC Light™ har blitt brukt til forsyning av flere eksisterende plattforminstallasjoner, blant annet til elektrifisering av kompressorer på Troll A-plattformen i 2005 [11]. Da Valhallfeltet ble elektrifisert ble det bygget en ny plattform for omformeren, som gjorde elektrifisering gjennom HVDC Light™ mulig [12].

HVAC har nylig blitt brukt til elektrifisering av den nye offshore installasjonen Gjøa [13], og er planlagt for Goliatfeltet [13].

2.2 Kraftelektronikk i Offshore Vindparker

Direkte tilkoblede induksjonsgeneratorer er enkel og etablert teknologi i vindturbiner, men de har sine begrensinger i offshore vindkraft. For det første er det ønskelig å kunne variere rotorens omdreiningshastighet med vindfarten. Dette gir høyere effekt ved moderat vind, og beskytter det mekaniske systemet under feil. Videre er det ønskelig med en teknologi som har mer styrbarhet mot kraftnettet. Girboks i vindturbiner trenger mye vedlikehold, og må skiftes ut flere ganger i løpet av levetiden. En generator med et tilstrekkelig antall poler gjør et mekanisk girsystem overflødig.

Permanent magnet synkron generator (PMSG) med en frekvensomformer mellom turbinrotor og nett løser problemene nevnt over. Omformeren gir mulighet til å variere generatorfrekvensen og dermed omdreiningshastigheten til rotoren uavhengig av nettfrekvensen. En omformer av typen VSC gir en ekstra frihetsgrad til en rask kontroll av reaktiv effekt til nettet. Det er mulig å benytte frekvensomformere på både induksjonsgeneratorer og vanlige synkrongeneratorer, men PMSG er valgt for å fjerne girboksen fra systemet.

3 SYSTEMBESKRIVELSE

I denne artikkelen studeres to måter å elektrifisere en plattform på. I system 1 forsynes plattformen med kraft fra land og system 2 er et isolert system med plattform tilknyttet en offshore vindpark. Se Figur 3 og 4 for systemskisser. Systemene har utspring i to masteroppgaver ved NTNU.

Synkrongeneratorer med gassturbiner dekker vanligvis oljeplattformers kraftbehov alene. Eksiterings- og governorsystem regulerer henholdsvis spenningen på generatorterminalene og frekvensen i systemet [14]. Ved tilknytting av ekstern kraft er det ønskelig at synkrongeneratorens kraftproduksjon er så liten som mulig, på denne måten minimeres plattformens CO_2-utslipp.

Frekvensen på plattformsystemet som studeres er 60 Hz, noe som er ganske vanlig i Nordsjøen siden mange av plattformene har hatt amerikanske operatorer.

Lasten på plattformen som er studert består hovedsakelig av en stor induksjonsmotor som er å betrakte som en akkumulert modell, og en liten passiv last som representerer lys og servicefunksjoner.

Se avsnitt 6 for verdier for spenning og merkeeffekter.

3.1 System 1: Elektrifisering fra land

System 1 er basert på et lignende system studert i [15]. Ulik frekvens på land og på plattform gjør en frekvensomformer nødvendig. VSC plasseres i dette tilfellet på land, og plattformen forsynes med HVAC-kabler, se Figur 3 for systemskisse. Dette gir kontrollmulighetene som VSC-HVDC introduserer, samtidig som den ikke tar opp plass på plattformen.

Simuleringene fokuserer på å vise systemets svakheter før VSC-kontroll er implementert, og simuleringsmodellen består av en stiv spenningskilde på land, tilknyttet plattformen gjennom en HVAC-kabel.

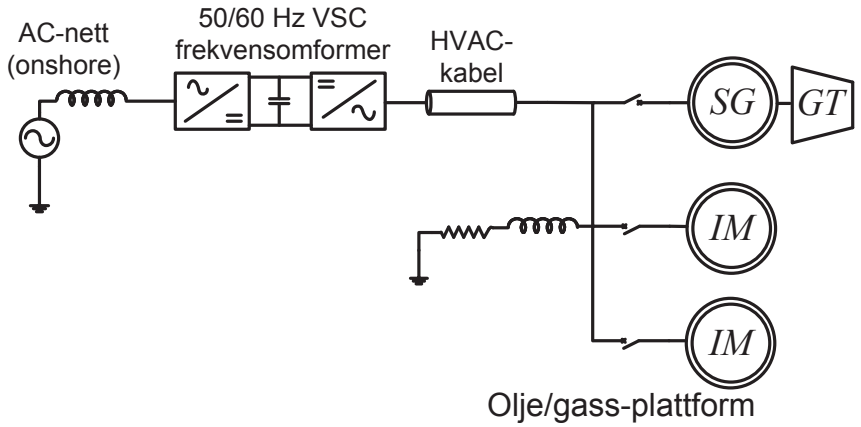

Figur 3: System 1, Elektrifisering av plattform med kraft fra land

3.2 System 2: Elektrifisering fra offshore vindpark

Systemet er basert på [16]. En offshore vindpark er koblet til en oljeplattform uten forbindelse til land som vist i Figur 4. Dette gir flere utfordringer. Energiproduksjonen fra en vindpark er variabel og vanskelig å kontrollere. Gassturbinene med sine synkrongeneratorer må balansere aktiv og reaktiv effekt for å unngå for store avvik i spenning og frekvens.

Simuleringene som presenteres skal illustrere kontrollmulighetene i vindturbinene sine frekvensomformere. De har mulighet til rask kontroll av reaktiv effekt uavhengig av aktiv effektflyt. Kontrollen er implementert med spennings-droop (V-droop), der vindturbinene leverer reaktiv effekt proporsjonalt med avviket mellom terminalspenning og en referansespenning [17].

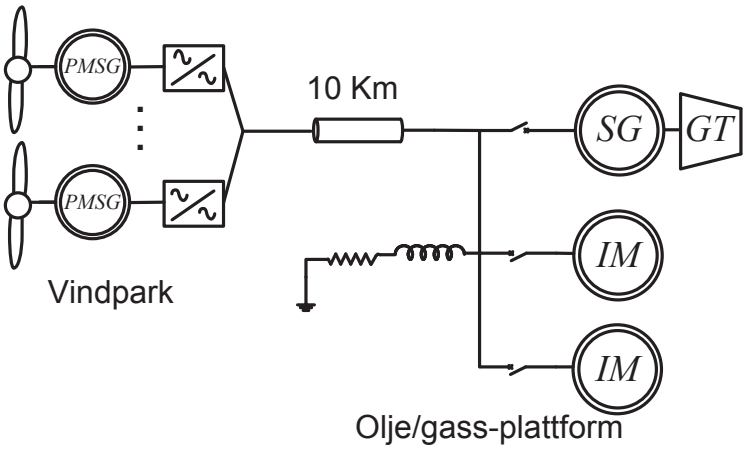

Figur 4: System 2, Elektrifisering fra offshore vindpark

4 SIMULERINGER

System 1 og 2 er modellert i henholdsvis MATLAB® Simulink™ SimPowerSystems™ og PSCAD®. Under følger simuleringsresultater fra hvert system. For system 1 simuleres tap av synkrongenerator. For system 2 simuleres start av en stor direktekoblet induksjonsmotor på plattformen.

4.1 System 1: Frakobling av synkrongenerator

En akkumulert modell av induksjonsmaskiner og en liten passiv last drives på plattformen som initielt er i stasjonær tilstand. Synkrongeneratoren på plattformen frakobles ved t = 4 s. Systemet som simuleres har HVAC-kabler på henholdsvis 10 km, 50 km og 80 km. Figur 5 viser spenningsendringene på plattformen før, under og etter frakobling av synkrongeneratoren.

For alle lengdene på HVAC-kabelen viser resultatene tydelig at spenningsfallet på plattformen etter tap av synkrongenerator er høyere enn hva som aksepteres av IEC-standarden gitt i [18]. Dette betyr at det være nødvendig med en form for kontroll av spenningsnivået på plattformen ved en eventuell frakobling av synkrongeneratoren.

Elektromagnetisk moment for induksjonsmaskiner er tilnærmet proposjonalt med spenning [19]. Et spenningsfall vil dermed medføre at induksjonsmotoren får et lavere elektromagnetisk moment. For kabelen på 10 km stabiliserer induksjonsmotoren seg på et lavere mekanisk og elektromagnetisk moment, som fremdeles er innenfor et akseptabelt arbeidsområde for motoren. På tross av dette er spenningen for lav i følge [18]. Når kabelen er 50 km og 80 km er spenningsfallet så stort at induksjonsmotoren ikke greier å opprettholde et elektromagnetisk moment som kan drive motorlasten. Dette gjør at motoren bremses ned og stopper.

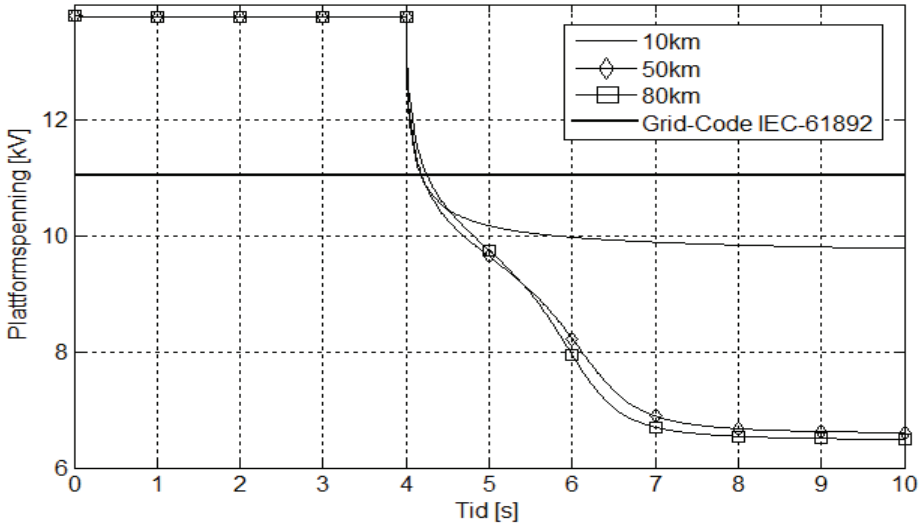

Figur 5: Frakobling av synkrongenerator i system 1

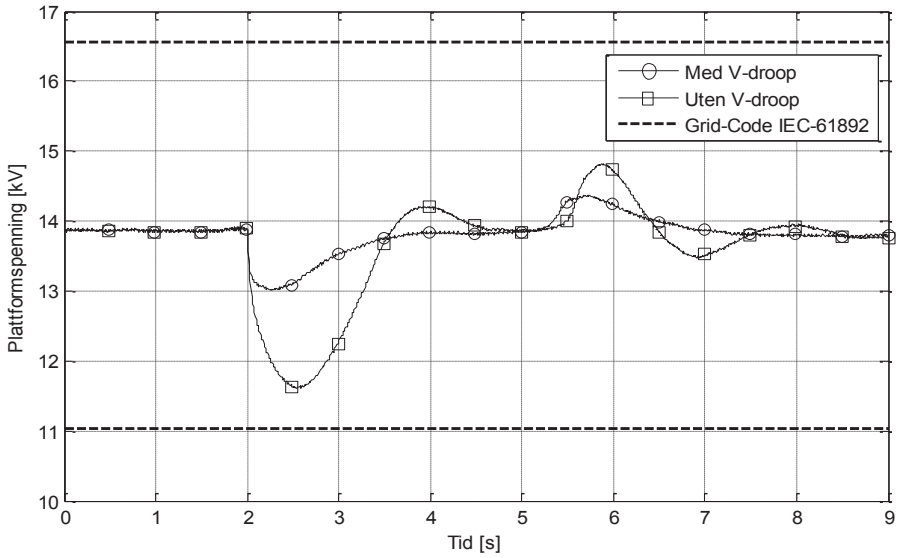

Figur 6: Motorstart med og uten V-droop i system 2

4.2 System 2: Motorstart

En direkte tilkoblet 5 MW induksjonsmotor blir startet i systemet som er vist i Figur 4. Figur 6 viser simuleringer med og uten V-droop i vindturbinene. Resultatene viser en stor reduksjon i spennings-transienten under oppstart når V-droop er implementert. VSC-omformere har kortere tidsforsinkelser enn AVR-eksiteringssytem, slik at de responderer fortere under forstyrrelser. Begge resultatene er innenfor grensene til offshore grid-code for transiente forstyrrelser [18], men start av en noe større motor kan gi problemer for tilfellet uten V-droop.

5 KONKLUSJON

For å redusere CO_2-utslippene fra gassturbiner som benyttes til elektrisitetsproduksjon på oljeplattformer, må andre og renere kilder tilknyttes. I denne artikkelen har forsyning med HVAC-kabler tilkoblet land og kraft fra offshore vindkraft blitt studert.

Artikkelen påpeker hvordan kraftelektronikk muliggjør elektrifisering av oljeplattformer, og kan bidra til et mer driftssikkert elektrisk system.

Simuleringene av system 1 viser at kraftelektronikk er helt nødvendig for kontroll av plattformspenning og aktiv og reaktiv effektforsyning hvis plattformens synkrongenerator faller ut eller kobles fra. Simuleringene viser også hvordan spenningsfallet på plattformen varierer med lengden på HVAC-kablene.

Simuleringene av system 2 viser at spenningsvariasjoner ved direkte start av induksjonsmotor reduseres betraktelig hvis reaktiv effektkompensasjon implementeres i vindturbinens frekvensomformer.

En kombinasjon av tilknyttning av kraft fra land til plattform, og kraft fra offshore vindpark til plattform vil kunne eliminere behovet for synkrongeneratoren på plattformen, og dermed redusere utslipp ved elektritetsproduksjon ytteligere gjennom at kraft fra land er produsert fra fornybare energikilder. Et studie av et slik kombinert system foreslås som fremtidig arbeid, hvor samordning mellom kraftelektronikk er nødvendig for kontroll av spenning og frekvens i systemet.

6 VEDLEGG

Table 6-1, Systemverdier brukt ved simulering

	Verdi	**Enhet**
Plattformspenning	13,8	kV
Synkrongenerator merkeeffekt, system 1	20	MVA
Synkrongenerator merkeeffekt, system 2	50	MVA
Stor induksjonsmotor merkeeffekt	28	MVA
Induksjonsmotor brukt til motorstart	5	MVA
Passiv last	2	MW

Et typisk plattformsystem i nordsjøen er i størrelsesorden 20 MVA og opp mot 100 MVA.

7 TAKK TIL

Forfatterene ønsker å takke PhD-studentene Sverre Skalleberg Gjerde og Raymundo Torres-Olguin, samt Dr.Eng Jan Wiik (ABB) for deres støtte ved utarbeiding av prosjektene og artikkelen.

8 REFERANSER

[1] O. L. (OLF), "Elkraft fra land til norsk sokkel," 2003.

[2] Regjeringen. (2006-2007, 2011-01-31). *Stortingsmelding nummer 34, Om norsk klimapolitikk*.

[3] K.-o. forurensningsdirektoratet. (2010, 02.17). *Gjøteborgprotokollen*. Available: http://www.miljostatus.no/Tema/Luftforurensning/Sur-nedbor/Goteborgprotokollen/

[4] NVE. (2011, 2011-01-31). *Vindkraft*. Available: http://www.nve.no/no/Konsesjoner/Konsesjonssaker/Vindkraft/

[5] G. J. W. He, T. Anderson, F. Olsen, T. Hanson, M. Korpås, T. Toftevaag, J. Eek, K. Uhlen, E. Johansson, "The Potential of Integrating Wind Power with Offshore Oil and Gas Platforms," Sintef Energy Research, T2010.

[6] ABB. (2010, 16.02.2011). *HVDC Light is the most interesting power transmission system developed for several decades*. Available: http://www.abb.com/industries/us/9AAC30300394.aspx

[7] R. Rudervall*, et al.*, "High voltage direct current (HVDC) transmission systems technology review paper," *Energy week,* pp. 7–8, 2000.

[8] N. Hörle*, et al.*, "Electrical supply for offshore installations made possible by use of VSC technology," in *Cigré 2002 Conference*, Paris, France, 2002.

[9] ABB. (2011). *Skagerrak 1-3 HVDC Interconnections* Available: http://www.abb.com/industries/ap/db0003db004333/e9c890cb41ffa3d5c125774a0044be37.aspx

[10] ABB. (2008, 17.02.11). *The NorNed HVDC Connection, Norway – Netherlands*. Available: http://www05.abb.com/global/scot/scot245.nsf/veritydisplay/2402665447f2d054c12571fb00333968/$file/project%20norned%20450%20kv%20dc%20mi%20sub.pdf

[11] ABB. (2010, 22.11.2010). *Power from shore: ABB technologies at Troll A platform* Available: http://www.abb.cl/industries/ap/db0003db004333/8c3aa401373d6f9cc125774a0049a015.aspx

[12] S. Gilje and L. Carlsson, "Valhall Re-development project, power from shore," Energex, 2006.

[13] ABB. (2010, 04.12.2010). Submarine Power Cables, Cables for offshore platforms and wind farms. Available: http://www05.abb.com/global/scot/scot245.nsf/veritydisplay/796660a22284a381c125777c00448c08/$File/Submarine%20power%20cables%20for%20offshore%20wind%20farms%20and%20platforms%202GM5010-gb%20oil%20rev%202010-08.pdf

[14] P. Kundur, *Power System Stability and Control*: McGraw-Hill Professional 1994.

[15] K. M. Høvik, "Study on Shore Converter Operated in Parallel with Platform Synchronous Generator," NTNU, Institute of Electric Power Engineering, Department of Energy Conversion, Trondheim2010.

[16] A. R. Årdal, "Modeling and Simulation of an offshore wind farm connected to an oil platform as an islanded system," NTNU, Institute of Electric Power Engineering, Department of Energy Conversion, Trondheim2010.

[17] F. Katiraei and M. R. Iravani, "Power Management Strategies for a Microgrid With Multiple Distributed Generation Units," *Power Systems, IEEE Transactions on,* vol. 21, pp. 1821-1831, 2006.

[18] IEC, "IEC 61892: Mobile and Fixed Offshore Units," in *Internasjonal grid-code*: IEC, 2010.

[19] J. Stephen, *Chapman, Electric Machinery Fundamentals*: McGraw-Hill, 2005.